

RADIATIVE NEUTRON CAPTURE INTO THE
GIANT RESONANCE REGION OF ^{41}Ca

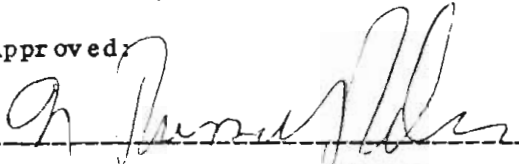
by

Colleen Mary Fitzpatrick

Department of Physics
Duke University

Date: April 15, 1983

Approved:



N. Russell Roberson, Supervisor







A dissertation submitted in partial fulfillment of
the requirements for the degree of Doctor
of Philosophy in the Department of
Physics in the Graduate School
of Duke University

1983

Abstract

RADIATIVE NEUTRON CAPTURE INTO THE
GIANT RESONANCE REGION OF ^{41}Ca

by

Colleen Mary Fitzpatrick

Department of Physics
Duke University

Date: April 15, 1983

Approved:

N. Russell Roberson

N. Russell Roberson, Supervisor

Henry R. W. Walker

Richard L. Walter

Lambert

An abstract of a dissertation submitted in partial
fulfillment of the requirements for the degree
of Doctor of Philosophy in the Department
of Physics in the Graduate School
of Duke University

1983

ABSTRACT

Neutron radiative capture is a useful tool in the investigation of the contribution of non-E1 effects in the capture reaction, since the recoil effective charge of the captured neutron is small for these higher multipolarities. Therefore, the direct contributions of these higher multipolarities to the cross section does not obscure the more interesting resonance effects in the giant resonance region. The $^{40}\text{Ca}(n,\gamma)^{41}\text{Ca}$ reaction is useful in studying these effects in that the ground state of ^{41}Ca has a large spectroscopic factor, and neutron capture in this reaction can only excite the $T = 1/2$ component of the giant resonance region, reducing the complexity of the analysis.

The work reported here is a study of the $^{40}\text{Ca}(n,\gamma)^{41}\text{Ca}$ reaction for excitation energies in the giant resonance region of ^{41}Ca . A detailed comparison will be made between the measured yield curve and angular distributions of cross section and analyzing power and calculations based on the direct-semidirect model. Particular attention will be given to the strength of non-E1 radiation in the reaction.

In general, the data are very well described by calculations based on the direct-semidirect model. The cross section measurements are reproduced quite well by including only E1 terms in the calculations. But the presence of non-zero odd a_i and b_i coefficients extracted from the angular distributions of cross section and analyzing power indicate the presence of non-E1 radiation in the

reaction. The addition of a semidirect E2 term using either a surface-peaked or a volume form factor improves the agreement between the data and the calculated coefficients. Additional analysis was done including a direct M1 term in the calculations, the effect of which was to further improve the agreement with the b_1 coefficients. The agreement with the 90° analyzing power was also improved.

Finally, an analysis was done to determine what amplitudes contributed to the capture process. It was found that if the $g_{7/2}$ "spin-flip" amplitude was neglected, the $g_{9/2}$ amplitude accounts for about 80% of the E1 cross section. When E2 amplitudes were also included, no unique solution could be determined because of the large number of amplitudes involved.

ACKNOWLEDGEMENTS

Without the grace of the Lord Jesus Christ, I would not have been able to complete this project. I am thankful for His constant presence during this time.

I would like to thank my advisor, Dr. N. Russell Roberson, for his stimulating attitude during the course of my work, and Dr. Henry R. Weller for additional support and discussion during this time. In the earlier parts of this work, the support of Dr. S. A. Wender was especially valuable. In addition, I would like to recognize the other members of the capture group, both past and present, for their valuable assistance in the data-taking involved in this project.

The help of Dr. T. B. Clegg with the maintenance of the polarized ion source was indispensable. I gratefully acknowledge the technical assistance of Mrs. Joseph Bailey in the preparation of the figures in this thesis, and the assistance of Mr. S. E. Edwards in computer and electronic maintenance. Mr. R. L. Rummel, and Mr. P. Carter also offered invaluable technical support to this project.

The loving patience of my parents, Mr. and Mrs. E. M. Fitzpatrick was appreciated more than they realize, as well as that of my grandmother, Mrs. Bernard F. Rice.

Finally, I would like to thank the following personal friends for their understanding and friendship during these years: Harold Pfutzner, Linda Franks, Suzan Orchard, Kathlyn Rhymes, Mark and Karen Philbrick, Paula Chauncey, Louise Baker, and Bonita Franks.

Table of Contents

	<u>Page</u>
Abstract	iii
Acknowledgements	v
List of Figures	viii
List of Tables	x
1. Introduction	1
2. Experimental Apparata	5
A. Introduction	5
B. Ion Beams	6
C. Neutron Beams	10
D. Target	16
E. Detectors	16
F. Electronics and Data Acquisition	19
1. Monitor Electronics	19
2. NaI Detector Electronics	25
3. Experimental Results	36
A. Absolute Cross Section Measurements	36
B. Analyzing Power Measurements	54
C. Angular Distribution Measurements	60
1. Cross Section	60
2. Analyzing Power	68
4. Theory	74
A. Classification of Multipole Resonances	74
B. Formalism	76
C. Transition Matrix Elements	78
5. Analysis of Experimental Results	84
A. Absolute Cross Section Calculations	84
B. Calculations of the Legendre and Associated Legendre Coefficients	88
C. Calculations of Analyzing Power	95
D. Summary	97
6. Transition Matrix Amplitude Analysis	98

A. Pure E1 Analysis	98
B. E1-E2 Analysis	103
7. Conclusions	113
Appendix A	116
Bibliography	134

List of Figures

<u>Figure</u>		<u>Page</u>
2-1	The three stage bunching system used in these experiments.	7
2-2	Voltages applied to the double buncher as a function of time.	9
2-3	The general lay-out of the Triangle Universities Nuclear Lab.	11
2-4	$\sigma(0^0)$ vs E_d for the reaction $D(d,n)^3\text{He}$.	12
2-5	$\sigma(\theta)$ vs θ for the reaction $D(d,n)^3\text{He}$ at $E_n = 10.2$ MeV.	13
2-6	Deuterium gas cell.	15
2-7	Detector geometry.	18
2-8	A block diagram of the monitor electronics.	20
2-9	A typical monitor pulse-shape-discrimination (PSD) spectrum.	23
2-10	A typical monitor time-of-flight (TOF) spectrum.	24
2-11	A block diagram of the NaI electronics.	26
2-12	A typical γ -ray spectrum.	27
2-13	The energy levels of ^{41}Ca .	28
2-14	A typical γ -ray spectrum at several stages of processing.	31
2-15	A typical NaI time-of-flight (TOF) spectrum.	32
3-1	Model for the geometry used in the finite geometry corrections to the data.	38
3-2	Finite geometry correction factors as a function of neutron energy.	42
3-3	Efficiency of one of the NaI detectors as a function of gain for $E_\gamma = 15$ MeV.	45

3-4	Efficiency factor $f(E_\gamma)$ as a function of E_γ .	46
3-5	Absolute 90° cross section measurements for the $^{40}\text{Ca}(n, \gamma_0)^{41}\text{Ca}$ reaction.	48
3-6	$\sigma(90^\circ)/A_0$.	52
3-7	Total cross section calculations as a function of neutron energy.	53
3-8	The total cross section for the $^{41}\text{Ca}(\gamma, n_0)^{40}\text{Ca}$ reaction.	55
3-9	The 90° analyzing power measurements as a function of neutron energy.	57
3-10	Angular distributions of cross section.	62
3-11	The a_i coefficients extracted from the angular distributions of cross section.	63
3-12	Angular distributions of analyzing power.	69
4-1	Some possible nuclear vibrational modes with the associated spin and isospin selection rules.	75
5-1	DSD model calculations of $\sigma(90^\circ)$.	87
5-2	DSD model calculations of the a_i and b_i coefficients compared to the data.	92
5-3	DSD model calculations of the a_1 and b_1 coefficients.	94
5-4	DSD model calculations of the 90° analyzing power.	96
6-1	Percent $\sigma_{g_{9/2}}$ of the total E1 cross section.	102
6-2	Contour plot produced from a χ^2 search on the $p_{3/2}$ and $h_{11/2}$ E2 amplitudes at $E_n = 10$ MeV.	110
6-3	Contour plot produced from a χ^2 search on the $f_{7/2}$ and $h_{11/2}$ E2 amplitudes at $E_n = 10$ MeV.	111

List of Tables

<u>Table</u>		<u>Page</u>
3-1	Absolute cross section parameters.	36
3-2	Typical experimental parameters.	39
3-3	Finite geometry correction factors.	43
3-4	Values of $\sigma(90^\circ)$ as a function of neutron energy.	49
3-5	Values of $\sigma(90^\circ)/A_0$ derived from angular distribution data.	51
3-6	90° analyzing power measurements as a function of neutron energy.	58
3-7	Experimental parameters of 90° analyzing power measurements.	59
3-8	Legendre coefficients extracted from fits of angular distributions of cross section to third order.	64
3-9	Legendre coefficients extracted from fits of angular distributions of cross section to fourth order.	65
3-10	Experimental parameters of angular distribution measurements.	66
3-11	Associated Legendre coefficients extracted from fits of angular distributions of $\sigma(\theta)A(\theta)/A_0$ to third order.	71
3-12	Associated Legendre coefficients extracted from fits of angular distributions of $\sigma(\theta)A(\theta)/A_0$ to fourth order.	72
5-1	Becchetti-Greenlees optical model parameters.	85
5-2	Parameters used in calculations of final single-particle state.	86
5-3	Parameters used in the E1 particle-core vibrational coupling term.	89
5-4	Parameters used in the E2 particle-core vibrational coupling term.	91
6-1	Results of pure E1 analysis based on the extracted a_2 and b_2 coefficients.	100
6-2	Results of pure E1 analysis based on direct fit to data.	101
6-3	Solutions of E1-E2 transition matrix analysis for search on $f_{7/2}$ and $h_{11/2}$ amplitudes.	108

6-4 Solutions of E1-E2 transition matrix analysis for search on $p_{3/2}$
and $h_{11/2}$ amplitudes.

109

1. Introduction

In recent years, there has been considerable advancement in understanding the radiative capture of fast nucleons. One formalism which has been successful in describing the capture reaction is the direct-semidirect model. In this picture, the transition amplitude consists of two terms, one of which is called the direct term and the other the semidirect (or collective) term. By the expression "direct" capture is meant a one-step process in which the projectile undergoes a radiative transition directly into a single particle bound state. The expression "semidirect", on the other hand, implies a two-step process in which the incoming nucleon inelastically excites the target nucleus into a collective state while being captured into the same single particle bound state as in the "direct" capture. The radiative decay of this system produces the enhanced transition strength associated with the giant resonances. The semidirect process takes place in a time long compared to the direct process, but short compared with compound nucleus formation and decay.

Originally, the idea of "direct" capture was suggested by Cohen [Coh55] to explain the failure of the compound nucleus model to describe (p, γ) cross sections. Lane and Lynn [Lane59] later made more detailed comparisons between the observed nucleon capture cross sections and the predictions of both the compound nucleus theory and

direct model calculations. They found that the compound nuclear mechanism was insufficient to explain the observed cross sections for $E_{\text{proj}} \geq 10$ MeV, especially in heavy elements. However, they found that the direct capture mechanism not only accounted for the order of magnitude of the cross section in this energy region, but also for its slowly varying dependence on both energy and atomic number.

The theory was further refined by Brown [Brow64] and Clement et al. [Clem65] by the addition of the "semidirect" term to the formalism. It was shown that the inclusion of the semidirect process gave the calculations a general resonance shape, and enhanced the calculated cross sections by about an order of magnitude in the giant resonance region.

Studies of the giant resonance region of a variety of nuclei have been done at TUNL [Well80, Ward81, Wend82] using radiative capture of protons, neutrons, and α particles as probes. Because angular distribution measurements of cross section do not provide enough information to determine the transition matrix elements in a given reaction, studies have also been made involving angular distributions of analyzing power (see [Well82] for a survey of earlier work). The first polarized neutron capture experiment was done at TUNL [Jens79]. Radiative capture reactions are the time-reversal equivalent of photoabsorption reactions, but they select only one possible channel of the photoabsorptive process. The two types of cross sections are related through the principle of detail balance [Hayw70]. In addition, through radiative capture, studies can be made of the

photoabsorption of nuclei in excited states, which is otherwise impossible.

The systematics of the giant dipole resonance (GDR) are now well known [Hann79] and attention has been turned to the study of resonances of higher multiplicities. Neutron capture should be an especially useful tool [Arth75] in such investigations. This can be seen as follows. In the direct-semidirect model, the direct term of the transition matrix element is proportional to the effective charge of the incoming nucleon [Well80],

$$e_L = [A_t^L Z_p + (-1)^L Z_t A_p^L] / [A_p + A_t]^L \quad 1-1$$

where the subscripts t and p refer to the target and projectile, respectively, and L is the multipolarity of the transition. In the case of quadrupole (L=2) radiation,

$$e_2 = [A_t^2 Z_p + Z_t A_p^2] / [A_p + A_t]^2 \quad 1-2$$

The ratio of the quadrupole effective charge of the neutron to that of the proton is thus

$$e_{\text{neut}}/e_{\text{prot}} = Z_t/[A_t^2 + Z_t] \quad 1-3$$

For example, with ^{40}Ca as the target, this ratio is approximately 1/80. This implies, for E2 radiation, that the semidirect or resonance process should be more apparent in the case of neutron capture, because it is not obscured by the direct capture contributions to the matrix elements.

The work reported in this thesis is a study of the $^{40}\text{Ca}(n,\gamma_0)^{41}\text{Ca}$ reaction for excitation energies in the giant resonance region of ^{41}Ca . A detailed comparison will be made of the measured yield curve and the angular distributions of cross section and analyzing power with calculations based on the direct-semidirect model. Special attention will be given to the strength of non-E1 radiation in the reaction, i. e. E2 and M1.

There are several advantages in studying this reaction. An earlier measurement of the 90° yield curve in 1 MeV energy steps [Berg74] clearly showed a giant resonance behavior. Also, an earlier DSD model calculation [Poto73] gave a reasonable fit to this yield curve. Finally, the complexity of the analysis of the results in this case is reduced considerably by the fact that the ground state spectroscopic factor of ^{41}Ca is large [Belo65] and that neutron capture can excite only the $T=1/2$ components of the giant resonances.

From the experimental point of view, it is necessary to have approximately 60 grams of target material, which in this case is easily obtainable in the form of natural calcium ($\simeq 97\%$ ^{40}Ca). Also, the γ -rays from transitions to the ground state and the first excited states are readily separated and detected by the two large NaI spectrometers available at TUNL which have an energy resolution of $\simeq 3\%$ for 20 MeV γ -rays.

2. Experimental Apparata

A. Introduction

During the course of the experiments described in this thesis, there was substantial change in the data-taking apparatus. The earlier data were taken with a Honeywell DDP-224 computer, using only a single NaI detector. This system has been replaced with a VAX 11/780 computer operating under the XSYS data handling system. In addition, a second NaI crystal was installed which especially facilitated the acquisition of data obtained with polarized beams. Since in all major aspects, the experimental procedure remained essentially the same, only the latter system will be described here.

In all cases, the required flux of neutrons on target was supplied by bombarding a deuterium filled gas cell with a beam of deuterons accelerated by a type FN Tandem Van de Graaff. Polarized neutrons were obtained when the deuterons were supplied by the Lamb-Shift polarized ion source. Unpolarized neutrons were produced by deuterons from a direct-extraction negative ion source. The γ -rays were detected by two large NaI detectors. In the following sections, descriptions of the experimental set-up and the data reduction and analysis are presented.

B. Ion Beams

As discussed above, this project required both polarized and unpolarized beams. The unpolarized beams were produced by a direct-extraction negative ion source, which can provide typically 40 to 60 microamps of deuterons. As the beam leaves the source, it first passes through a standard HVEC HV chopper, a pair of plates driven with a sine wave voltage at 2 MHz to sweep the beam across a 3/8 inch aperture. The retrace pulse is eliminated by a second pair of plates, perpendicular to the first pair, which act as an auxiliary chopper. The resulting beam packets then enter a double gap klystron buncher, where they are compressed so that, on target, the beam bursts have a width of about 2 ns. In this process, only about 2 microamps of beam is delivered to the entrance tube of the accelerator.

Polarized beam for this work was supplied by the TUNL Lamb-Shift polarized ion source. This source has been described in detail elsewhere [Cleg74] and will not be discussed here. Production of pulsed polarized beam must be handled differently because much lower beam intensities provided by the source, typically 300 to 400nA of polarized beam. The three stage bunching system used in these experiments appears in Fig. 2-1 [Wend80,Wend81]. As the beam emerges from the duoplasmatron, it experiences a linear ramp voltage of about 70V peak to peak at 4 MHz. Since the beam energy at this point is 1100V, the drift length of approximately 1.5 meters in the source allows the beam to compress into beam packets which are less than 140 nsec long. After the beam has been accelerated by 50 kV, it is

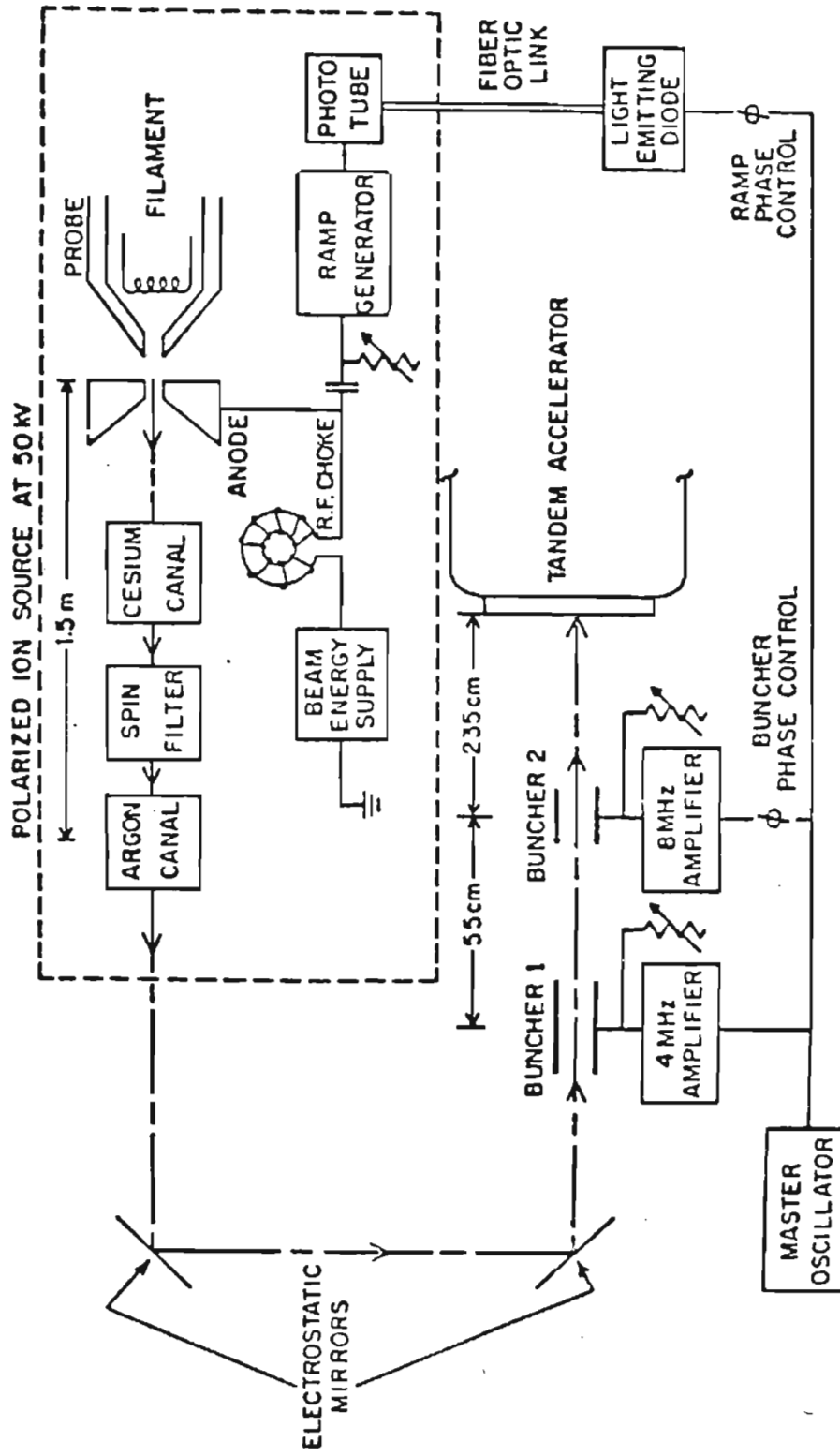


Figure 2-1. The three stage bunching system used in these experiments.

injected into a double-drift bunching system with a time acceptance of ~ 140 ns. Since the packet size is less than the acceptance time, the phasing of the ramp relative to the double drift buncher is not critical. The actual ramp voltage is adjusted to obtain the maximum buncher efficiency and optimum timing.

The first element of the double-drift system is a double-gap buncher which is operated at 4 MHz. Since the linear portion of the sine wave voltage is only about 20% of the total cycle, this would be the maximum efficiency of the first buncher operating alone. However, since a second buncher follows, by phasing the two elements, it is possible to obtain much higher efficiencies. This is illustrated in Fig. 2-2. Those portions of the cycle of the first buncher which most deviate from a linear voltage (causing "overbunching") are corrected for by driving the second buncher out of phase with and at twice the frequency of the first buncher. In practice, 60 to 70% of the cycle is useful because of the drift space of 55 cm between the two elements which allows the beam leaving the first buncher to compress somewhat before entering the second buncher. Typical peak to peak voltages are 4.3 kV for the first buncher and 1.3 kV for the second buncher.

Because this system consists of a ramp and two bunchers, there was normally about 10% of the beam on target that was not in the beam packets. The addition of an auxiliary chopper (not shown in Fig. 2-2) following the second element of the buncher and before the entrance to the tandem was found to eliminate this problem. Typically, 60 to 70% of the dc beam on target is bunched into 2 nsec wide pulses. For both

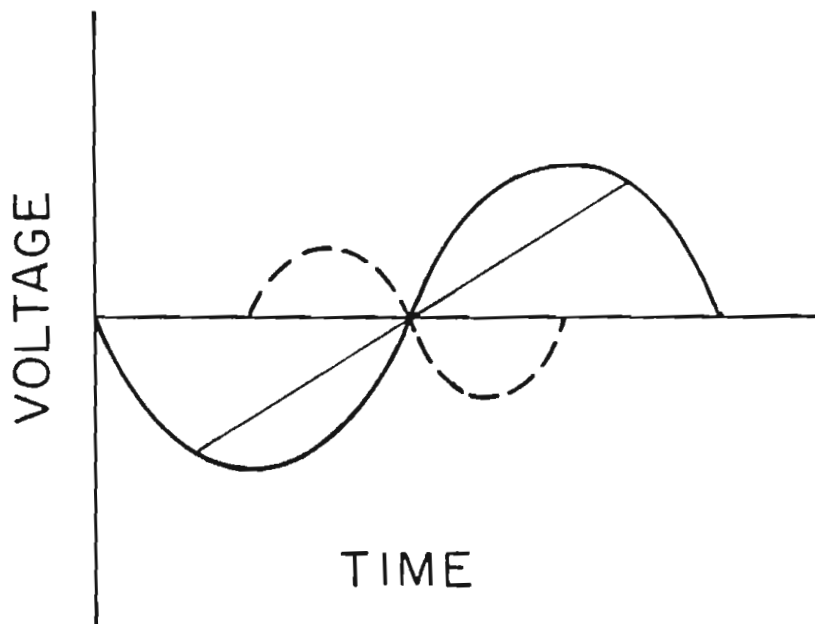


Figure 2-2. Voltages applied to the double buncher as a function of time: voltage on the first element (solid curve), voltage on the second element (dashed curve), and net voltage (straight line).

polarized and unpolarized beams, the bursts are detected near target by a capacitive pick-off unit which generates a timing signal.

The general lay-out of the laboratory can be seen in Fig. 2-3. After the beam has been chopped and bunched, it is injected into the tandem. At the center of the terminal, the beam passes through a carbon foil which strips the electrons off the negative ions. The positive beam exits the accelerator and is steered through two ninety degree magnets, which select beam of only the correct energy. Between these magnets is a pair of slits which provide a feedback correction signal to a circuit which controls the potential on the terminal. Finally, the beam passes through a switching magnet which sends it down the correct beam leg (30° left in target room #4). Typical beam intensities used for this experiment were of the order of 350 nA for unpolarized beams and 100 nA for polarized beams.

C. Neutron Beams

Because neutrons are electrically neutral, it is necessary to use secondary reactions to produce a flux of these particles. In these experiments, the $D(d,n)^3\text{He}$ reaction was used because its cross section is forward peaked with relatively high intensity (Fig. 2-4) [Drosg78]. A large fraction of the neutron flux occurs in a cone of $\theta < 20^\circ$ (see Fig. 2-5). The deuterium gas necessary to produce this reaction was contained in a 1-inch gas cell which was pressurized to up to 90 psia and which was located at the end of the beam leg. The incident deuterons first pass through a tantalum collimator and then

Cyclo-Graaff Laboratory

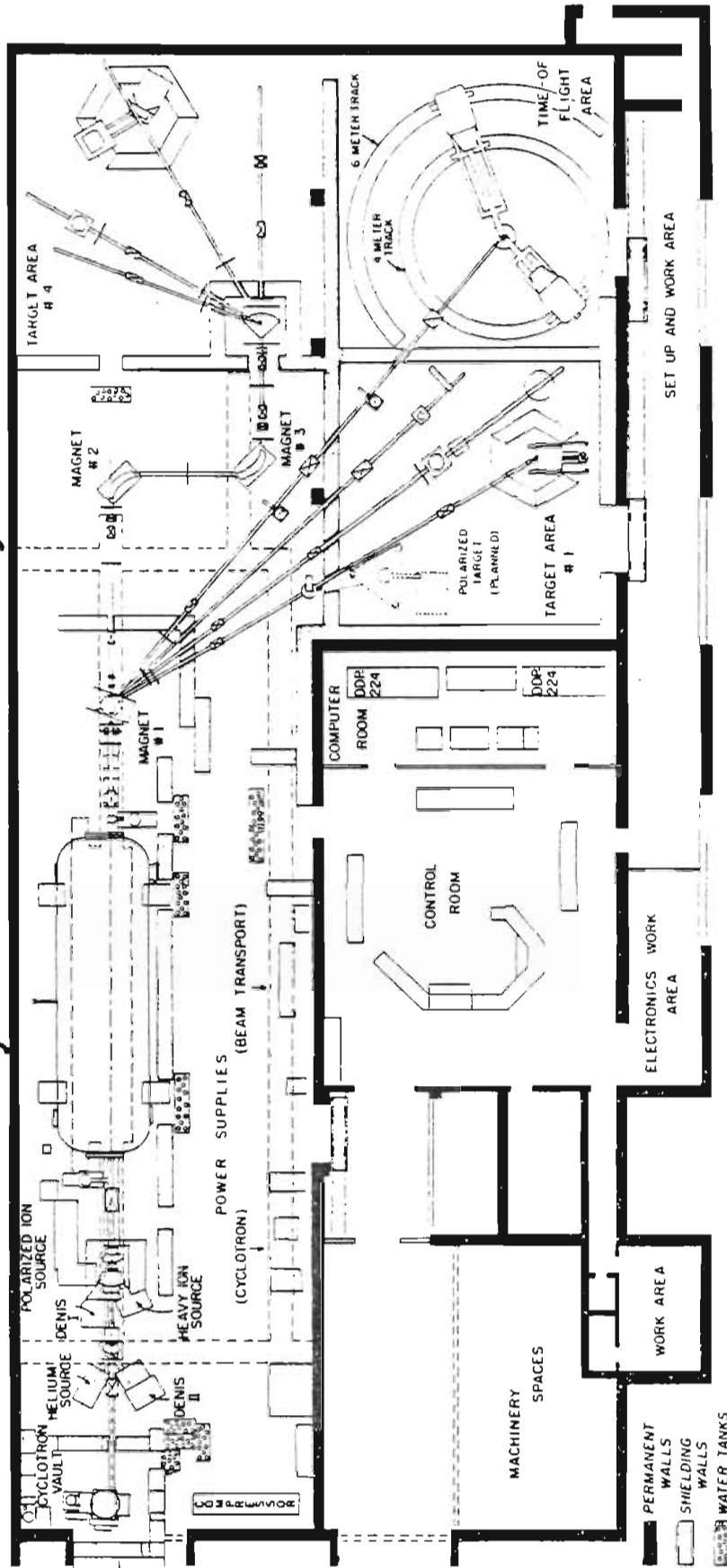


Figure 2-3. The general floor plan of the Triangle Universities Nuclear Laboratory.

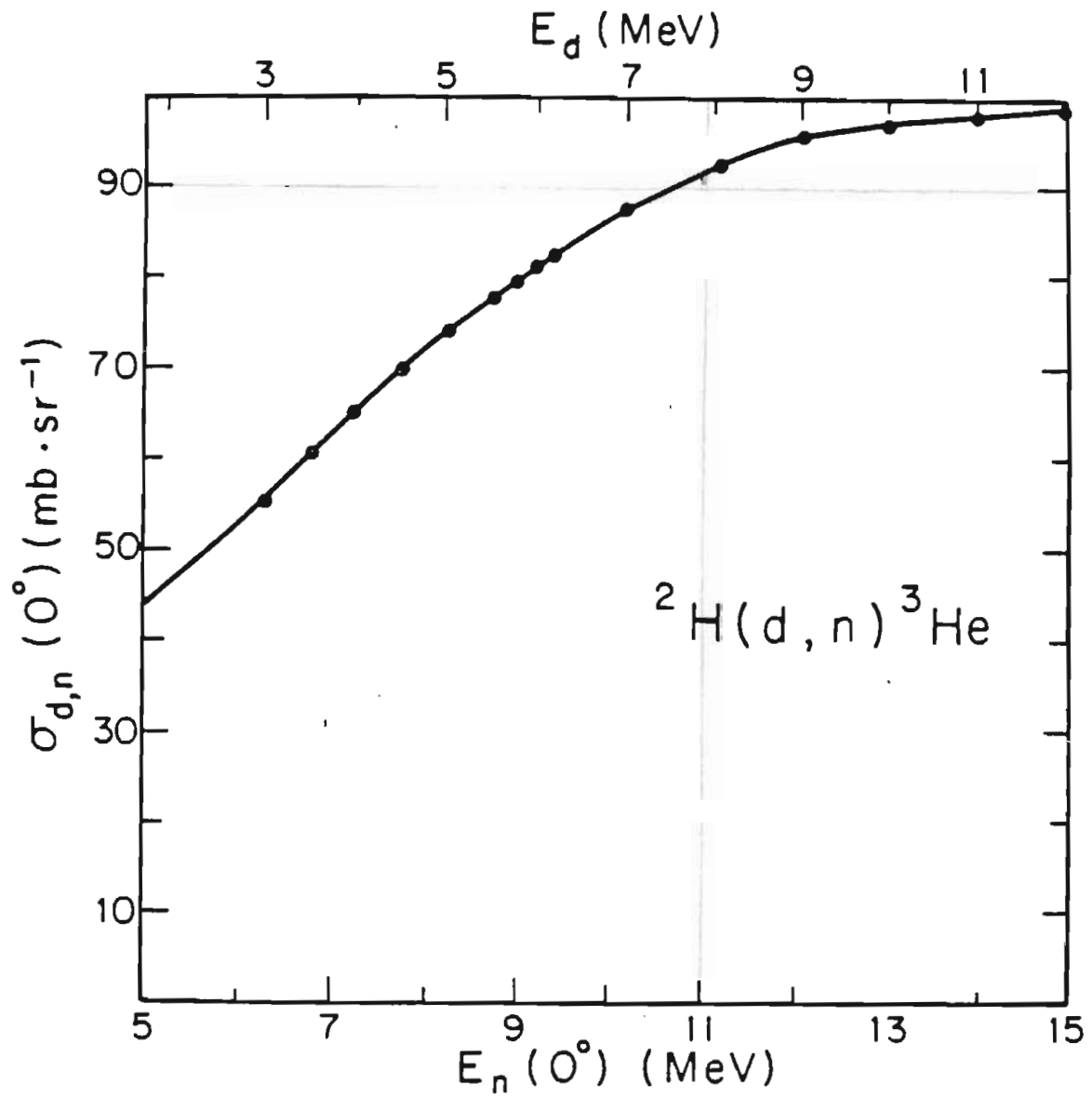


Figure 2-4. $\sigma(0^\circ)$ vs E_d for the reaction $\text{D}(d, n){}^3\text{He}$.

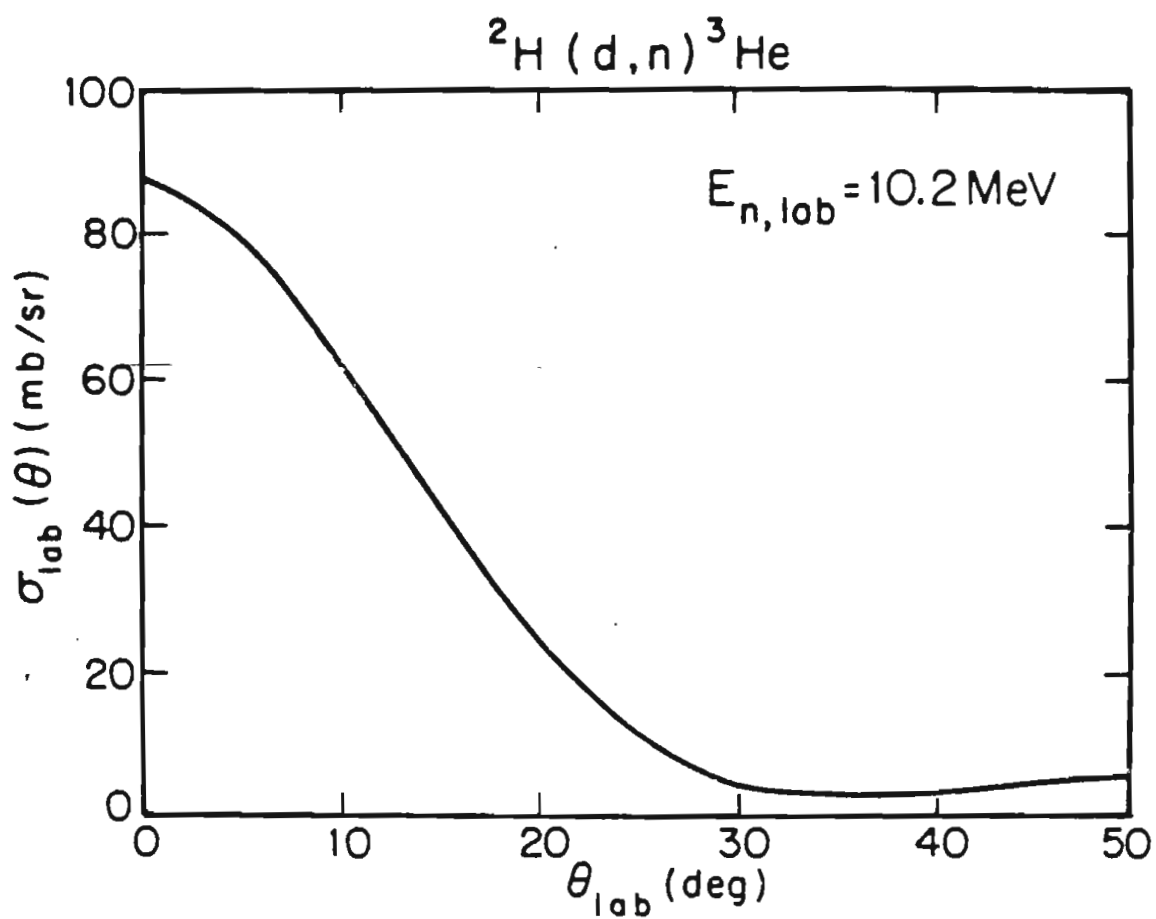


Figure 2-5. $\sigma(\theta)$ vs θ for the reaction $\text{D}(d, n){}^3\text{He}$ for $E_n = 10.2 \text{ MeV}$.

an electron suppressor before entering the gas cell through a 5.7 mg/cm² Havar foil. The gas cell itself is lined with tantalum (see Fig. 2-6). Beam current integration is determined from the total charge integrated on the gas cell. The relative neutron yield of this source reaction is monitored by a liquid scintillator detector located at zero degrees with respect to the incident beam direction.

Another reason for using the $D(d,n)^3\text{He}$ reaction as the source reaction is that the polarization transfer from incident polarized deuterons to the resulting neutrons is on the order of 90%. The exact relationship between these two quantities at zero degrees depends on the polarization transfer coefficients, $K_y^{y'}(0^\circ)$, as well as the tensor analyzing power $A_{zz}(0^\circ)$ of the reaction [Liso75]. The neutron polarization $p_{y'}(0^\circ)$ is given by

$$p_{y'}(0^\circ) = \pm \frac{3}{2} p_3 K_y^{y'}(0^\circ) \left(1 - \frac{1}{4} p_{33} A_{zz}(0^\circ) \right)^{-1} \quad 2-1$$

where \pm refers to spin "up" or spin "down" relative to the reaction plane, and p_3 and p_{33} are the vector and tensor polarizations of the incident deuterons with respect to the axis of quantization at the polarized ion source. $A_{zz}(0^\circ)$ was found to have the almost constant value of -0.46 for $E_d > 3$ MeV, while $K_y^{y'}(0^\circ)$ was found to be a slowly varying function of energy, with

$$K_y^{y'}(0^\circ) = 0.6624 - 0.0032 E_d \quad 2-2$$

where E_d is in MeV. In addition, the zero degree cross section is dependent on the tensor polarization of the incident deuteron beam according to the relationship

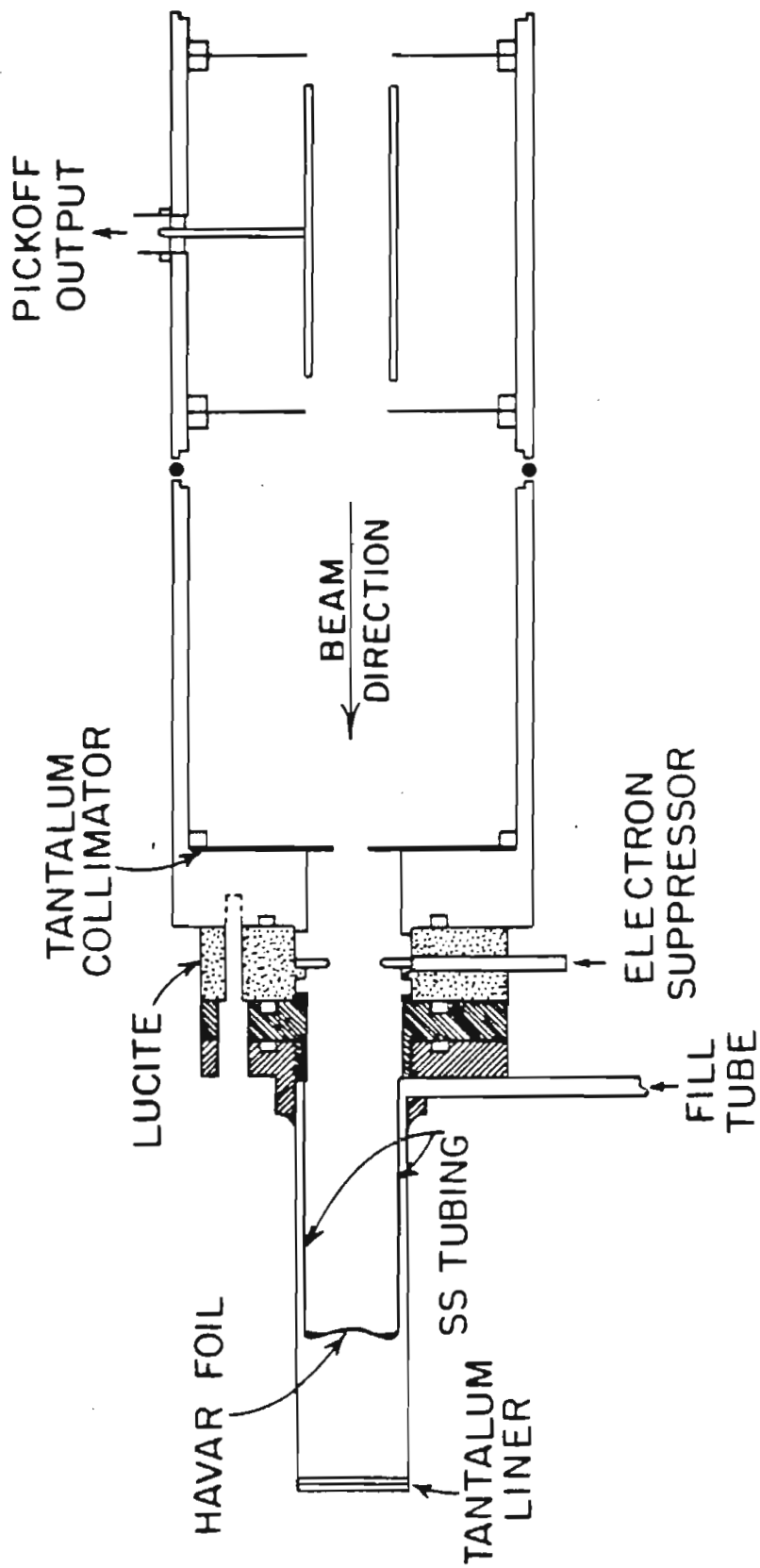


Figure 2-6. Deuterium gas cell.

$$\sigma(0^{\circ}) = \sigma_0(0^{\circ}) \left(1 - \frac{1}{4} p_{33} A_{zz}(0^{\circ})\right) \quad 2-3$$

or,

$$\sigma(0^{\circ}) = \sigma_0(0^{\circ}) (1 + 0.116 p_{33}) \quad 2-4$$

In the experiments reported here, the source was operated such that p_{33} was equal to p_3 . Typically, the neutron polarization, as determined after each individual run by the quench ratio method [Trai74], was found to be about 60%. Under these circumstances, the zero degree cross section is increased by about 7%.

D. Target

The target used for this work is a cylindrical sample of natural calcium, which is 97% ^{40}Ca . The target has a height and a diameter of 1.5 inches. Because of the corrosive interaction of calcium with water vapor in the air, the target was stored under mineral oil for the duration of this study, with almost no noticeable deterioration. The target was suspended by wire such that the distance from the center of the target to the center of the gas cell was 8.9 cm.

E. Detectors

To monitor neutron flux from the source reaction, an NE-213 liquid scintillator detector was placed at zero degrees with respect to the beam direction. Though the room background of neutrons coming from reactions other than the source reaction seems to affect the

counts seen by this detector, it was found that by stripping away the pedestal under the main neutron peak, fairly consistent count rates could be obtained (see Fig. 2-10). Since the analyzing power for the source reaction is zero at zero degrees, a second monitor, located off-axis, was occasionally used to check the polarization of the incident deuteron beam.

During the early stages of this work, the γ -rays were detected by a single 10 x 10 inch Bicron NaI detector located on the right of the beam leg. This detector was complemented by the addition of a second similar detector on the left side of the beam leg (Fig. 2-7). Each crystal is viewed from the rear by a circle of six RCA 9575 photomultiplier tubes, the signals from which are mixed and sent into the electronics. Both detectors are surrounded by NE-110 anticoincidence shields for the rejection of cosmic rays and secondary γ -rays. The shields are each viewed by eight XP1031 photomultiplier tubes positioned along their sides and backs. Both assemblies are enclosed by a layer of lead blocks for passive shielding against γ -rays created in the shielding itself. A layer of wax doped with lithium carbide shields the detectors from neutrons. For extra protection from thermal neutrons the right detector has an additional sheet of cadmium metal between the lead and the wax, while the left detector has a layer of boron carbonate in this place. A lead collimator is located in front of the crystal so that the entire back face of the crystal is illuminated when it is a distance of 41.75 inches from the target. Further shielding is provided by tungsten shadow bars positioned to prevent neutrons from the source reaction

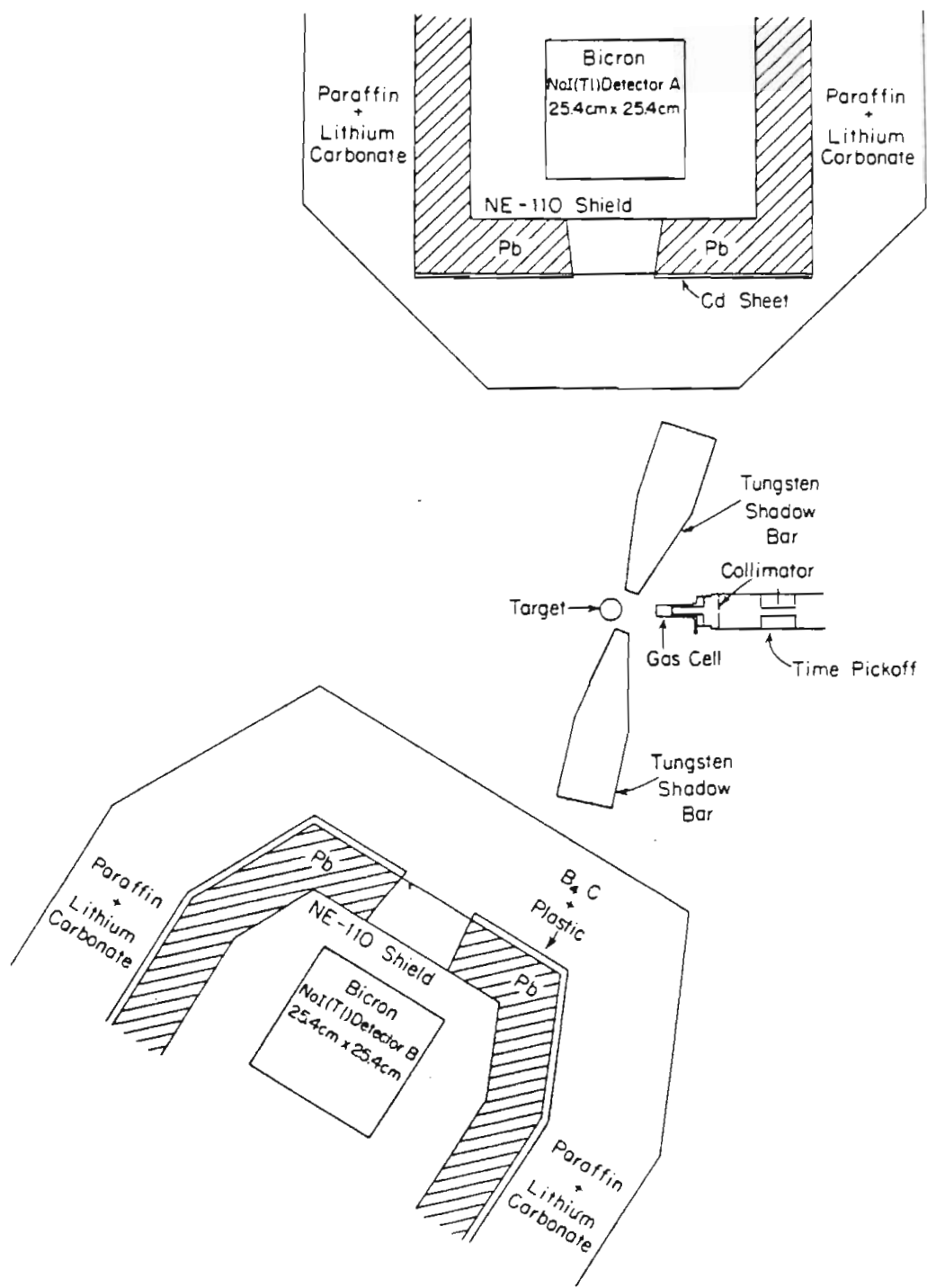


Figure 2-7. Detector geometry.

from entering the detectors. Both detectors sit on carriages and can be rolled away from the target if lower count rates are desired. The carriages can also be rotated to position the detectors at different angles. Practically, the range of angles is from 35 to 150 degrees for each detector.

F. Electronics and Data Acquisition

1. Monitor Electronics

A block diagram of the monitor electronics is given in Fig. 2-8. There are three stages of these electronics: the first provides a lower level threshold on the linear signal which fixes the lowest neutron energy that can be detected; the second performs pulse-shape-discrimination (PSD) to distinguish neutrons from γ -rays; and the third generates, for neutron events, a time-of-flight (TOF) signal for processing by the computer.

In the first stage, the dynode (linear) signal is fed into a delay line amplifier, which generates both a unipolar and bipolar output pulse. The bipolar pulse is sent to a timing single channel analyzer (SCA) with both an upper and a lower level discriminator to provide an energy window on the events allowed in the spectrum. For this experiment, the upper level is set near its maximum value. The lower level is set on the Compton edge of ^{137}Cs , corresponding to 490 keV γ -rays. This is equivalent to the scintillator response for approximately 2 MeV neutrons. The gain on the delay line amplifier is

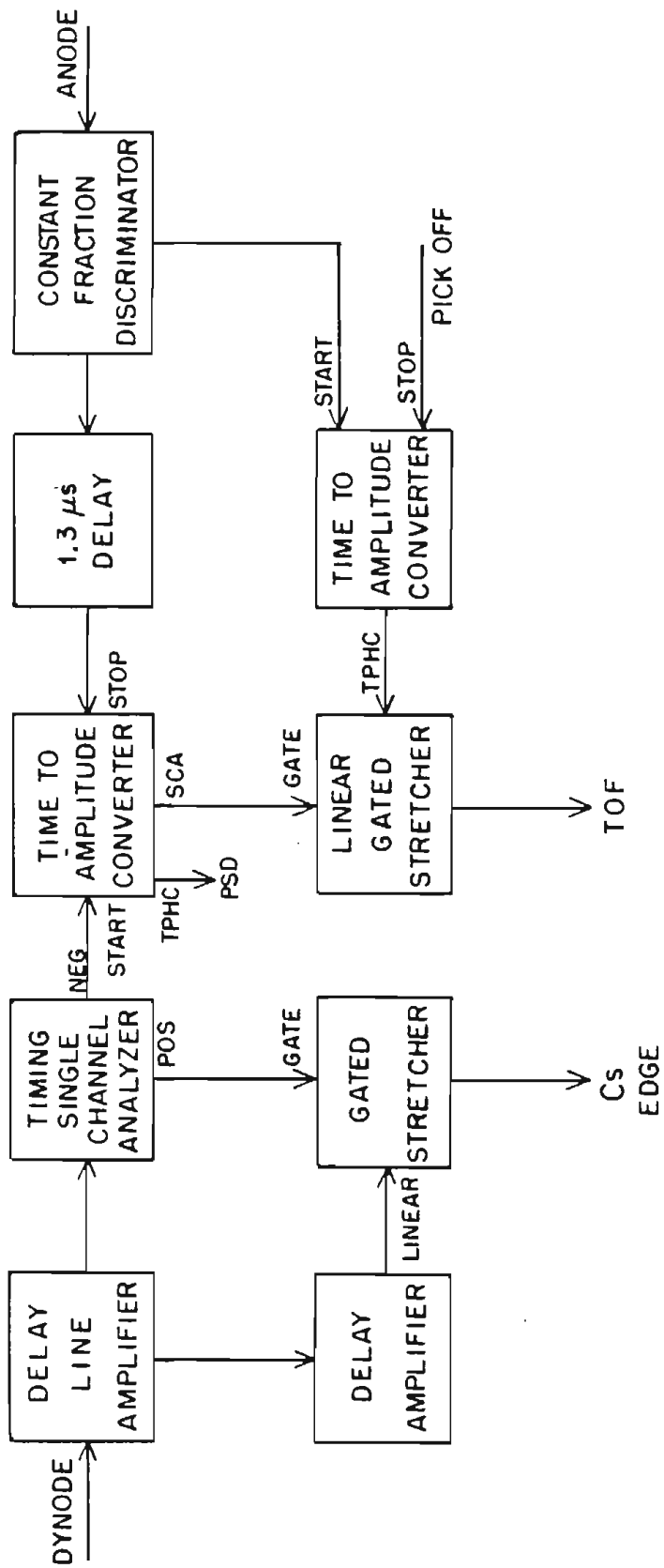


Figure 2-8. A block diagram of the monitor electronics. Outputs are labeled according to their function in the circuit. 20

set so that the smallest pulses accepted by the single channel analyzer are less than two volts high. This is to ensure that the higher energy signals observed during an experiment fall into the linear range of the amplifiers in the circuit. The positive output of the SCA is used to gate the delayed unipolar signals from the delay line amplifier at the linear gated stretcher. The linear output from the gated stretcher is used only as an aid in setting the SCA discriminator.

In the next stage of the electronics, pulse-shape-discrimination (PSD) takes place. Liquid scintillators have different responses to γ -rays (Compton electrons) and neutrons (recoil protons). The shape of the light pulse, which depends on the rate of energy loss of the particles, is approximately the sum of two exponential functions, having decay times of two to five nsecs and of 100 to 200 nsecs. For a given total energy loss, proton pulses have a smaller fast component than electron pulses. It is this feature that makes PSD possible in organic scintillators.

The delay line amplifier integrates over these different response times, and produces signals with different rise times for neutrons and γ -rays. When the delay line amplifier is operated in the double delay line mode, the cross-over time of the resulting bipolar pulse is related to the rise time of the integrated signal. Therefore, the timing signal generated by the timing single channel analyzer on the basis of the cross-over is also related to the rise time. The anode (fast) signal from the scintillator goes into a constant fraction

discriminator, generating a fast negative logic signal. The discriminator is set as low as possible to obtain good timing. When the timing signal from the timing single channel analyzer is fed to the start of a time-to-amplitude converter (TAC), and the signal from the constant fraction discriminator (delayed by approximately 1.3 usecs) is input to the stop of the TAC, the resulting time-to-pulse-height (TPHC) output of the TAC is a pulse directly related to the shape of the signal from the scintillator. If these linear signals are fed to the computer and a spectrum generated, there are two peaks, one corresponding to neutrons and the other to γ -rays. It is thus possible to set a window on the neutron peak with the internal single channel analyzer (SCA) of the TAC, and to use the output as a gate in the last stage of the electronics. An example of a PSD spectrum is shown in Fig. 2-9.

The final function of the monitor electronics is to generate for neutron events a signal which is proportional to the neutron time-of-flight from the source (gas cell) to the detector. The fast logic signal from the constant fraction discriminator described above is used as the start signal of a second TAC, and the fast negative signal generated by the beam pick-off is used as the stop to the TAC. The linear TPHC output of this second TAC is fed to the linear gated stretcher gated by the PSD single-channel-analyzer output of the first TAC. In this way, only neutron events are stored by the computer. A typical time-of-flight spectrum is shown in Fig. 2-10. The neutron peak from the source reaction, ${}^2\text{H}(d,n){}^3\text{He}$, is clearly visible; the rounded peak to the left is due to neutrons coming from the deuteron

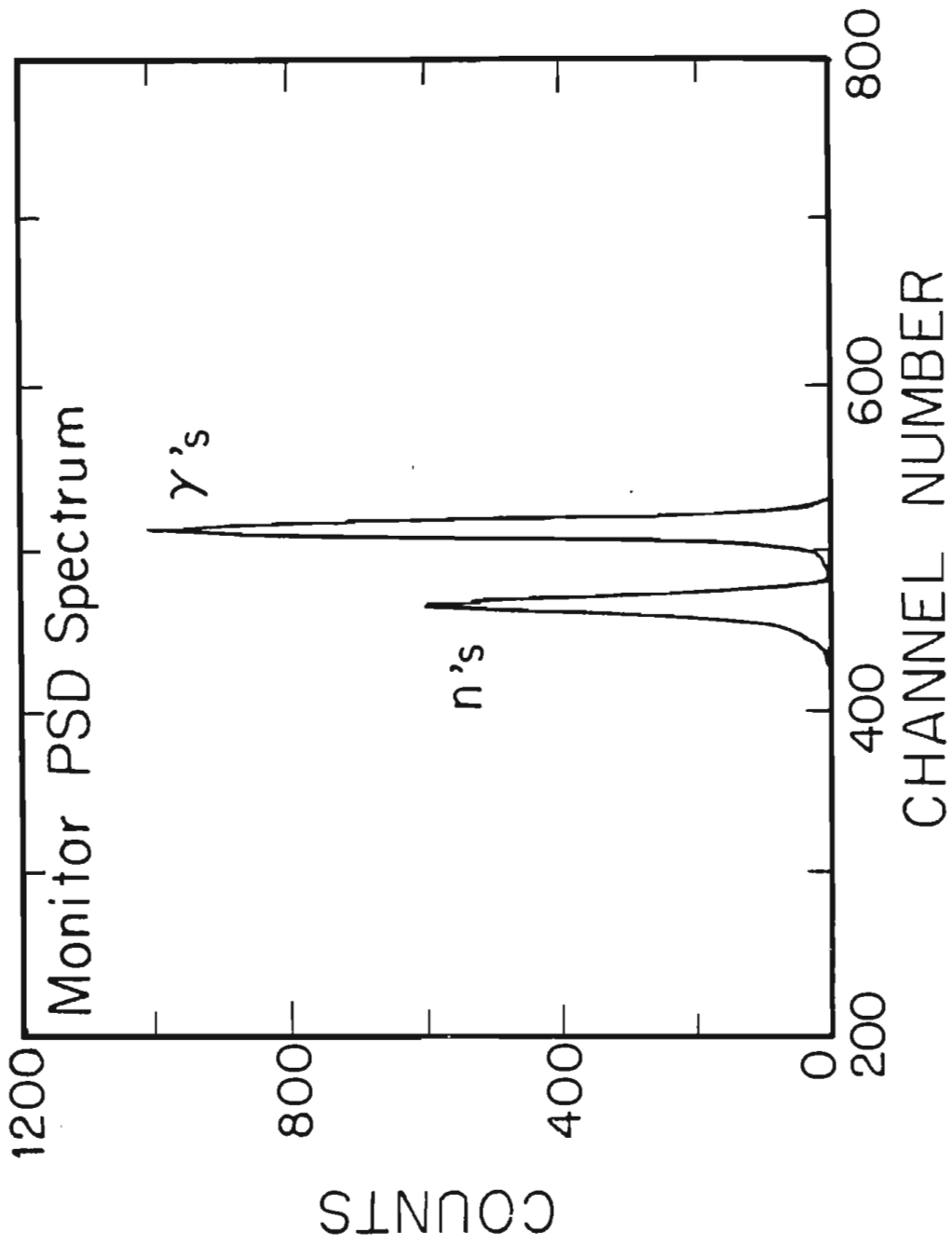


Figure 2-9. A typical monitor pulse-shape-discrimination spectrum.

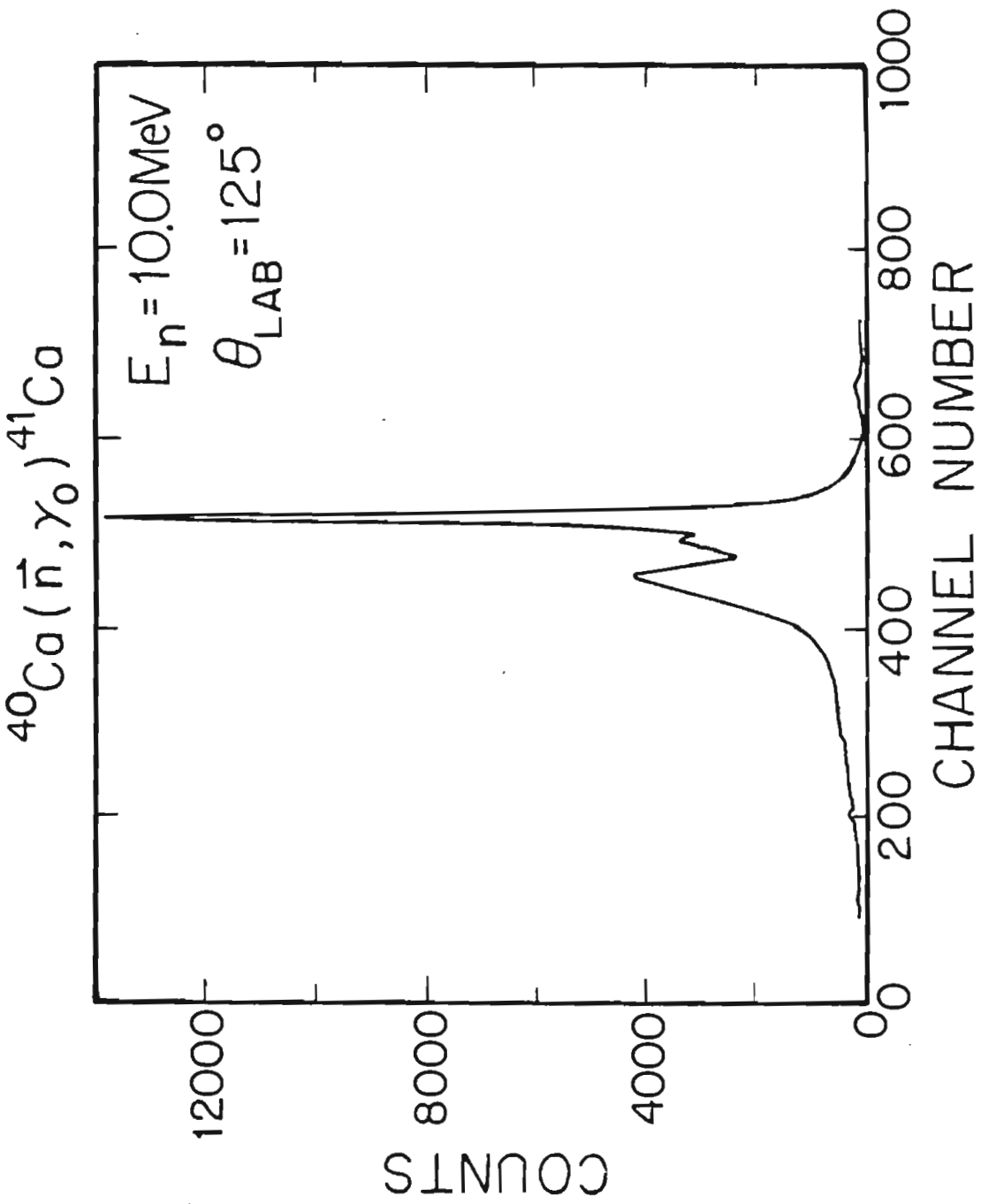


Figure 2-10. A typical monitor time-of-flight (TOF) spectrum.

breakup reaction. After correcting for the background, the number of counts in the source neutron peak is summed to produce the monitor yield.

The number of pulses at the output of the timing single channel analyzer is counted with an on-line scaler during the run. The ratio of the counts in this scaler to the total number of counts in the spectrum provides a measure of the dead time in the monitor circuit as well as in the computer interface. Typical values of the dead time were less than 10 percent and were used to correct the monitor counts.

2. NaI Detector Electronics

As in the case of the monitor electronics, the NaI detector electronics can be divided into several parts according to their functions in the circuit: the circuitry dealing with the processing of energy signals, the time-of-flight electronics, and the coincidence circuitry. A block diagram of the electronics for both the shield and the crystal is shown in Fig. 2-11. Each part of the electronics will be described separately here.

As an example of the final result of the signal-processing, a γ -ray spectrum is given in Fig. 2-12, where the peak corresponding to the γ -ray transition to the ground state is clearly visible and separated from the peaks due to the transitions to the excited states. The peaks in this spectrum correspond to transitions to the levels presented in the energy level diagram of Fig. 2-13. The

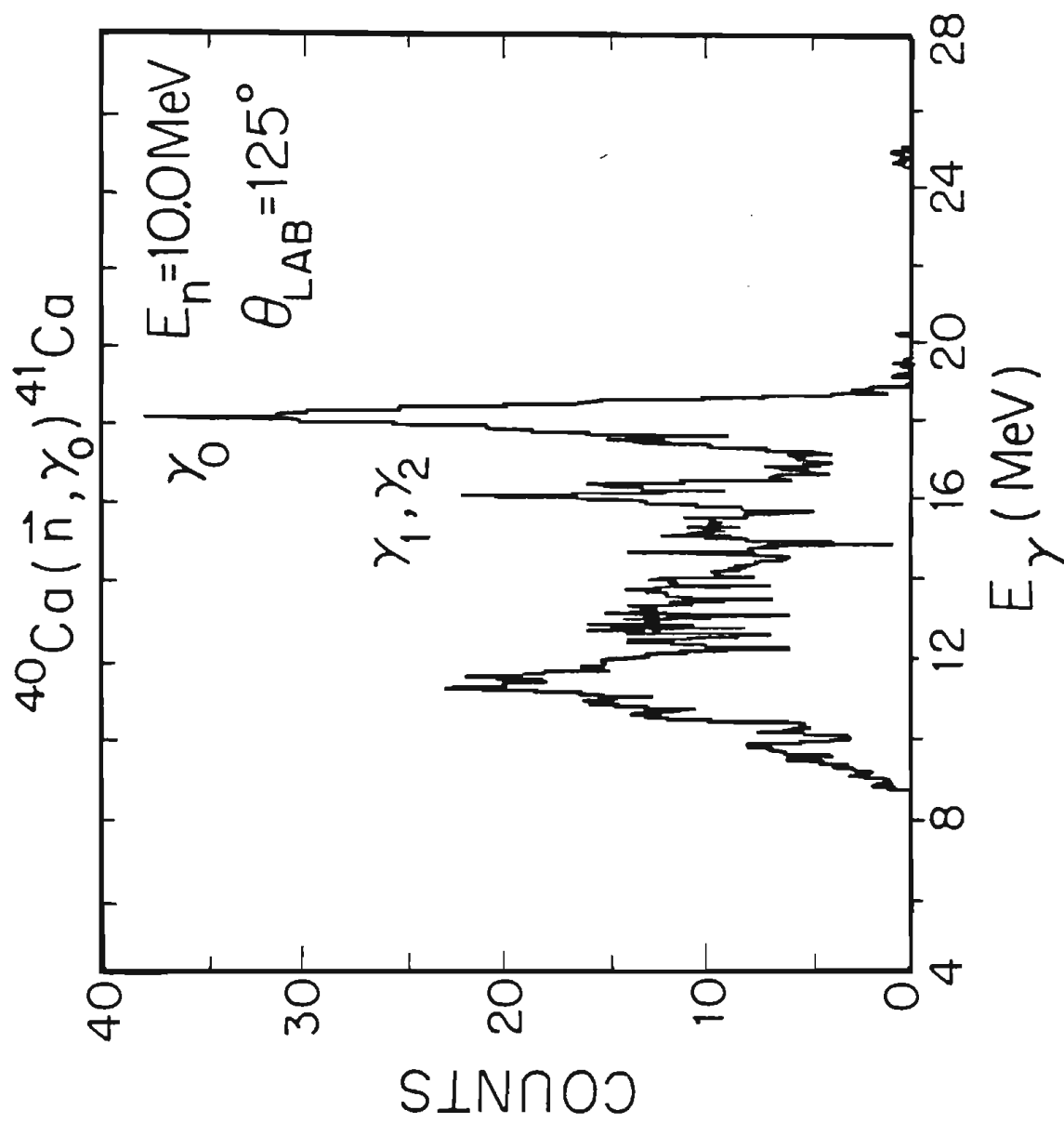


Figure 2-12. A typical γ -ray spectrum.

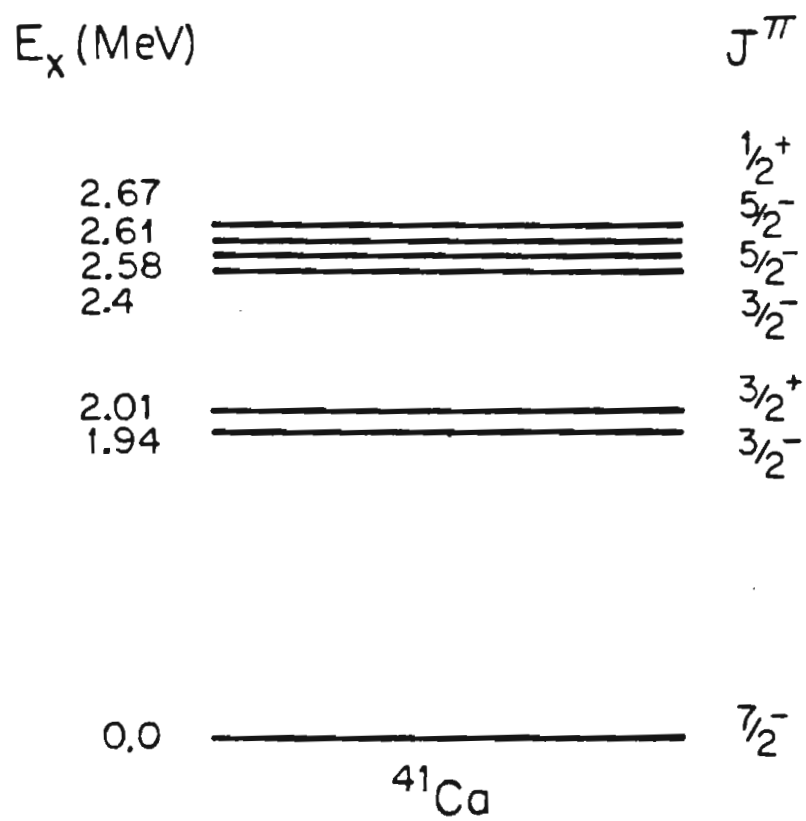


Figure 2-13. The energy levels of ^{41}Ca .

particular spectrum shown was taken at a neutron energy of 10 MeV and at $\theta = 125^\circ$.

The pulses that come from the six RCA 8575 photomultiplier tubes which view the NaI crystal are first mixed and summed, and then clipped to a width of 350 nsecs. The clipped signals are then fanned out into two branches. The first branch is the input for the fast linear gate. The signal in the second branch is amplified with a fast amplifier and passed to a leading edge discriminator which provides both timing and a lower level threshold. The output from the leading edge discriminator is used to trigger a gate generator which is held open for 10 μ secs. This gate generator produces two pulses, one of which is used to open the fast linear gate in the first branch and the other which provides a gate (R1) for a 12 channel ADC which is interfaced to the VAX computer. The output of the fast linear gate is amplified and shaped, and then sent to one input of the 12 channel ADC. An on-line scaler counts the total number of pulses (R1) produced by the gate generator, and this number, along with the total number of counts in the spectrum gives an estimate of the dead time in the system. Typical dead times were less than one percent. It should be noted that two features of this circuit are designed to prevent pulse pile-up. First, the fast linear gate is only opened for 400 nsecs, and only if there has been no other gate signal for 10 μ secs. Second, two low energy signals can not pile up and cause the leading edge discriminator to trigger if they are separated by about 40 nsec, a time determined by the shaping in the fast linear amplifier. A picture of the "raw" spectrum produced in this phase of the

electronics, without the coincidence and timing requirements of the other two stages of the electronics, is shown by curve A in Fig. 2-14.

The output of the leading edge discriminator is also used as the start signal to a TAC, while the signal from the beam pick-off is used as the stop. The linear output of the TAC is sent to another input of the 12 channel ADC. A typical time-of-flight spectrum for the NaI detectors is shown in Fig. 2-15. The γ -ray peak is clearly separated from the neutron peak. By setting a gate on the γ peak, it is possible to eliminate time-uncorrelated events. Curve B of Fig. 2-14 illustrates the effect of this time requirement on the original spectrum. The total number of counts in the spectrum is now only about 15 percent of the number without this time requirement, with the most obvious effect being the elimination of a large fraction of the cosmic ray background at high energies and the considerable low energy γ -ray background from neutron induced events. The peak of interest is considerably more visible in this case.

The purpose of the coincidence circuit is to eliminate the rest of the cosmic rays in the spectrum, as well as counts from escape events and scattered γ -rays. These types of events produce simultaneous pulses in both the anticoincidence shield and the central crystal. After the signals from the eight XP1031 photomultiplier tubes which view the shield are mixed and summed, the sum is suitably amplified and passes to a leading edge discriminator. The outputs of this leading edge discriminator and of the NaI leading edge

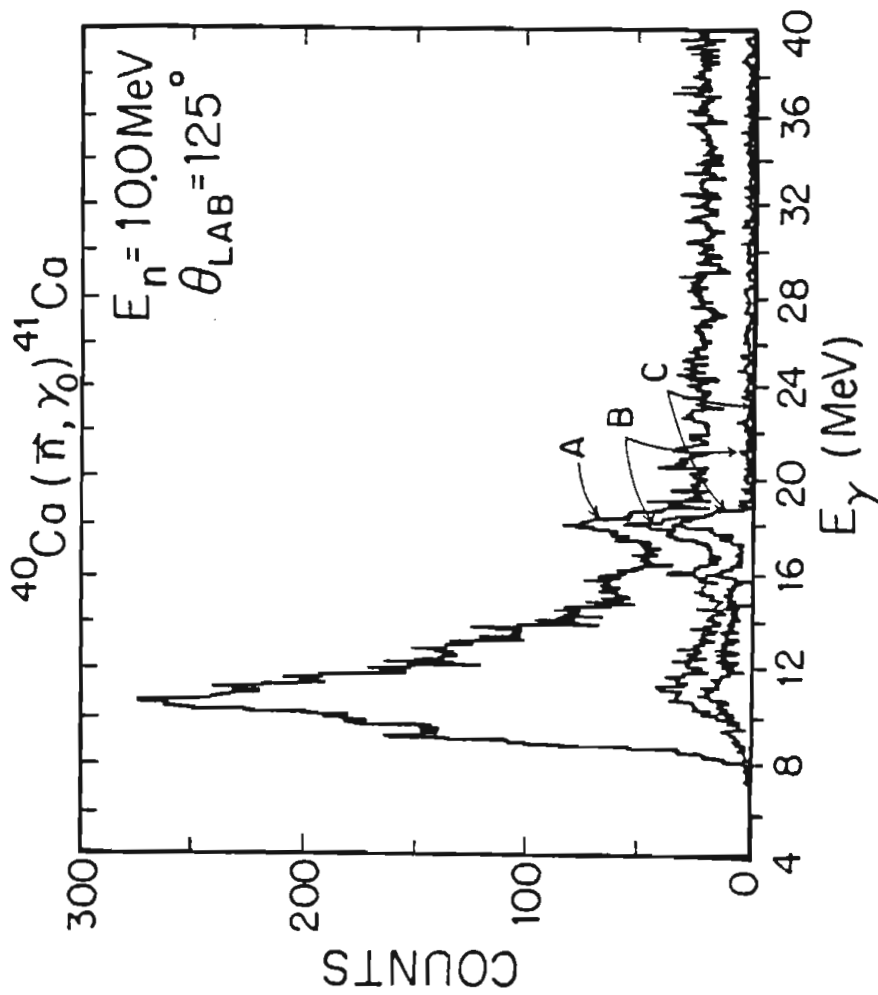


Figure 2-14. A typical γ -ray spectrum at several stages of processing. Curve A is the "raw" spectrum; Curve B is the same spectrum gated with a time-of-flight requirement; Curve C is the same spectrum, with both a timing requirement and coincidence rejection. The spectrum of curve C is the same as that of Fig. 2-12.

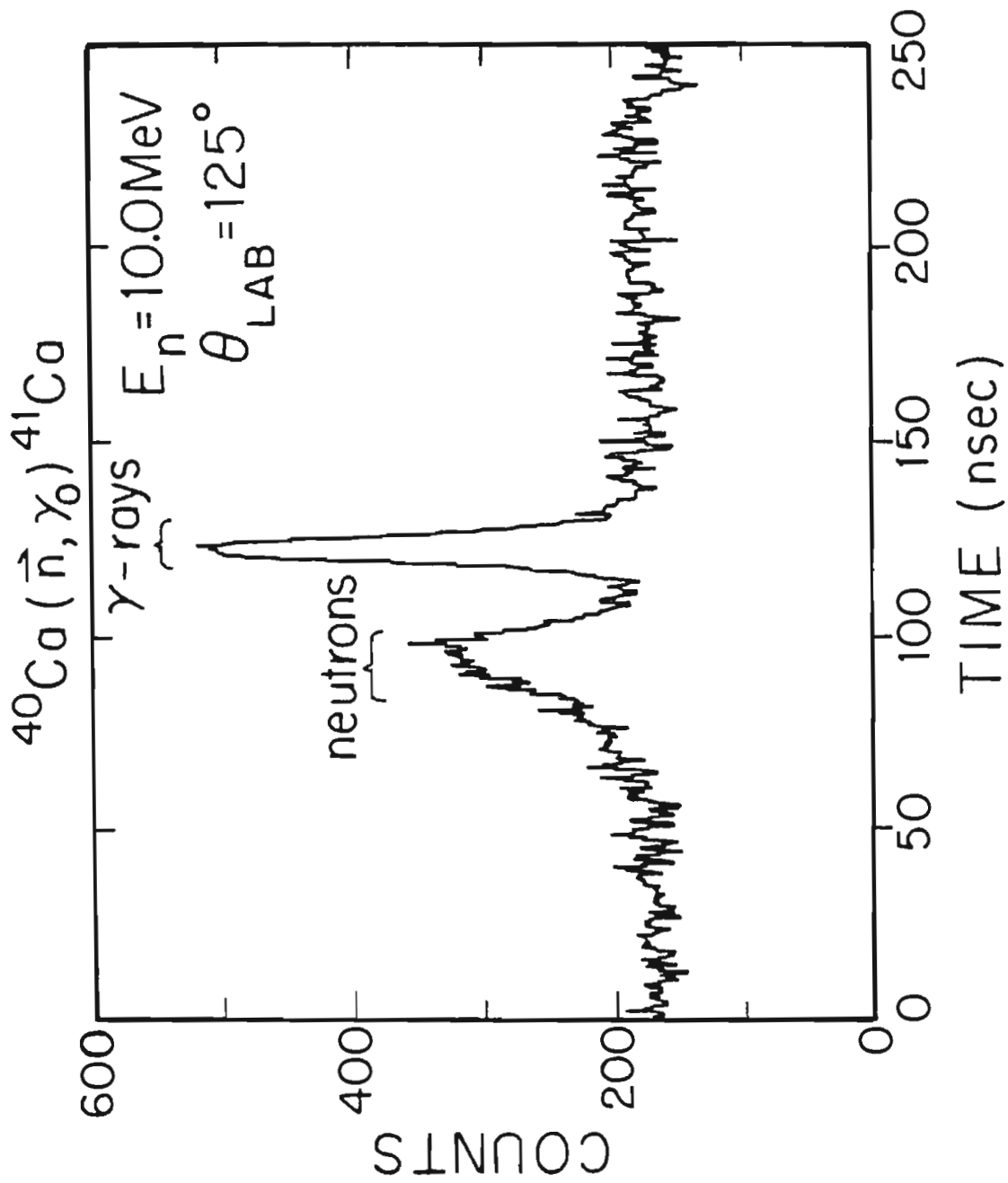


Figure 2-15. A typical NaI time-of-flight (TOF) spectrum.

discriminator are both fed to a fast coincidence module. The resolving time of the coincidence circuit is set at about 60 nsec. The output of this module provides a logic pulse (R2) to the computer interface to signal that the data is a coincidence event and is to be stored in a separate reject spectrum. This same logic pulse (R2) is counted by an on-line scaler. It is possible, however, that a true event in the central crystal could be detected at the same time as an uncorrelated event in the shield, and should not be rejected. The rate of such accidental coincidences is determined by another fast coincidence module in the circuit. The accidental circuitry is identical to the coincidence electronics just described, except that the pulse from the shield is delayed by 250 nsecs. This gives an estimate of the number of random coincidences between the shield and the NaI crystal. The number of accidentals depends on the beam current, the position of the detectors, and the gain on the shields. For this work, typical accidental rates were about 7% of the true coincidence rates. Rarely was the accidental rate allowed to exceed 10% of the coincidence rate. The time-correlated pulses which were not rejected by the coincidence circuitry were displayed in a final "accept" spectrum. The effect of the rejection of the coincidences is clear from curve C in Fig. 2-14, which shows the final product in relation to the original ungated spectrum. (Note that curve C lies along the x-axis above 20 MeV.) The total number of counts finally accepted as true events is only about 7% of the number in the original spectrum. The spectrum represented by Curve C is the same one presented in Fig. 2-12. Now, with both the timing and anticoincidence

requirements placed on the spectrum, there is essentially no background in the area of the peak, and the peak is cleanly separated from the rest of the spectrum.

The monitor and NaI ADCs are connected via a CAMAC system, to a MBD-11 (microprogrammed branch driver) which is then connected to a VAX 11/780 computer. A detailed description of both the hardware and software components of this system may be found elsewhere and will not be described here [Robe81,Goul81,King81,Holz81]. The scalers and the spectra are stored in the VAX, and are displayed live during the run. All data are dumped on magnetic tape for future off-line analysis.

3. Experimental Results

A. Absolute Cross Section Measurements

The total number of counts observed at a given energy and angle is related to the absolute cross section by:

$$N_{\gamma} = \frac{N_t N_d n_g t \sigma_n(0^{\circ}) \sigma(\theta, E) \epsilon(E, \text{gain}) \Omega}{r_{gs}^2 F(\theta) \text{Acci}} \quad 3-1$$

The parameters in this expression are presented in Table 3-1, along with some typical values.

A detailed description of the Monte-Carlo code, FIXER, used to generate finite geometry corrections to the data, can be found elsewhere [Jens81]. This code includes the effects of the finite size of the experimental apparatus, the neutron and γ -ray attenuation, and neutron multiple scattering. The geometry used to model the gas cell, target, and detector is shown in Fig. 3-1. The values of the experimental parameters pertinent to the finite geometry calculations can be found in Table 3-2. The program averages the neutron flux over the volume of the target and the γ -ray flux over the area of the back face of the detector. In addition, the program considers the widening of the deuteron beam in the gas cell, and a Gaussian spread in the energy of the deuterons as they pass through the cell. Gamma-ray

Table 3-1 Absolute Cross Section Parameters

Symbol	Description	Typical Values
N_γ	number of γ -rays detected at a given energy and angle	0.33 counts/ μ C of beam at $E_n = 10$ MeV (high rejection)
$\sigma(E, \theta)$	absolute differential cross section at given energy and angle	5 - 15 μ b/sr
Acci	correction due to accidental coincidences = (1 + acci rate/coin rate)	1.02 to 1.08
$F(\theta)$	finite geometry correction factor	1.2 to 1.6 (see Table 3-3 and Fig. 3-2)
$\sigma_n(0^\circ)$	$D(d, n)^3\text{He}$ differential cross section at 0°	87.3 ± 1.3 mb/sr at $E_n = 10$ Mev (see Fig. 2-4)
Ω	solid angle acceptance of detector at 41.75 inches to rear face	45×10^{-3} sr
r_{gs}	distance from center of gas cell to center of target	8.9 cm
$\epsilon(E, \text{gain})$	absolute efficiency of detector	0.21 (see Figs. 3-3, and 3-4)
n_g	density of deuterium in gas cell (atoms/cm ³)	1.56×10^{20} at 42.7 psia

Table 3-1 (cont.) Absolute Cross Section Parameters

Symbol	Description	Typical Values
t	length of the gas cell	2.54 cm ✓
N_t	number of atoms in the target	1.014×10^{24} ✓ 1×10^{24} 1.0119×10^{24}
N_d	total number of deuterons incident on gas cell	7.5×10^{15}

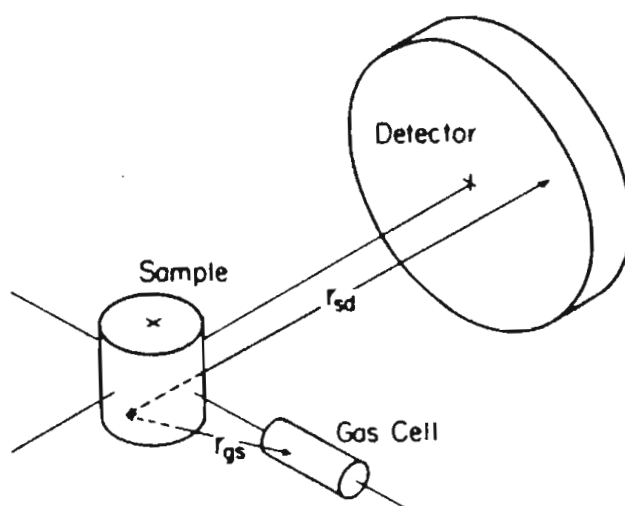


Figure 3-1. Model for the geometry used in the finite geometry corrections to the data.

Table 3-2

Typical Experimental Parameters

Parameter	Value
beam intensity	250 nA unpol 100 nA pol
polarization	60%
gas cell pressure	28.0 - 90.0 psia
diameter of target	1.5 in
height of target	1.5 in
size of NaI crystal	10 in × 10 in
distance from center of target to front face of detectors	25.0 - 48.84 in
angular range of detectors	$\approx 35 - 150^\circ$
resolution	$\approx 6.0\%$ at 4.4 MeV
dead time	$< 1.0\%$

attenuation in the target is taken into account by using the total γ -ray cross section from Storm [Stor70]. The neutron total cross section and the neutron elastic cross section used to calculate neutron attenuation and multiple scattering, respectively, came from the ENDF/B-V library [Garb76].

Basically, the program calculates finite geometry effects as follows. Using the cross section and the angular distribution of the source reaction, and the energy spread of the deuterons in the gas cell, the program traces the path of a neutron produced at a random point in the gas cell which reacts at a distance of r_{gs} at a random point in the target. A γ -ray produced at this site is assumed to be detected at a distance of r_{sd} at a random point in the detector. The attenuation of neutrons and γ -rays in the target is taken into account, and any elastically scattered neutrons reenter the calculation via multiple scattering. The differential count rate is integrated over the gas cell, the sample, and the area of the face of the detector. This is done for each angle of the detector.

The generation of the corrected data on the basis of these considerations will be discussed later, in § 3-C. At present, it is only necessary to point out that the calculation of the correction factor at a particular neutron energy requires an initial guess of the angular distribution of the capture reaction at that energy, along with the values of the elastic and total neutron cross sections at the energy. At energies where angular distributions were measured, the required parameters could be taken from the experimental data. Where

there were no angular distribution data, the necessary information came from direct-semidirect model calculations. The correction factor for $\theta = 90^\circ$ is shown in Fig. 3-2, where the smooth curve is the results of the DSD model calculations and the solid points are the results of using the experimental angular distribution. At $E_n = 13$ MeV where the discrepancy between these two methods is largest, the difference is less than two percent, much less than the other errors in the experiment. The overall shape of the data in the figure reflects the general trend of the elastic and total cross sections used in the calculations. A numerical tabulation of the factors in Fig. 3-2 can be found in Table 3-3.

The absolute efficiency of the γ -ray spectrometers, ϵ , is defined as the ratio of the number of counts in the full-energy peak in the accepted spectrum to the total number of γ -rays entering the spectrometer collimator. For this experiment, the full-energy peak is considered to extend from the high energy edge of the peak to two widths (FWHM) below the centroid of the peak. The energy dependence of the efficiency is determined by three factors: 1) the ratio of the counts in the full-energy region to the total response function, 2) the fraction of the counts in the full-energy region which are rejected by the anticoincidence shield, and 3) by the attenuation of the γ -rays in the material between the target and the NaI crystal. The procedure used here was to measure the efficiency at one energy ($E_\gamma = 15$ MeV) and then to determine a correction factor based on the energy dependent effects.

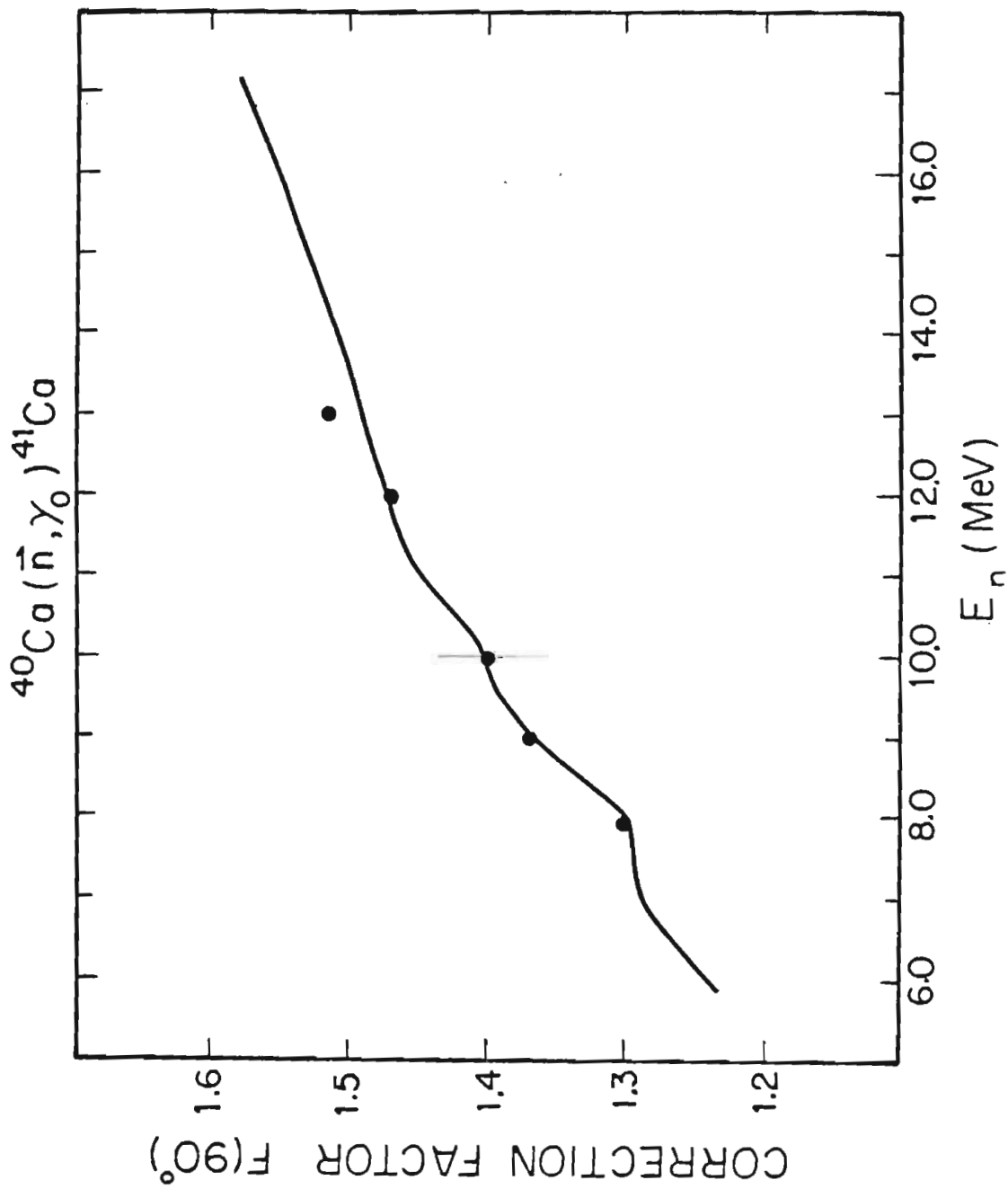


Figure 3-2. Finite geometry correction factors as a function of E_n , calculated on the basis of the data (dots), and on the basis of the DSD model (solid line).

Table 3-3

Finite Geometry Correction Factors $F(\theta)$
at 90° as a Function of Neutron Energy

E_n	Factor
6.0	1.240
6.2	1.250
6.4	1.260
6.6	1.270
6.8	1.276
7.0	1.285
7.2	1.290
7.4	1.292
7.6	1.295
7.8	1.295
8.0	1.300
8.2	1.310
8.4	1.325
8.6	1.340
8.8	1.355
9.0	1.370
9.2	1.375
9.4	1.385
9.6	1.392
9.8	1.398
10.0	1.400
10.2	1.410
10.4	1.421
10.6	1.430
10.8	1.440
11.0	1.450
11.2	1.455
11.4	1.456
11.6	1.465
11.8	1.470
12.0	1.470
12.2	1.475
12.4	1.480
12.6	1.485
12.8	1.490
13.0	1.515
13.25	1.494
13.5	1.498
14.0	1.507
14.5	1.518
15.0	1.528
15.5	1.541
16.0	1.551
16.5	1.565
17.0	1.575

The efficiency at $E_\gamma = 15$ MeV was measured using the $^{12}\text{C}(p, \gamma_0)^{13}\text{N}$ reaction, since the thick-target γ -ray yield from the 15.07 MeV level in ^{13}N has been accurately measured as $(6.83 \pm 0.22) \times 10^{-9}$ γ -rays per incident proton [Marr75]. This was done by measuring the yield at 125° or at 55° with a 50 keV thick target and comparing the observed yield to the known value. At a fixed E_γ , it is possible to change the efficiency by varying the fraction of the counts in the full-energy region that are rejected by the shield electronics. In the present system this is accomplished by varying the gain on the fast amplifier which comes before the shield discriminator (see Fig. 2-11), while keeping the discriminator level and the photomultiplier tube gains fixed. Fig. 3-3 shows $\varepsilon = \varepsilon(\text{gain})$ at $E_\gamma = 15$ MeV for one of the γ -ray spectrometers. In general, the shield is operated in either a high (gain=80) or a low (gain=4) rejection mode. All data included in this work were taken in the high rejection mode. As seen from the figure, for gain = 80, $\varepsilon(\text{gain}) = 0.208 \pm 0.012$.

The efficiency at other energies can be expressed as $\varepsilon(E_\gamma) = \varepsilon(15) * f(E_\gamma)$, where $f(E_\gamma)$ is determined by measuring the energy dependence of the three factors discussed above. The fraction of the total response appearing in the peak region was found to be constant over the energy region of current interest [Hayw79]. Therefore, $f(E_\gamma)$ depends only on the absorption of the material in front of the crystal, and the shield rejection rate [Well80]. The results of measurements of the absorption and of the rejection rate, along with $f(E_\gamma)$ are shown in Fig. 3-4.

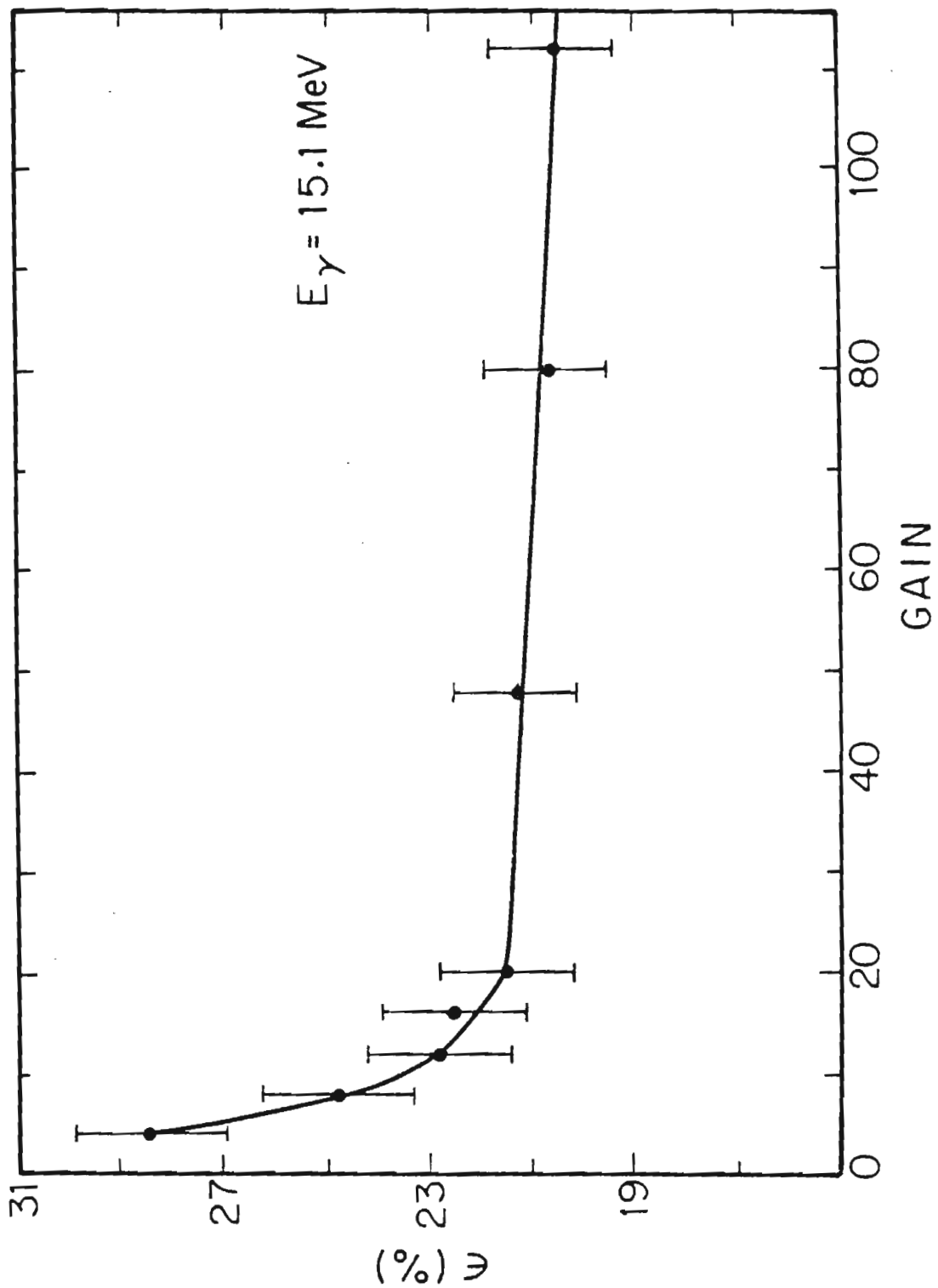


Figure 3-3. Efficiency of one of the NaI detectors as a function of gain for $E_\gamma = 15 \text{ MeV}$.

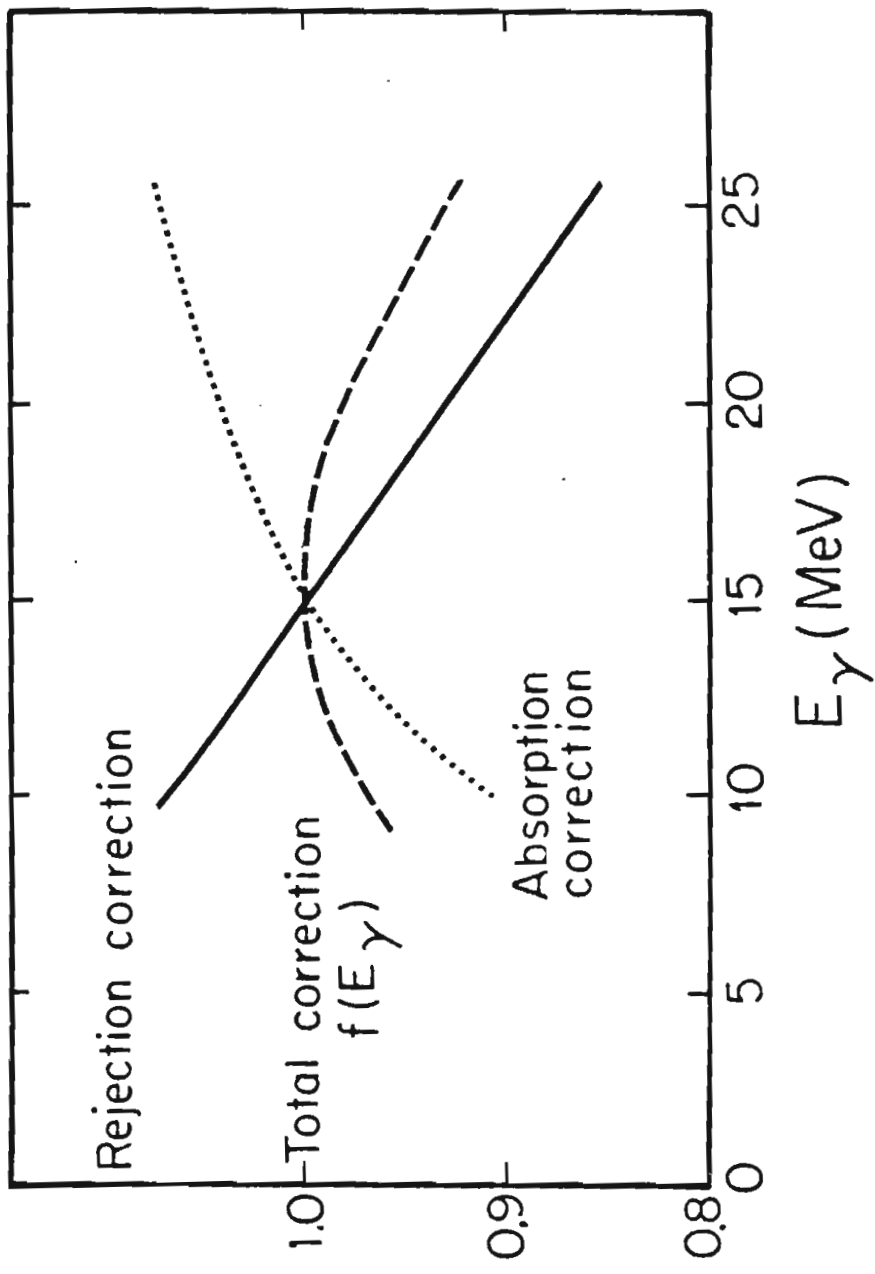


Figure 3-4. Efficiency factor $f(E_\gamma)$ as a function of E_γ . The total energy dependence of the efficiency is given by $\epsilon(E_\gamma) = \epsilon(E_\gamma = 15 \text{ MeV}) * f(E_\gamma)$. 46

The response function was obtained using a standard line shape from previous $T(p, \gamma)^4\text{He}$ measurements and was used in summing all other spectra. The width of a peak was used to determine the summing region of a particular spectrum.

The absolute cross section of the $^{40}\text{Ca}(n, \gamma)^{41}\text{Ca}$ reaction has been measured in the neutron energy range of 6.0 to 17.0 MeV. The data presented in Fig. 3-5 and tabulated in Table 3-4 represent the weighted average of two sets of data, one over the range $E_n = 6.0$ to 13.0 MeV [Wend78], and a later set spanning $E_n = 10.0$ to 17.0 MeV. The two sets of cross section data are absolute measurements, and contain no relative normalization. The agreement of the two sets of data over the region of overlap is excellent. In fact, the structure seen at $E_n \simeq 13.0$ MeV on the high energy side of the main peak was apparent in each case. Each data point required approximately 2.5 hours to measure. The earlier data were obtained with a gas cell pressure of 28 psia, where the energy spread in the neutrons produced in the gas cell ranges from 188 keV at $E_n = 7$ MeV to 80 keV at $E_n = 13$ MeV. This allowed the energy resolution necessary for data taken in 200 keV steps. The later data were taken at 42.7 psia, in 500 keV steps, with a typical energy spread of 127 keV at 12 MeV. The error bars in the figure are only statistical errors; the total uncertainty in the measurements due to the systematic errors is estimated to be about 15%, and includes the uncertainties in data stripping, efficiency measurements, finite geometry corrections, statistical errors, and the measurement of the cross section of the source reaction. The absolute cross section in this energy range has also

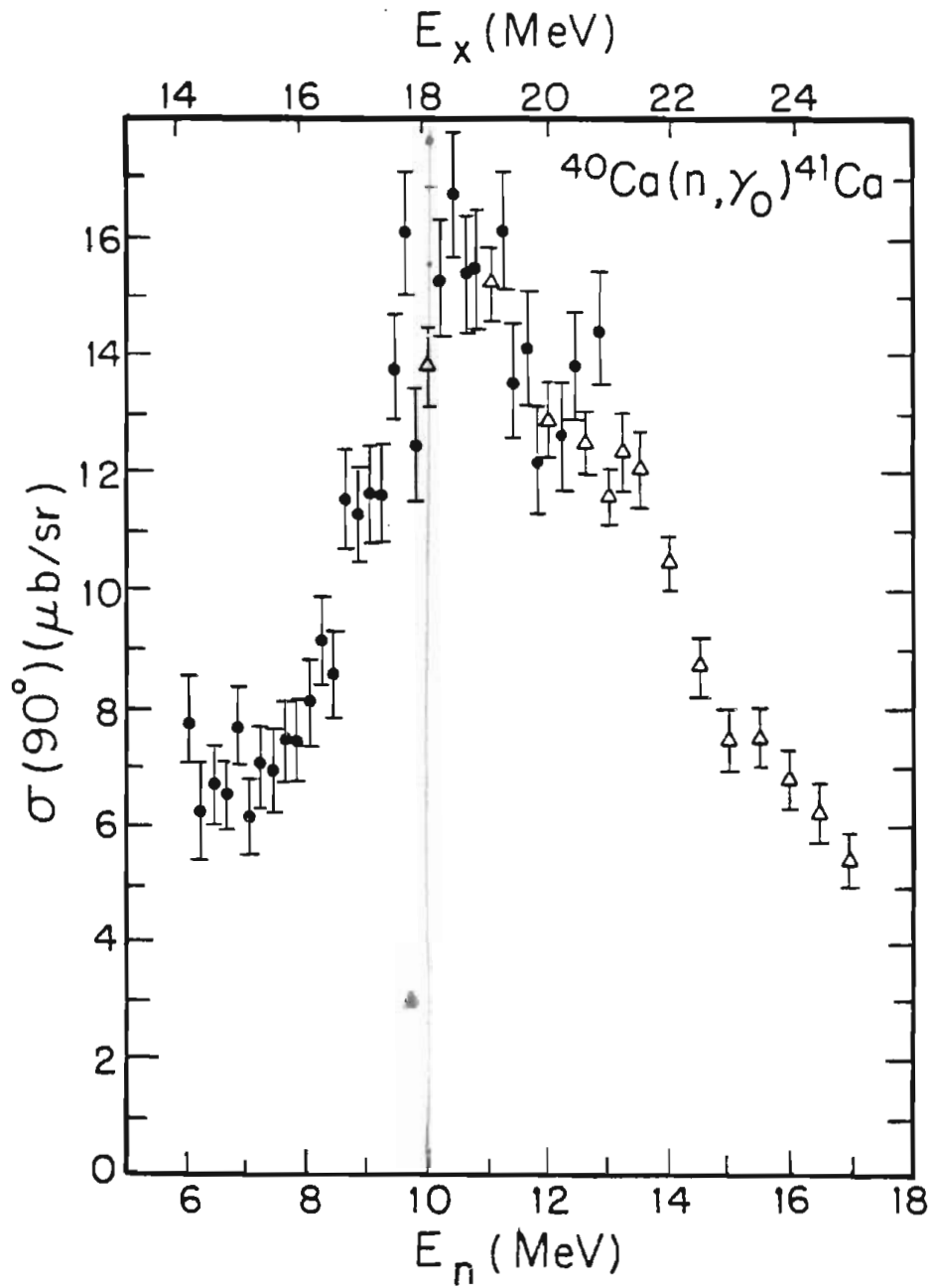


Figure 3-5. Absolute 90° cross section measurements for the reaction $^{40}\text{Ca}(n, \gamma)^{41}\text{Ca}$. The data have been corrected for finite geometry effects.

Table 3-4

Values of $\sigma(90^\circ)$ as a
Function of Neutron Energy

E_n	$\sigma(\mu\text{b}/\text{sr})$
6.0	7.75 \pm 0.70
6.2	6.22 \pm 0.84
6.4	6.66 \pm 0.67
6.6	6.51 \pm 0.60
6.8	7.61 \pm 0.64
7.0	6.15 \pm 0.66
7.2	7.01 \pm 0.69
7.4	6.89 \pm 0.68
7.6	7.42 \pm 0.69
7.8	7.41 \pm 0.68
8.0	8.08 \pm 0.70
8.2	9.15 \pm 0.74
8.4	8.56 \pm 0.72
8.6	11.50 \pm 0.83
8.8	11.25 \pm 0.81
9.0	11.59 \pm 0.82
9.2	11.58 \pm 0.82
9.4	13.76 \pm 0.89
9.6	16.06 \pm 1.05
9.8	12.44 \pm 0.92
10.0	13.74 \pm 0.65
10.2	15.27 \pm 1.01
10.4	16.72 \pm 1.05
10.6	15.38 \pm 1.01
10.8	15.42 \pm 1.01
11.0	15.14 \pm 0.68
11.2	16.10 \pm 1.02
11.4	13.52 \pm 0.93
11.6	14.17 \pm 0.96
11.8	12.15 \pm 0.89
12.0	12.83 \pm 0.62
12.2	12.58 \pm 0.89
12.4	13.77 \pm 0.93
12.6	12.43 \pm 0.52
12.8	14.20 \pm 0.95
13.0	11.56 \pm 0.45
13.25	12.28 \pm 0.68
13.5	12.01 \pm 0.68
14.0	10.42 \pm 0.44
14.5	8.67 \pm 0.56
15.0	7.39 \pm 0.52
15.5	7.45 \pm 0.52
16.0	6.72 \pm 0.50
16.5	6.13 \pm 0.49
17.0	5.37 \pm 0.46

been measured by Bergqvist et al [Berg74], and agrees reasonably well with the data presented in Fig. 3-5.

The yield curve exhibits a characteristic giant resonance shape, peaking at about $E_n = 10.5$ MeV, ($E_x = 18.6$ MeV), with a FWHM of 4.0 MeV. The shape and the position of the data agree well with other measurements in this mass region, if one considers isospin selection rules [Nils80,Dien73a,Braj74].

The total cross section can be derived from the integration of angular distributions. Since $\sigma_{tot} = 4\pi A_0$ (see § 5-A), the ratio of $\sigma(90^\circ)/A_0$ is needed in this case. Angular distributions have been measured at eight neutron energies, $E_n = 8.0$ to 15.0 MeV. The resulting values of $\sigma(90^\circ)/A_0$ are presented in Table 3-5 and Fig. 3-6. At energies where there were no angular distribution data, $\sigma(90^\circ)/A_0$ was determined from a smooth curve normalized to the data at 10 MeV, calculated on the basis of the direct-semidirect model (see § 4-A). This curve appears in Fig. 3-6. The total cross section results calculated from the $\sigma(90^\circ)$ measurements and the calculated values of $\sigma(90^\circ)/A_0$ are shown in Fig. 3-7.

In order to compare the (n,γ) total cross section data to photonuclear cross section measurements and to estimate the fraction of the electric dipole sum rule that is exhausted in the (γ,n_0) channel, it is necessary to convert the data into its time-reversed cross section. This can be done through the principle of detail balance, outlined by Hayward [Hayw70]. The expression used for this conversion is:

Table 3-5

Values of $\sigma(90^\circ)/A_0$
Derived from Angular Distribution Data

E_n	$\sigma(90^\circ)/A_0$
8.0	0.796 \pm 0.023
9.0	0.896 \pm 0.019
10.0	0.929 \pm 0.020
11.0	0.964 \pm 0.035
12.0	1.095 \pm 0.040
13.0	1.049 \pm 0.038
14.0	1.098 \pm 0.023
15.0	1.261 \pm 0.046

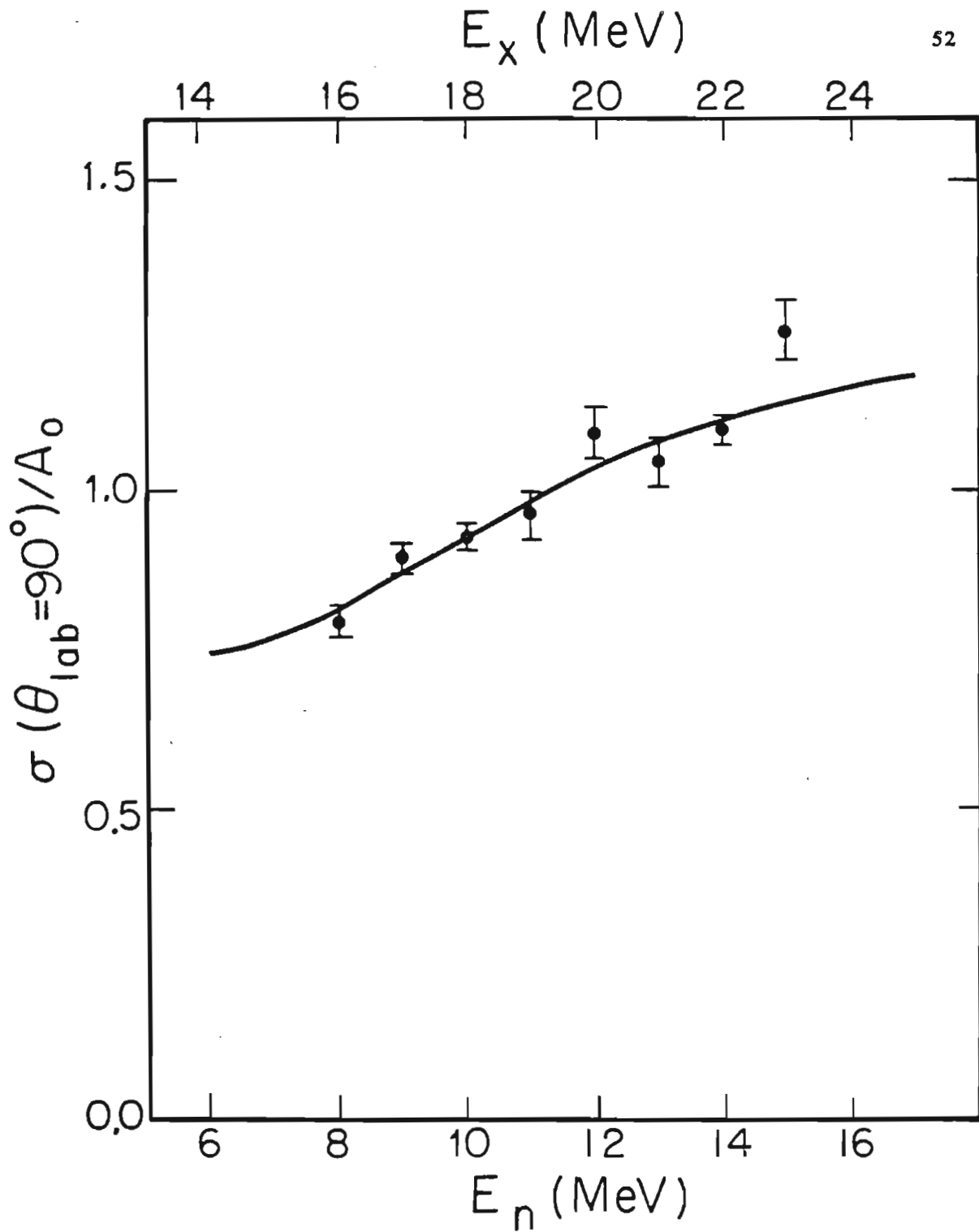


Figure 3-6. $\sigma(90^\circ)/A_0$ vs E_n . The dots are the values extracted from the data, and the solid lines are the results of a DSD model calculation normalized to the data at $E_n = 10$ MeV.

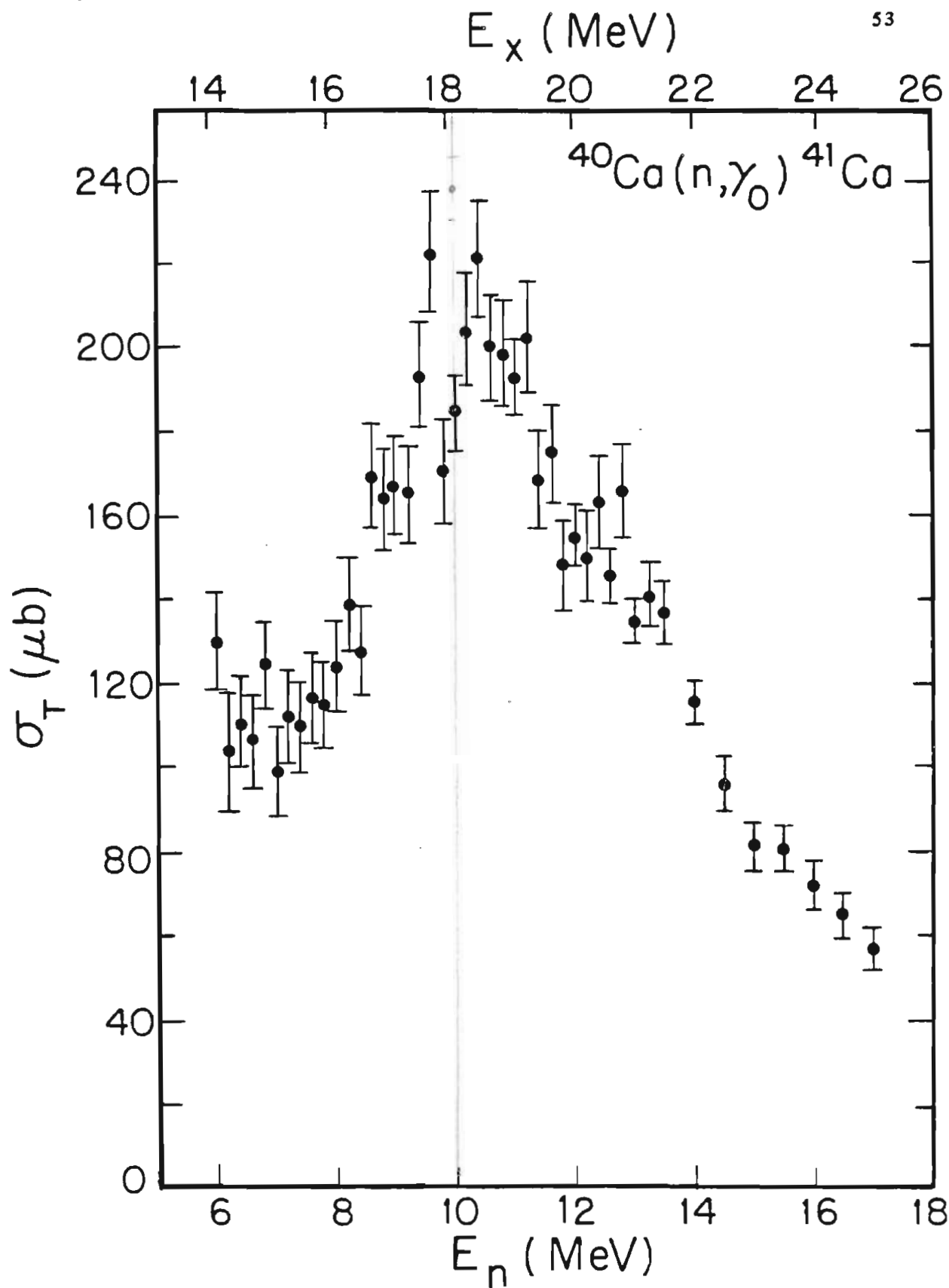


Figure 3-7. Total cross section calculations as a function of E_n .

$$\sigma(\gamma, n) = \frac{2I_{A-1} + 1}{2I_A + 1} \frac{A - 1}{A} \frac{E_x - Q}{E_x^2} 2Mc^2 \sigma(n, \gamma) \quad 3-2$$

where the parameters on the right of the equation refer to those of the (n, γ) reaction. For example, I_{A-1} and I_A imply the spin of the target and residual nuclei, respectively, in the (n, γ) reaction, while E_x is the energy of the γ -ray emitted in the decay process, M is the rest mass of the neutron, and Q is the Q -value of the capture reaction. The results of applying this technique to the present data are shown in Fig. 3-8.

B. Analyzing Power Measurements

The general expression for the analyzing power as a function of angle is given by

$$A(\theta) = \frac{1}{P} * \frac{NU - ND}{NU + ND} \quad 3-3$$

where NU and ND are the number of counts in the spin up and spin down states, respectively, defined according to the Madison Convention [Bars70]. The polarization of the beam is given by P . For a measurement made with two detectors at the same angle θ on opposite sides of the beam line, Eq. 3-3 can be written

$$A(\theta) = \frac{1}{P} * \frac{r - 1}{r + 1} \quad 3-4$$

where

$$r = \sqrt{\frac{LU * RD}{LD * RU}} \quad 3-5$$

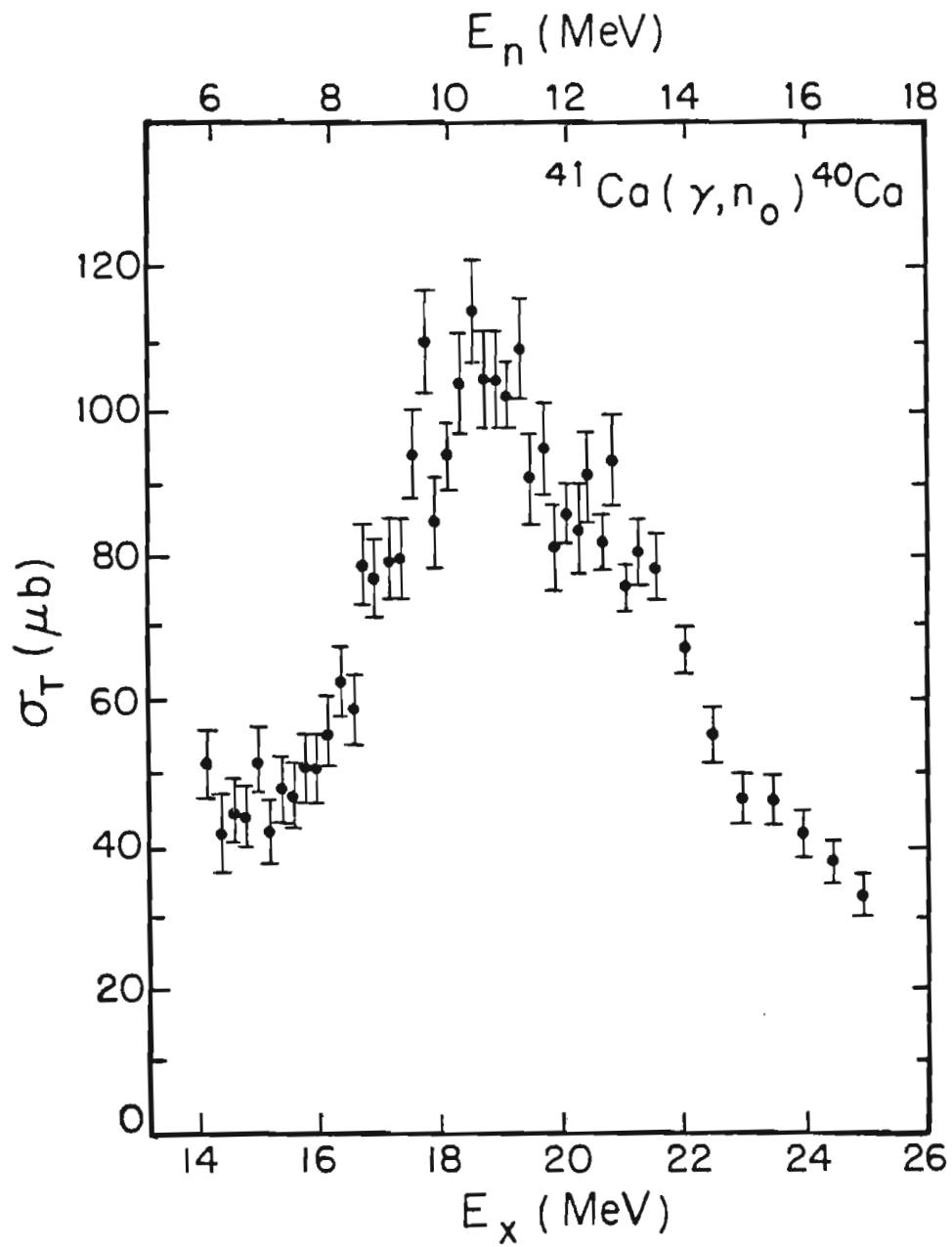


Figure 3-8. The total cross section for the $^{41}\text{Ca}(\gamma, n_0)^{40}\text{Ca}$ reaction calculated by the principle of detail balance.

and

LU (LD) = net counts in the left detector in the spin up (down)
state
RU (RD) = net counts in the right detector in the spin up (down)
state

In both Eqs. 3-3 and 3-4, the polarization P has been assumed to be equal for the spin up and the spin down states. In fact, this is not necessarily true. The equations for the analyzing power become much more complicated when this is taken into account. A more complete explanation of the derivations involved along with the error analysis can be found in Appendix A and will not be presented here.

The analyzing power at 90° has been measured over the energy range $E_n = 7.0$ MeV to 11.5 MeV. The data presented in Fig. 3-9 and Table 3-6 are the weighted averages of data taken at several different times. These data have not been corrected for finite geometry effects, since it was found that these corrections did not substantially change the final results. More will be said about this in the section on the angular distribution data (see § 3-C). The error bars represent statistical errors. The relevant experimental parameters of each run are listed in Table 3-7, including gas cell pressure and the neutron energy range of the particular experiment. In addition, the energies at which $A(90^\circ)$ was measured as part of an angular distribution are indicated. The data of November 1978 and October 1980 were taken with only one detector. The use of two detectors in the later experiments of January and April 1982 facilitated data-taking by increasing the count rate, thereby improving the statistical error for a given amount of run time. All

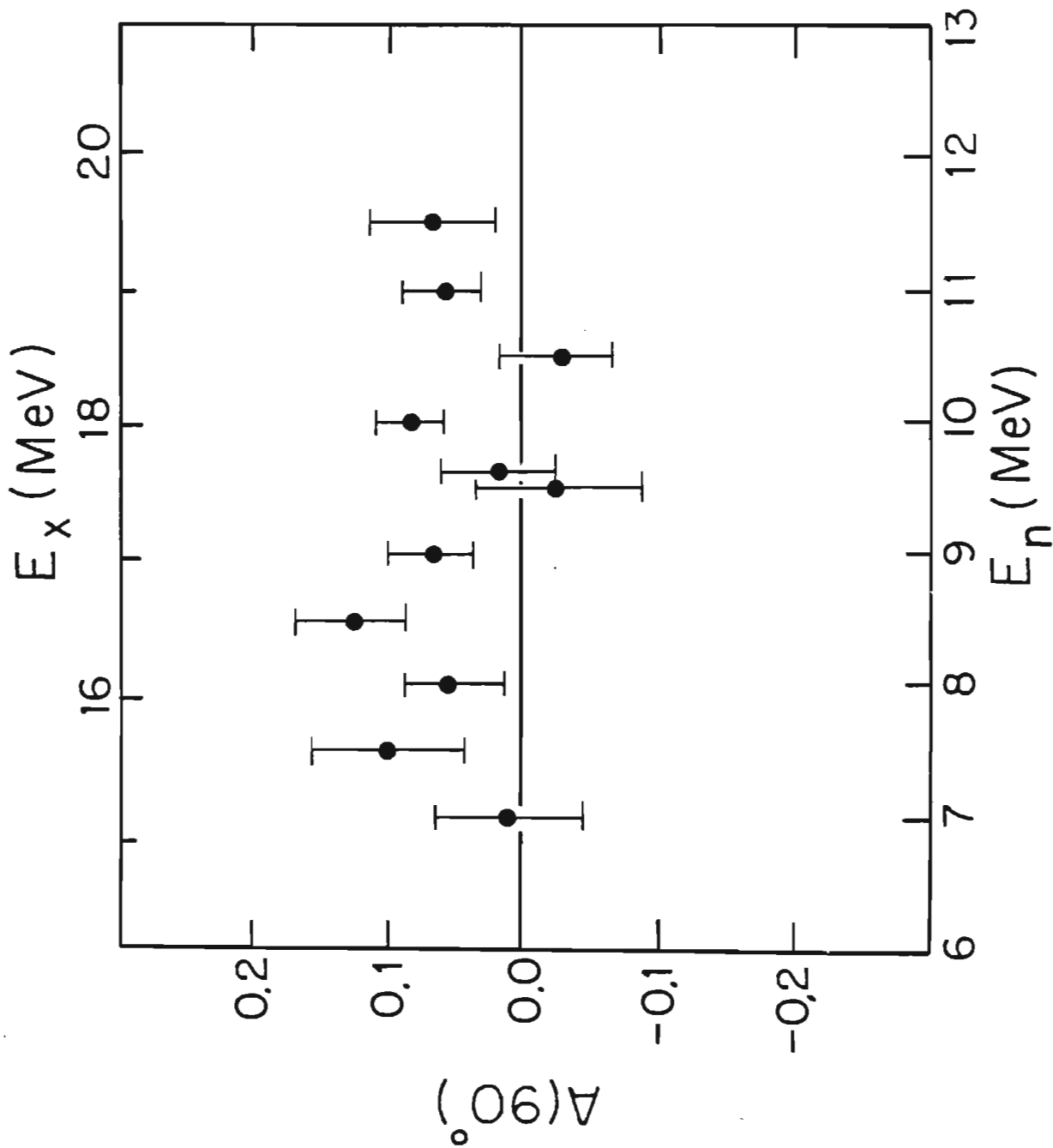


Figure 3-9. The 90° analyzing power measurements as a function of neutron energy.

Table 3-6

90° Analyzing Power Measurements
as a Function of Neutron Energy

E_n	$A(90^\circ)$
7.0	0.007 ± 0.058
7.5	0.097 ± 0.058
8.0	0.049 ± 0.037
8.5	0.124 ± 0.042
9.0	0.065 ± 0.032
9.5	-0.028 ± 0.064
9.6	0.015 ± 0.043
10.0	0.079 ± 0.026
10.5	-0.026 ± 0.043
11.0	0.059 ± 0.028
11.5	0.066 ± 0.047

Table 3-7 Experimental Parameters of 90° Analyzing Power Measurements

Date	Neutron Energies (MeV)	Neutron Energies where A(90°) from Ang. Distrib.	Gas Cell Press (psia)	Dist to Front Face of Detector (inches)
Nov. 1978	8.0, 9.0 10.0, 11.0	all	~ 42.5	31.75
Oct. 1980	7.0, 7.5, 8.0, 8.5, 9.0, 9.5, 10.0, 11.0	none	90.0	31.75
Jan. 1982	8.0	8.0	42.7	31.75
Apr. 1982	8.0, 8.5, 9.0, 9.6, 10.0, 10.5, 11.0, 11.5	9.0	42.8	31.75

data were taken in the high rejection mode, with the spin states alternated several times during each run.

C. Angular Distribution Measurements

1. Cross Section

Measurements of angular distributions of cross section have been made at neutron energies of $E_n = 8.0, 9.0, 10.0, 11.0, 12.0, 13.0, 14.0$ and 15.0 MeV. These angular distributions can be expanded as

$$\sigma(\theta) = \sum_{i=0}^{NMAX} A_i P_i(\cos \theta) \quad 3-6$$

where the $P_i(\cos \theta)$ are the Legendre polynomials. When the cross section is integrated over angle, $\sigma_{tot} = 4\pi A_0$. It is usually more convenient to renormalize the expression as

$$\sigma(\theta)/A_0 = \sum_{i=0}^{NMAX} a_i P_i(\cos \theta) \quad 3-7$$

where $a_i = A_i/A_0$, and $a_0 = 1$.

It will be seen later (§ 6-A and 6-B) that the coefficients of the Legendre expansions can be expressed in terms of the possible transition matrix elements of the reaction studied. The maximum term in the series is taken to be $NMAX \leq 2L$ where L is the highest multipolarity of the transition included in the analysis. We have followed the suggestion of Langsdorf [Lang59] that if the a_i coefficient is to be determined with reasonable accuracy, the measurement of $\sigma(\theta)$ should be extended to the zeroes of $P_{i+1}(\cos \theta)$.

At five energies ($E_n = 8.0, 10.0, 11.0, 14.0,$ and 15.0 MeV), the accuracy of the data and the measured angular range allowed a statistically significant fit only for $NMAX = 3$. At $E_n = 9.0, 12.0,$ and 13.0 MeV, $NMAX = 4$.

A preliminary investigation of this experiment along these lines was done by Weller et al [Well78]. The current data are presented in Fig. 3-10, corrected for the effects of finite geometry as described below. Some of this data has already been reported [Wend78,Jens79]. The curves in the figure are the fits to the sum of Legendre polynomials using a least-squares criterion (Eq. 3-7). The resulting a_i coefficients derived from these fits are shown in Fig. 3-11 and are tabulated in Tables 3-8 and 3-9 for both third and fourth order expansions, respectively.

The data presented in the figure were taken at several different times, with both polarized and unpolarized beam. Table 3-10 lists the experimental parameters of each experiment along with the energies at which angular distributions were measured, and indicates whether the data were taken with polarized or with unpolarized beam. All data was taken in the high rejection mode. In all cases where angular distribution data at a particular energy were measured on more than one occasion, the individual datasets were first analyzed separately and a normalization factor was determined for each set from the separate values of A_0 . These factors were then used to combine all of the data for a single final analysis.

The usual procedure of using two detectors depended on whether

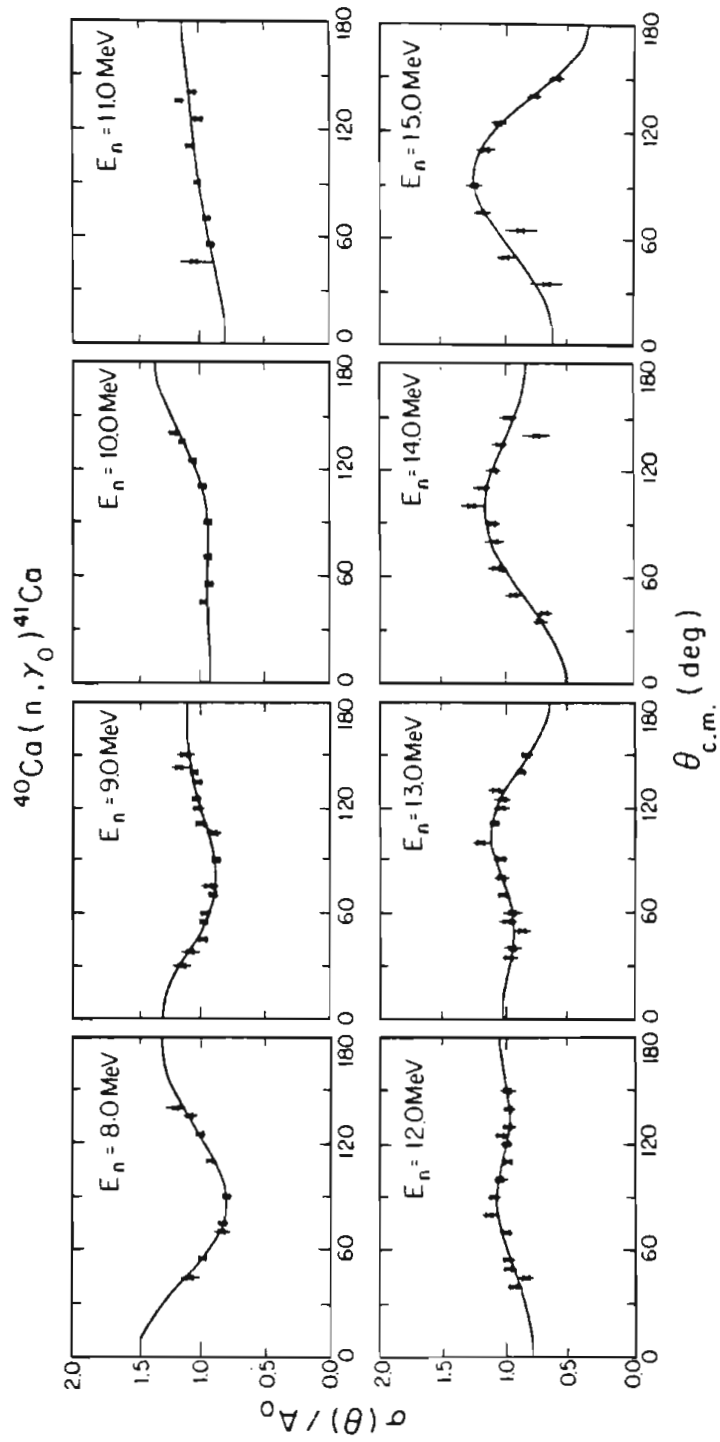


Figure 3-10. Angular distributions of cross section. The data have been corrected for finite geometry effects. 62

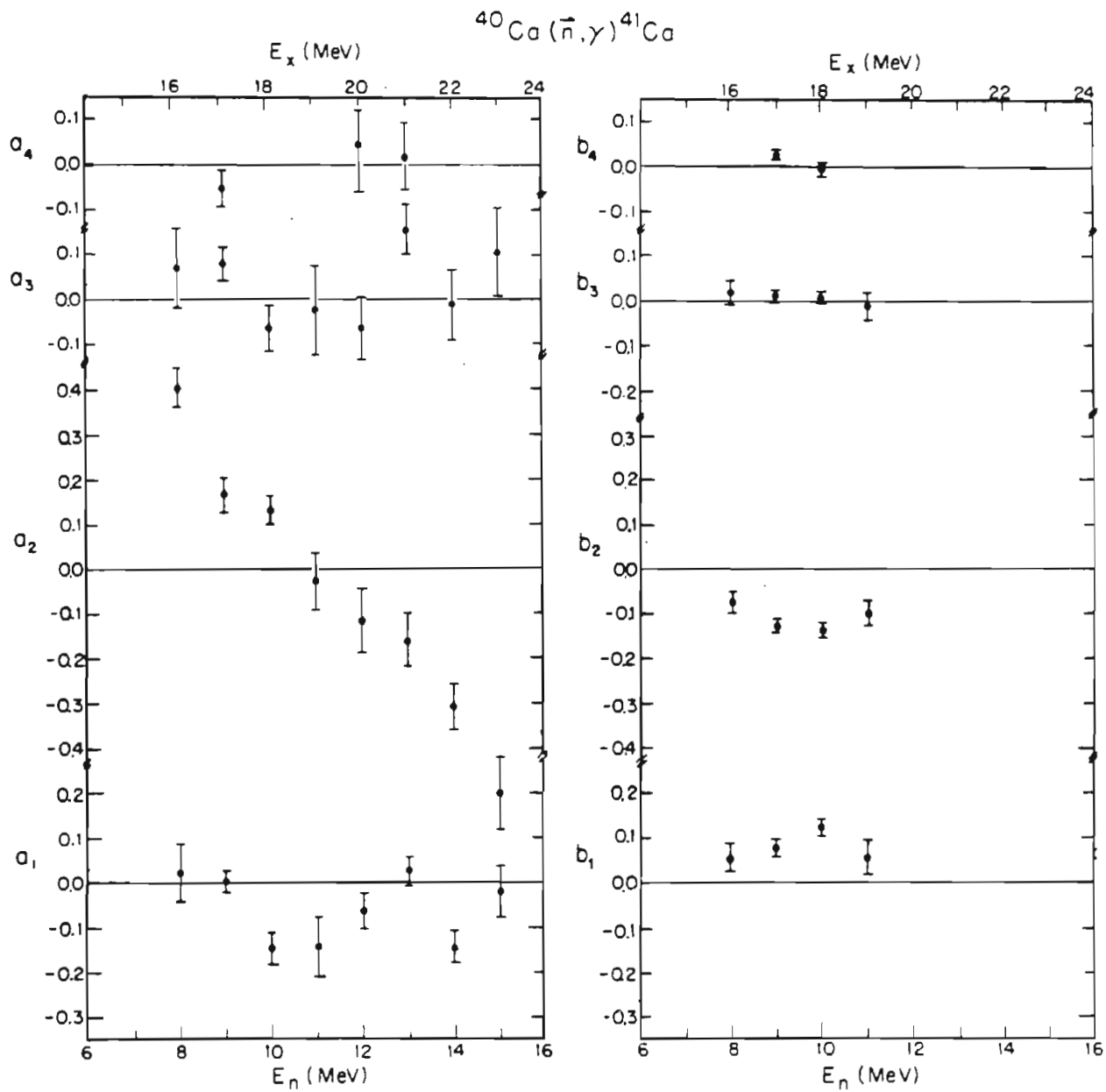


Figure 3-11. The a_i and b_i coefficients extracted from the angular distributions of cross section.

Table 3-8 Legendre Coefficients Extracted from Fits of Angular Distributions of Cross Section to Third Order

E_n	a_1	a_2	a_3
8.0	0.021 ± 0.065	0.403 ± 0.043	0.068 ± 0.089
9.0	0.010 ± 0.023	0.205 ± 0.025	0.083 ± 0.036
10.0	-0.146 ± 0.034	0.131 ± 0.032	-0.065 ± 0.051
11.0	-0.142 ± 0.066	-0.028 ± 0.065	-0.026 ± 0.099
12.0	-0.077 ± 0.032	-0.147 ± 0.044	-0.090 ± 0.057
13.0	0.023 ± 0.032	-0.168 ± 0.042	0.152 ± 0.054
14.0	-0.145 ± 0.037	-0.307 ± 0.052	-0.013 ± 0.078
15.0	0.021 ± 0.058	-0.499 ± 0.082	0.105 ± 0.099

Table 3-9 Legendre Coefficients Extracted from Fits of Angular Distributions of Cross Section to Fourth Order

E_n	a_1	a_2	a_3	a_4
8.0	0.018 ± 0.073	0.393 ± 0.142	0.065 ± 0.098	-0.009 ± 0.120
9.0	0.003 ± 0.023	0.164 ± 0.039	0.077 ± 0.036	-0.054 ± 0.040
10.0	-0.132 ± 0.035	0.212 ± 0.076	-0.057 ± 0.051	0.085 ± 0.073
11.0	-0.033 ± 0.090	0.219 ± 0.162	0.096 ± 0.118	0.205 ± 0.126
12.0	-0.062 ± 0.041	-0.115 ± 0.071	-0.066 ± 0.070	0.044 ± 0.076
13.0	0.025 ± 0.033	-0.159 ± 0.058	0.156 ± 0.056	0.016 ± 0.073
14.0	-0.147 ± 0.038	-0.321 ± 0.073	-0.020 ± 0.082	-0.028 ± 0.101
15.0	0.006 ± 0.066	-0.542 ± 0.118	0.074 ± 0.116	-0.068 ± 0.132

Table 3-10 Experimental Parameters of Angular Distribution Measurements

Date	Neutron Energies (MeV)	Type of Beam	Gas Cell Pressure (psia)	Dist to Front Face of Det (inches)
Jan. 1978	8.0,9.0, 10.0,11.0	unpol	29.7	31.75
Feb. 1978	8.0,9.0, 10.0,11.0, 12.0,13.0	unpol	≈ 28.7	31.75
Nov. 1978	8.0,9.0, 10.0,11.0	pol	≈ 42.7	31.75
Apr. 1981	9.0,12.0, 13.0	unpol	42.7	48.84
Sept. 1981	14.0,15.0	unpol	42.7	48.84
Jan. 1982	8.0	pol	42.7	31.75
Apr. 1982	9.0	pol	42.7	31.75

the experiment was performed with polarized or unpolarized beam. If polarized beam was used, the two detectors were positioned simultaneously at the same angle, so that the analyzing power could be measured with both detectors at the same time (see the following section). However, if the experiment was done with unpolarized beam, alternating angles were measured with different detectors, with at least one angle measured with both detectors. This was done to check the relative normalization between the detectors. The expressions for the cross section in terms of the number of counts in the detectors for both one- and two- detector data are derived in App. A.

The data in Fig. 3-10 have been corrected for finite geometry using the Monte Carlo code FIXER. To generate the correction factors, the program starts with the experimentally measured cross section, σ_{meas} as a first guess, σ_{guess}^i , to the true cross section. Based on this guess, the code predicts an observed cross section, σ_{pred}^i , which includes all the finite geometry effects. A new guess at the true cross section is made according to

$$\sigma_{\text{guess}}^{i+1} = \frac{\sigma_{\text{meas}}}{\sigma_{\text{pred}}^i} \sigma_{\text{guess}}^i \quad 3-8$$

where the correction is made at each angle. The iteration continues until $(\sigma_{\text{meas}} - \sigma_{\text{pred}}^{i+1})$ is small. The true cross section is then given by $\sigma_{\text{guess}}^{i+1}$. In practice, only one iteration of this procedure is necessary.

In the present work, the observed angular distributions necessary for the first guess were supplied to the code in the form of the a_i

coefficients at each energy. These coefficients were determined by fitting the angular distribution data with the data reduction codes DATAAMP (written by C. Cameron [Came77]) or SCRAP (see Appendix A or [Murp83]). These codes have the option of correcting the data for the finite size of the crystal. However, to generate the input to FIXER, point geometry was assumed in the data reduction. The resulting a_i coefficients were used in FIXER to produce the first-guess cross sections necessary to begin the iteration procedure. The data were multiplied by the correction factors produced by this process and a new set of a_i coefficients were generated on the basis of the corrected data, again assuming point geometry for the input to the data reduction code. The effect of this procedure was to change the a_i coefficients by only a few percent.

2. Analyzing Power

Angular distributions of analyzing power have been measured at neutron energies of $E_n = 8.0, 9.0, 10.0,$ and 11.0 MeV. The data at $E_n = 10.0$ MeV have been reported previously [Jens79]. The angular distributions of $\sigma(\theta)A(\theta)/A_0$ are shown in Fig. 3-12, with the expression for the analyzing power as a function of angle, $A(\theta)$ given by Eq. 3-3. The product $\sigma(\theta)A(\theta)/A_0$ can be expanded as

$$\frac{\sigma(\theta)A(\theta)}{A_0} = \sum_{i=0}^{NMAX} b_i P_i^1(\cos \theta) \quad 3-9$$

where the $P_i^1(\cos \theta)$ are the associated Legendre polynomials. Like the a_i coefficients, the b_i coefficients can be written in terms of the

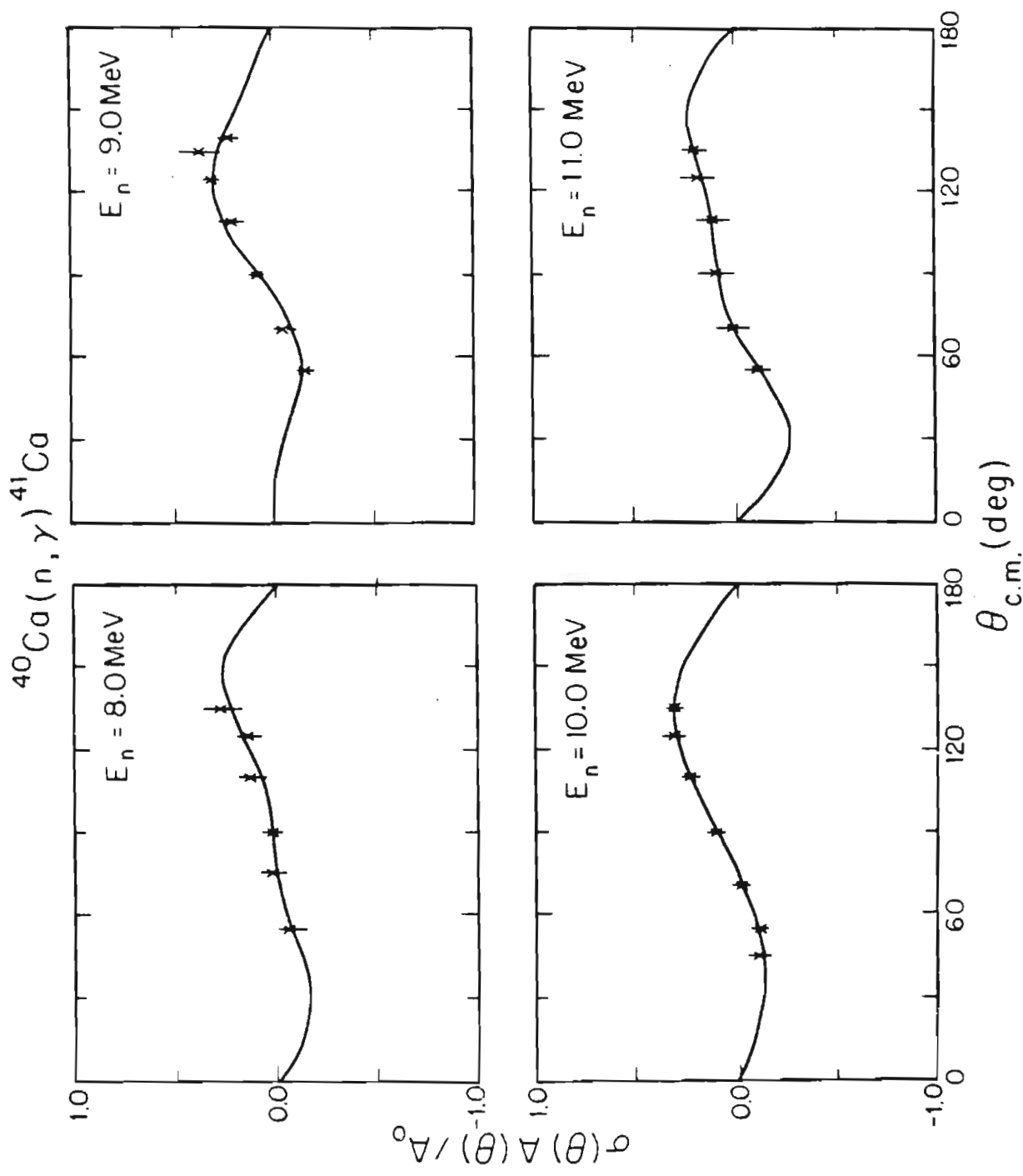


Figure 3-12. Angular distributions of analyzing power. Finite geometry corrections are described in the text. 69

transition matrix elements of the reaction. The exact expressions will be presented in a later section (see § 6-A and 6-B). The maximum nonzero term in the expansion is again $N_{MAX} \leq 2L$. Whether it is experimentally possible to measure the contribution from the higher order terms depends on the angles measured. Since $b_0 = 0$, and the zeroes of $P_k^1(\cos\theta)$ occur closer to 90° than those of $P_k(\cos\theta)$, the b_4 coefficient can be measured if the angular range of the experiment is from about 40° to about 140° . The b_i coefficients extracted from the data of Fig. 3-12 are shown in Fig. 3-11. The values of the coefficients are listed for both third and fourth order fits in Tables 3-11 and 3-12. The experimental parameters of all polarized runs are listed in Table 3-10, since both cross section and analyzing power are measured with polarized beam.

In order to perform finite geometry corrections on the analyzing power data, the following method was used. The cross section and analyzing power at a given energy were decomposed into the spin up cross section σ^+ , and the spin down cross section σ^- , and these contributions were fed individually into the fitting code DATAAMP. The resulting sets of a_i coefficients were fed separately into FIXER, and the finite geometry correction factors for each spin state were used to correct the original data. Finally, this corrected data was processed with DATAAMP. The result was that, in the energy range studied, the b_i coefficients changed by only a small fraction of their associated errors. For this reason, the analyzing power measurements presented in this thesis are uncorrected for any finite geometry effects, and any correction factors enter into the angular

Table 3-11 Associated Legendre Coefficients Extracted from Fits of Angular Distributions of $\sigma(\theta)A(\theta)/A_0$ to Third Order

E_n	b_1	b_2	b_3
8.0	0.056 ± 0.031	-0.079 ± 0.026	0.020 ± 0.025
9.0	0.078 ± 0.019	-0.126 ± 0.014	0.023 ± 0.011
10.0	0.127 ± 0.017	-0.144 ± 0.013	0.008 ± 0.014
11.0	0.056 ± 0.039	-0.104 ± 0.028	-0.008 ± 0.032

Table 3-12 Associated Legendre Coefficients Extracted from Fits of Angular Distributions of $\sigma(\theta)A(\theta)/A_0$ to Fourth Order

E_n	b_1	b_2	b_3	b_4
8.0	0.050 ± 0.032	-0.103 ± 0.039	0.015 ± 0.026	-0.032 ± 0.038
9.0	0.076 ± 0.019	-0.134 ± 0.014	0.010 ± 0.012	0.024 ± 0.010
10.0	0.122 ± 0.018	-0.143 ± 0.015	0.008 ± 0.013	-0.005 ± 0.015
11.0	0.044 ± 0.038	-0.117 ± 0.034	-0.024 ± 0.035	-0.035 ± 0.039

distributions of Fig. 3-12 only through the correction to $\sigma(\theta)$.

4. Theory

A. Classification of Multipole Resonances

In photonuclear capture, it is useful to classify the giant multipole resonances according to the oscillations of the nucleus that they describe. In the transition from the excited intermediate state to the final state of the residual nucleus, the angular momentum L of the emitted photon determines the multipolarity of the transition. If $L=1$, the transition is a dipole transition. If $L=2$ or $L=3$, the decay is a quadrupole or octupole transition, respectively, and so on. If the parity changes by $(-1)^L$, an electric transition has occurred; while if the parity changes by $(-1)^{L+1}$, a magnetic transition has occurred. The notation is as follows: a transition of multipolarity L is labeled as an "EL" or "ML" transition, depending on if it is electric or magnetic. For example, E1 and M1 refer to electric and magnetic dipole transitions, respectively.

Fig. 4-1 shows a picture of some of the possible vibrational modes of a nucleus along with the associated spin and isospin selection rules. The isoscalar electric modes are oscillations of the nucleus as a whole while isovector electric modes correspond to oscillations of protons against neutrons without spin

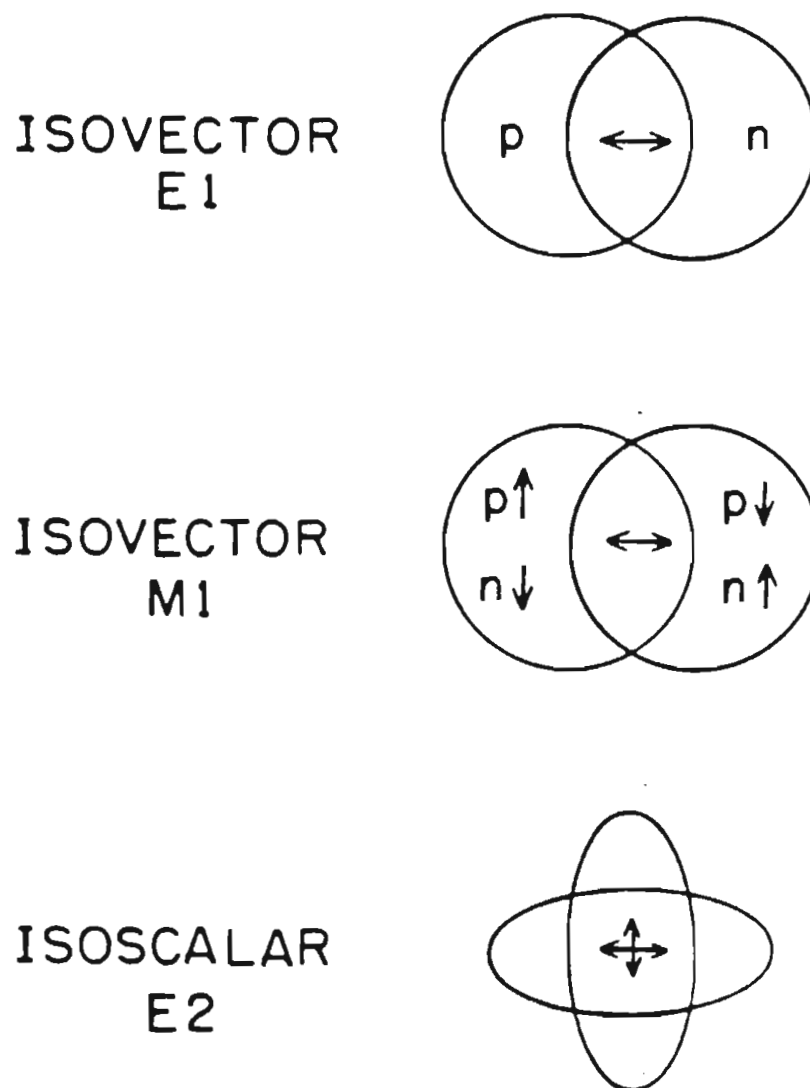


Figure 4-1. Some possible nuclear vibrational modes with the associated spin and isospin selection rules.

differentiation. On the other hand, the magnetic modes correspond to oscillations involving spin. For example, in the isovector modes, protons with spin up oscillate against neutrons with spin up, and so on.

B. Formalism

In the direct-semidirect model, the radial part of the transition matrix elements is given by

$$\langle u_b | d^L | \chi^{(+)} \rangle + \frac{\langle u_b | h^L(r) | \chi^{(+)} \rangle}{E - E_r + i\Gamma/2} \quad 4-1$$

where $\chi^{(+)}$ is the continuum wave function of the incoming nucleon calculated with the optical model, and u_b is the radial wave function of the captured nucleon in the final bound state [Well80]. The first term represents the direct part of the matrix element; the quantity d^L is the radial part of the single-particle electromagnetic operator for radiation of multipolarity L . In the long wavelength limit, $d^L = r^L$. The second term represents the semidirect or resonance part of the matrix element. In the denominator of this term, E_r and Γ represent the energy and width of the appropriate resonance, respectively, of the combined particle plus nucleus system. The operator $h^L(r)$ represents the radial part of the particle-nucleus vibrational coupling interaction. Several authors have suggested a form for this operator [Clem65, Brow64, Poto73]. The one used for the electric dipole calculations in this thesis is that of Potokar,

$$h^1(r) \propto \left[\frac{1}{4} V_1 f_a(r) - \frac{1}{4} W_1 4b \frac{\partial f_b(r)}{\partial r} \right] \quad 4-2$$

where V_1 and W_1 are the real and imaginary parts of the optical model symmetry potential, respectively; $f_a(r)$ and $f_b(r)$ are Woods-Saxon form factors, and b is the diffuseness parameter of the imaginary term.

The photoabsorption cross section is dominated by the contribution of the giant dipole resonance (GDR), as can be determined by examination of angular distribution data. The GDR is located at $80 A^{-1/3}$ MeV in heavy nuclei, and at about 20 MeV in lighter nuclei, with a width from 3 to 10 MeV [Hayw70]. It exhausts most of the classical electric dipole sum rule

$$\int \sigma_\gamma(E1) dE_\gamma = \frac{60 NZ}{A} \text{ mb-MeV} \quad 4-3$$

However, the contributions from higher order multipoles can also be of interest, particularly those from electric quadrupole radiation. The giant quadrupole resonance (GQR) is located at about $63 A^{-1/3}$ MeV for nuclei with $A > 36$ [Bert76]. The energy weighted sum rule for the isoscalar part of this resonance is given by [Gel153]

$$\int \frac{\sigma_\gamma(E2)}{E_\gamma^2} dE_\gamma = \frac{\pi^2}{137} \frac{A}{11} \frac{\langle r^2 \rangle}{938} \text{ fm}^2 \text{ MeV}^{-1} \quad 4-4$$

where $\langle r^2 \rangle$ is the value of the mean square nuclear radius.

A direct extension of the model can be made to include direct

and semidirect E2 terms in the calculations [Snov76,Satc72,Long72]. The form factor in the semidirect term of Eq. T-1 for an isoscalar E2 resonance based on the Goldhaber-Teller model [Uber71] has a surface-peaked shape proportional to $-r dU_0(r)/(dr)$, where $U_0(r)$ is the real central potential. For an isovector E2 resonance, the form factor is proportional to $r^2 V_1(r)$, where $V_1(r)$ is the real part of the optical model symmetry potential [Snov76].

However, these E2 form factors have not been clearly established. The most extensive data for E2 cross section measurements have been obtained from (\vec{p}, γ) measurements [Well80]. But because of the large direct E2 contribution to the proton capture reaction, it has been difficult to unfold the collective E2 part of the cross section to test these form factors. As discussed in the introduction, part of the motivation of this study of neutron capture was to examine a case where the direct E2 strength was suppressed, for which the collective E2 strength could be more easily studied. As part of our program for testing the standard E2 form factors, we have also made calculations using an isoscalar E2 form factor which is proportional to $r^2 U_0(r)$ [Kita80]. This form factor is referred to below as the "volume form factor".

C. Transition Matrix Elements

It has been shown [Poto77] that the direct-semidirect cross section can be written as a product of the direct cross section and a resonance-like term

$$\sigma_{DSD} = \sigma_D \cdot |\text{FFACT}|^2 \quad 4-5$$

where

$$\text{FFACT} = 1 + \frac{1}{E - E_r + i\Gamma_r/2} \frac{\int u_b(r) h(r) \chi^{(+)}(r) dr}{\int u_b(r) r \chi^{(+)}(r) dr} \quad 4-6$$

and where $h(r)$ is the appropriate form factor.

In this discussion, the following notation should be understood. The reaction in question will be written as

$$a(x, \gamma)c \quad 4-7$$

where

- a = the total angular momentum of the target nucleus
- x = the spin of the incoming particle
- c = the total angular momentum of the residual nucleus

Other symbols that will be used are:

- l_a = the orbital angular momentum of the incident nucleon
- j_a = the total angular momentum of the incident nucleon
- l = the orbital angular momentum of the final single-particle bound state
- j = the total angular momentum of the final single-particle bound state
- b = the spin of the γ -ray emitting intermediate state
- L = the angular momentum of the emitted γ -ray
- p = the mode of decay ($p=1$ for electric and $p=0$ for magnetic)

decay)

$$\hat{q} = (2q + 1)^{1/2} \text{ for any quantity } q$$

Also, $I_c = C(T_a T_{az} \ 1/2 \ t_z, T_c T_{cz})$ is defined as the Clebsch-Gordan coefficient connecting the isospins of the initial and final states, where

$T_c \ (T_a)$ = the isospin of the residual (target) nucleus

$T_{cz} \ (T_{az})$ = the z-projection of the appropriate isospin

t_z = the z-projection of the isospin of the incident nucleon

For a target with spin zero, the total angular momentum c of the residual nucleus is just the total angular momentum of the final single particle state occupied by the captured nucleon. In this situation, the radial part of the transition matrix element for direct capture can be written as

$$T_G = i^{(1_a - 1 - L)} C(j \ \frac{1}{2} \ L \ 0, \ j_a \ \frac{1}{2}) \quad 4-8$$

$$\cdot e_L \left[\frac{CNORM}{2 j_a + 1} \right]^{1/2} (2x+1)^{1/2} \langle u_b | r^L | \chi^{(+)} \rangle$$

where

$$CNORM = 4\pi \frac{197.3289}{137.036} \frac{k_f}{E_a k_a} \frac{2j+1}{2x+1} B_L^2 \quad 4-9$$

and

$$B_L^2 = \frac{L+1}{(2L+1)L} \frac{k_f^{2L}}{[(2L-1)!!]^2} \quad 4-10$$

(see [Well80] or [Mang81] for more discussion). The cross section is

then given by

$$\sigma_T = 4\pi A_0 = I_c^2 S_j \sum \left[\frac{\hat{j}}{2a} \right]^2 |T_G|^2 \quad 4-11$$

where c is the true spin of the final state, and S_j is the spectroscopic factor describing the final single-particle state, u_b . Note that we are using the normalization condition

$$\sum \left[\frac{\hat{j}}{2a} \right]^2 |T_G|^2 = 1 \quad 4-12$$

The a_k and b_k can be calculated from

$$a_k = \left[\frac{\hat{k}}{2a} \right]^2 \frac{\bar{A}_k}{A_0} \quad 4-13$$

$$b_k = \left[\frac{\hat{k}}{2a} \right]^2 \frac{\bar{B}_k}{A_0} \quad 4-14$$

In the j - j coupling scheme, where $l_{a+s}=j_a$ and $j_{a+a}=b$, the factors \bar{A}_k and \bar{B}_k can be calculated according to the spin-zero target expressions ($a = 0$, $j_a = b$)

$$A_0 = \left[\frac{\hat{k}}{2a} \right]^2 \sum \left[\frac{\hat{j}}{2a} \right]^2 |T_G|^2 \quad 4-15$$

and

$$\begin{aligned}
\bar{A}_k = & \sum -1^{a-c+1-x+k+j-j'} \hat{j}_j \hat{j}_j, \hat{1}_1 \hat{1}_1, \hat{L}_L \hat{L}_L, \hat{b}_b \hat{b}_b, \hat{2}_x \hat{2}_x^{-2} \\
& \cdot \{ \} \cdot C(1 \ 0 \ 1' \ 0, \ k \ 0) \cdot W(1 \ j \ 1' \ j', \ x \ k) \\
& \cdot C(L \ 1 \ L' \ -1, \ k \ 0) \cdot W(j \ b \ j' \ b', \ a \ k) \\
& \cdot W(L \ b \ L' \ b', \ c \ k) \cdot \text{Re}(T_G T_G'^*)
\end{aligned} \tag{4-16}$$

and

$$\begin{aligned}
\bar{B}_k = & \frac{3\sqrt{x} \hat{x} \hat{k}}{[(x+1)k(k+1)]^{1/2}} \\
& \cdot \sum -1^{a-c+1+1'-j-j'} \hat{j}_j \hat{j}_j, \hat{1}_1 \hat{1}_1, \hat{L}_L \hat{L}_L, \hat{b}_b \hat{b}_b, \hat{2}_x \hat{2}_x^{-2} \\
& \cdot \{ \} \cdot C(1 \ 0 \ 1' \ 0, \ k \ 0) \cdot W(j \ b \ j' \ b', \ a \ k) \\
& \cdot C(L \ 1 \ L' \ -1, \ k \ 0) \cdot W(L \ b \ L' \ b', \ c \ k) \\
& \cdot X(1 \ x \ j, \ 1' \ x \ j', \ k \ 1 \ k) \cdot \text{Re}(iT_G T_G'^*)
\end{aligned} \tag{4-17}$$

where $\{ \} = \frac{1}{2} \cdot \{1 + (-1)^{L+p+L'+p'+k}\}$ and where the sums are over $pp'LL'bb'11'jj'$. Note that in the above equations, the subscripts have been dropped from 1, 1', j, and j' for convenience. Note also that Eqs. 4-8 through 4-10 have been written, for simplicity, assuming that the T_G have been calculated for pure direct capture. However, the calculations done in this thesis used the code HIKARI [Kitaz80], which calculated the T_G for both direct and semidirect capture by using FFACT (Eq. 4-6) in the particle-nucleus coupling term.

Since the ground state of ^{40}Ca is $T=0$, the neutron capture by

this nucleus can only excite $T=1/2$ states. This means that the only one value of the isospin Clebsch-Gordan coefficient involved is $I_c = C(0\ 0\ 1/2\ 1/2 | 1/2\ 1/2) = 1.0$. In addition, it has been shown that the spectroscopic factor of the ground state of ^{41}Ca is 1.0 [Bel65], which implies a pure $f_{7/2}$ ground state and eliminates the need for a summation over j in the expressions.

5. Analysis of Experimental Results

A. Absolute Cross Section Calculations

The absolute cross section measurements presented in Fig. 3-5 and Table 3-4 have been compared to direct-semidirect model calculations based on the considerations discussed in § 4. The current calculations use the Becchetti-Greenlees parameters [Becc69], which are presented in Table 5-1. The final single-particle state in Eq. 4-1 was obtained by adjusting the potential well-depth to produce the known binding energy $E_b = 8.346$ MeV of the ground state of ^{41}Ca . The final result of the well-depth search was a potential well of $V = 61.19$ MeV, compared to a typical well-depth of $V = 53.1$ at $E_n = 10$ MeV for the real part of the Becchetti-Greenlees optical model potential. The spectroscopic factor of the final state was 1.0 [Belo65]. Because the cross section in this energy range is predominantly from electric dipole transitions, only E1 terms in eq. 4-1 were considered. The addition of higher order terms will be discussed later. The values of the parameters used to calculate the final state are listed in Table 5-2.

The calculations presented here were first done assuming a pure direct capture process. The results are shown as the dotted line in Fig. 5-1. They not only fail to reproduce the order of magnitude of

Table 5-1

Becchetti-Greenlees Optical Model Parameters

$$V = 56.3 - 0.32 E - 24 (N - Z)/A$$

$$W = 0.22 E - 1.56$$

or zero, whichever is greater

$$W_D = 13 - 0.25 E - 12 (N - Z)/A$$

or zero, whichever is greater

$$V_{so} = 6.2$$

$$r_o = 1.17$$

$$a_o = 0.75$$

$$r_W = r_D = 1.26$$

$$r_{so} = 1.01$$

$$a_W = a_D = 0.58$$

$$a_{so} = 0.75$$

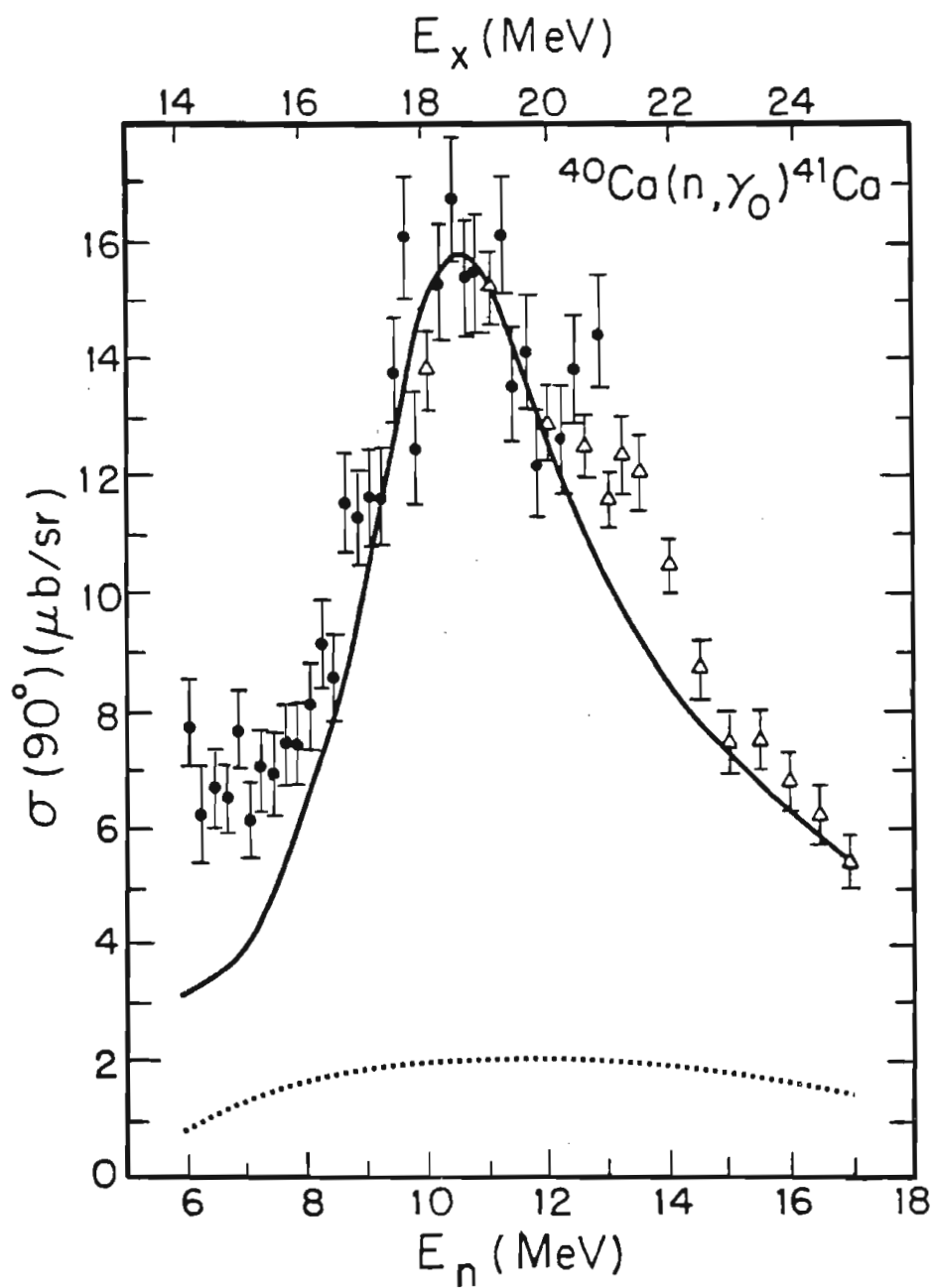


Figure 5-1. DSD model calculations of $\sigma(90^\circ)$, as described in the text.

the data, but also do not have the correct resonance-like shape. The results of adding a semi-direct term to the calculations are shown as the solid curve of Fig. 5-1. The calculations were performed with $E_x = 18.1$ MeV and $\Gamma = 4.0$ MeV (determined by fitting to the resonance). The strengths of the real and the imaginary terms in the Potokar coupling form factor were taken as $V_1 = 73.0$ MeV, $W_1 = 32.0$ MeV, respectively, consistent with values derived from optical model analysis of charge exchange reactions [Carl75]. The ratio of V_1/W_1 was adjusted to produce the best shape of the calculations, and the fraction of the classical sum rule, after correction for isospin [Leon75], was set at $\eta = 0.69$. The ground state correlation factor used was $\alpha = 0.45$, in agreement with values quoted by Leonardi [Leon72]. A summary of the parameters used in the coupling term is given in Table 5-3.

A significant deviation of the calculations from the data occurs at $E_\gamma = 21$ MeV. A similar structure has also been observed [Dien73] and predicted [Blom69] in the giant dipole resonance region of ^{40}Ca . Also, the calculations fail to predict the rise in the data observed at lower energies ($E_n \simeq 7$ MeV). It has been shown that this rise is due to compound nucleus processes [Nils81], which were not included in the present analysis.

B. Calculations of the Legendre and Associated Legendre Coefficients

The a_i and b_i coefficients extracted from the angular distribution data shown in Figs. 3-10 and 3-12 were compared to DSD

Table 5-3 Parameters Used in the E1 Particle-Core
Vibrational Coupling Term

Parameter	Value
E_{res}	18.1 MeV
Γ_{res}	4.0 MeV
fraction of classical sum rule	0.67
correction for ground state correlation	0.45
V_1	73.0 MeV
W_1	23.0 MeV
r_a	1.17 fm
r_b	1.26 fm
a	0.75 fm
b	0.58 fm
E1 effective charge of neutron	-0.488

model calculations. The parameters used in the calculation of the initial state and those used to calculate the final single-particle bound state were the same as those used in the calculation of $\sigma(90^\circ)$ (see Tables 5-1 and 5-2). The E1 coupling parameters, from Table 5-3, were also the same. However, the finite size of the odd a_i and b_i coefficients indicated the presence of non-E1 radiation. Therefore, it was necessary to consider E2 and M1 contributions to the calculations.

When only direct E2 was added to the calculations, the odd a_i and b_i coefficients were still very near zero. This is a result of the small quadrupole effective charge of the neutron. It was clearly necessary to add an E2 semidirect term to the calculations to obtain general agreement with the data.

The E2 resonance parameters used for the semidirect calculations were taken principally from the various inelastic α particle scattering studies of the isoscalar E2 resonance in ^{40}Ca . In general, for ^{40}Ca , the position of the E2 resonance was found to be $E_{\text{res}} \approx 18.0$ MeV, with a width from $\Gamma_2 = (2.2 \pm 0.2)$ MeV [Yama78] to (4.0 ± 0.3) MeV [Will80]. The fraction of the E2 sum rule observed varied from $(25 \pm 7)\%$ [Rost79] to 77% [Arvi79]. The parameter set used in the calculation is tabulated in Table 5-4. It represents an "average" parameter set. The results of adding the E2 semidirect term to the calculations using these parameters can be seen as the solid line (for the surface form factor) and the dashed line (for the volume form factor) in Fig. 5-2.

Table 5-4 Parameters Used in the E2 Particle-Core
Vibrational Coupling Term

Parameter	Value
E_{res}	18.0 MeV
Γ_{res}	3.0 MeV
fraction of classical sum rule	0.52
correction for ground state correlation	0.45
V	53.0 MeV
W	0.0 MeV
r_a	1.17 fm
r_b	1.26 fm
a	0.75 fm
b	0.58 fm
E2 effective charge of neutron	0.0119

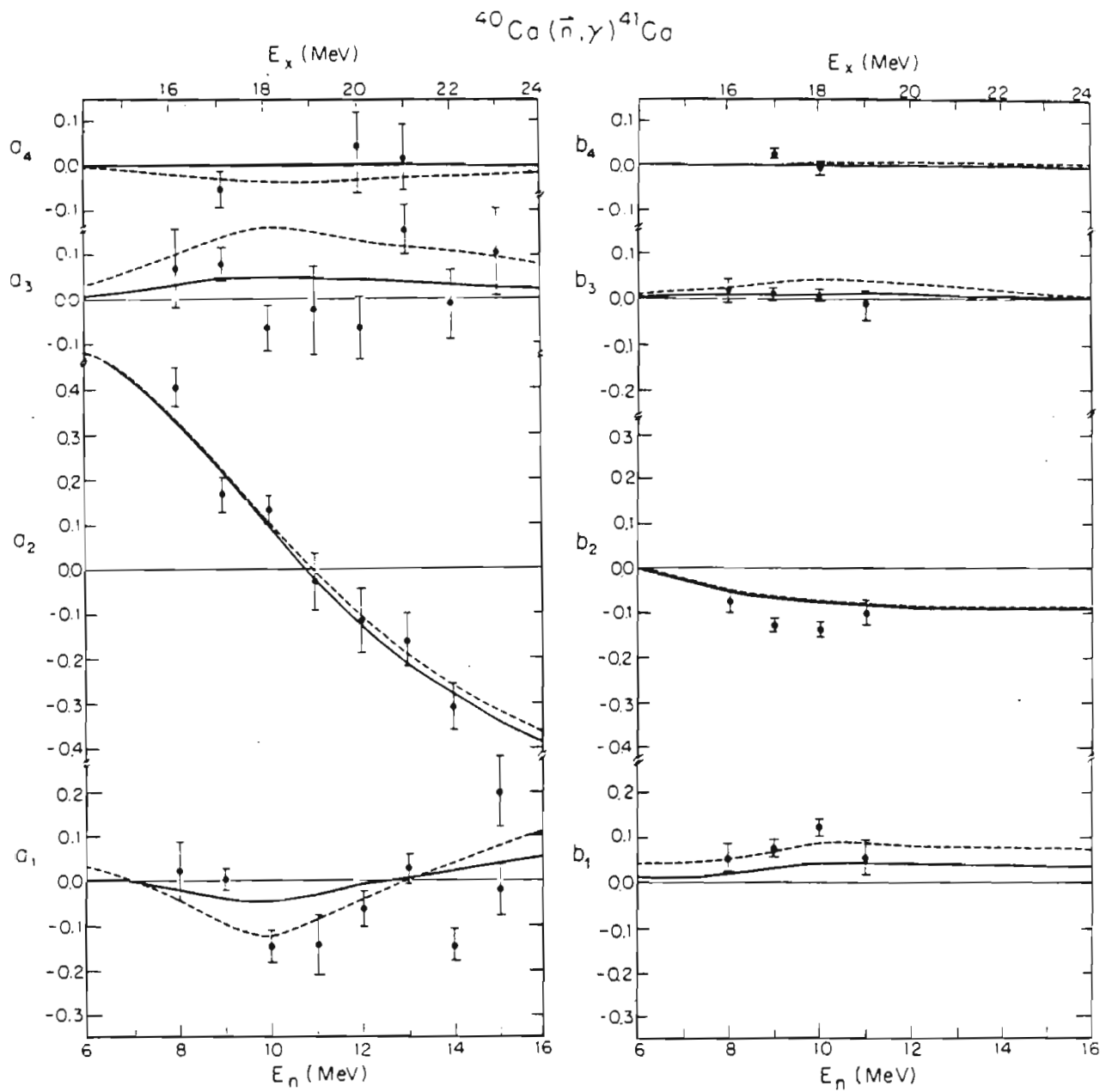


Figure 5-2. DSD model calculations of the a_i and b_i coefficients as described in the text.

Since the calculated E2 cross sections are less than 5% of the total cross section, the addition of the E2 resonance term should have little effect on the calculated a_2 and b_2 coefficients. In fact, the calculations of these coefficients are essentially the same as those from the pure E1 calculation. In addition, the calculated a_4 and b_4 coefficients should be small, since they arise only from E2 effects. This agrees with the results presented in the figure. In general, the calculations of the second and the fourth order coefficients are in good agreement with the coefficients extracted from the data.

The effect of the additional E2 resonance term on the odd a_i and b_i coefficients, however, should be more noticeable in that they are composed of E1-E2 interference terms. The calculated b_3 coefficients are near zero, in general agreement with the values extracted from the data. The calculated a_3 coefficients are positive, while the data clusters (within statistical errors) near zero. In general, the a_3 and b_3 coefficients agree better with the E2 surface form factor calculations. The situation is different for the a_1 and b_1 coefficients, since the general trend of the experimental coefficients is reproduced by the calculations, but the magnitude agrees best in the case of the volume form factor.

Since the a_1 and b_1 coefficients can be affected by the presence of M1 radiation, direct M1 was included in the analysis. The results of adding this term to the calculations can be seen in Fig. 5-3. The solid lines correspond to the E2 surface form factor calculations of Fig. 5-2, and the dotted lines represent the effects of adding direct

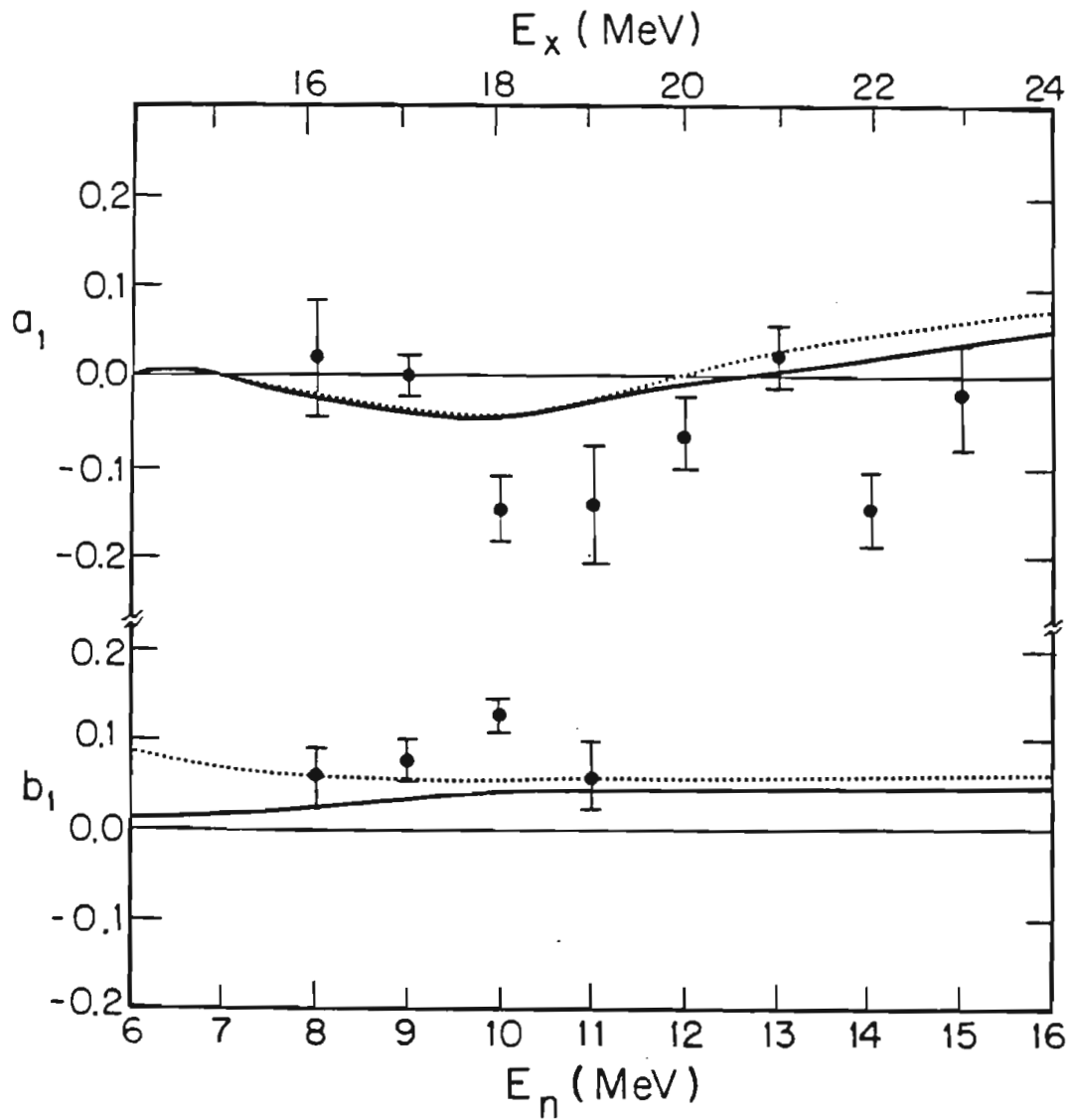


Figure 5-3. DSD model calculations of the a_1 and b_1 coefficients. The solid line corresponds to the solid line in Fig. 4-2. The dotted line is the result of adding a direct M1 term to the calculations.

M1 to the calculations. The agreement between the calculations that include the E2 surface form factor and direct M1 and the experimental b_1 coefficients is now much better, while the effect of adding direct M1 on the a_1 coefficient is small.

C. Calculations of Analyzing Power

Next, a comparison was made between DSD model calculations and the 90° analyzing power data presented in Fig. 3-9. The calculations here were made under the same conditions as above; the initial and final state parameters and the E1 and E2 parameters can be found in Tables 5-1 through 5-4. In this case, the difference between the calculations with the E2 surface form factor and the E2 volume form factor was small. This result is due to the fact that the volume form factor increases both b_1 and b_3 in such a way that $A(90^\circ)$ remains almost unchanged. The results of the calculations using the E2 surface form factor can be seen as the solid line in Fig. 5-4. It is clear that the agreement with the data is not very good. Therefore, a direct M1 term was added to the calculations. The effect produced by this change can be seen from the dotted line (E2 surface and M1 direct) and the dashed line (E2 volume and M1 direct) in the figure. It is clear that the difference between the two form factors is not large. The general trend of the data with energy is fairly well accounted for by the calculations, since the results are relatively independent of the E2 form factors, supporting the conclusion that direct M1 radiation is present in the reaction.

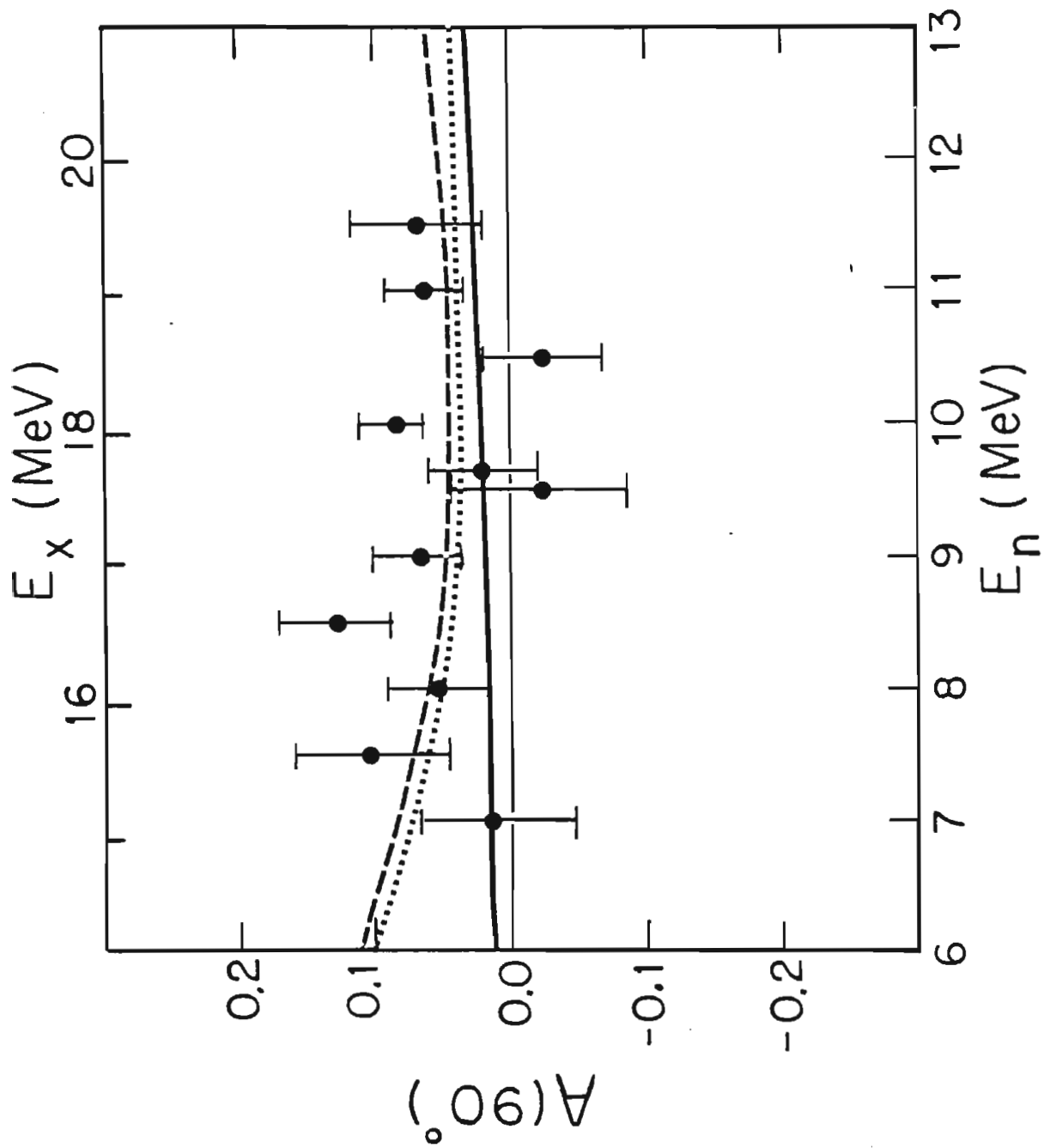


Figure 5-4. DSD model calculations of the 90° analyzing power, as described in the text.

D. Summary

In summary, it appears that the DSD model using the Becchetti-Greenlees optical model parameters does an excellent job of describing the E1 part of the cross section. The large a_1 and b_1 coefficients are in agreement with results of a DSD model calculation in which a volume E2 form factor was used. This calculation gives an order of magnitude more E2 cross section (3.0% of the total cross section at $E_n = 10$ MeV) compared with the values obtained with the surface form factor (0.2% of the total cross section at $E = 10$ MeV). On the other hand, the fits to the a_3 and b_3 coefficients are not as good as those obtained with surface coupling. The addition of direct M1 radiation improves the fit to the b_1 coefficient for the case of the surface form factor, but does not rule out a volume form factor. The measured values of $A(90^\circ)$ clearly require the addition of direct M1 but are insensitive to the E2 form factors. Taken overall, these results support the surface form factor for isoscalar E2 collective strength and the need to include direct M1 in DSD calculations. However, the reason for the large a_1 coefficients is presently unknown.

6. Transition Matrix Amplitude Analysis

A. Pure E1 Analysis

The first step in determining the transition matrix elements of the reaction is to consider only E1 transitions. Since the ground state of ^{41}Ca is $f_{7/2}$, the possible E1 transition matrix elements can be denoted by the incoming partial waves in j-j coupling as $d_{5/2}$, $g_{7/2}$, $g_{9/2}$. Each matrix element is a complex number, and therefore can be written as a real amplitude and phase. The expressions relating these E1 matrix elements to the Legendre coefficients of Eq. 3-7 and the associated Legendre polynomial coefficients of Eq. 3-12 are

$$a_0 = 3 d_{5/2}^2 + 4 g_{7/2}^2 + 5 g_{9/2}^2 \quad 6-1$$

$$\begin{aligned} a_2 = & - 0.4286 d_{5/2}^2 + 0.1905 g_{7/2}^2 - 1.667 g_{9/2}^2 \\ & + 5.669 d_{5/2} g_{9/2} \cos[\phi_{d_{5/2}} - \phi_{g_{9/2}}] \\ & + 0.8571 d_{5/2} g_{7/2} \cos[\phi_{d_{5/2}} - \phi_{g_{7/2}}] \\ & - 0.1260 g_{7/2} g_{9/2} \cos[\phi_{g_{7/2}} - \phi_{g_{9/2}}] \end{aligned}$$

$$\begin{aligned} b_2 = & + 1.890 d_{5/2} g_{9/2} \sin[\phi_{d_{5/2}} - \phi_{g_{9/2}}] \\ & - 1.890 g_{7/2} g_{9/2} \sin[\phi_{g_{7/2}} - \phi_{g_{9/2}}] \\ & - d_{5/2} g_{7/2} \sin[\phi_{d_{5/2}} - \phi_{g_{7/2}}] \end{aligned}$$

and a_0 is normalized to one.

In this case, there are three equations and five unknowns, the $d_{5/2}$, $g_{7/2}$, and the $g_{9/2}$ amplitudes, and the $(\phi_{g_{9/2}} - \phi_{d_{5/2}})$ and $(\phi_{g_{7/2}} - \phi_{d_{5/2}})$ relative phases. This implies that some assumptions must be made in order to make the problem soluble. We can be guided by the DSD calculations which indicate that the the $g_{7/2}$ "spin-flip" amplitude accounts for only a few percent of the total cross section. When this term is neglected, the equations reduce to

$$a_0 = 3 d_{5/2}^2 + 5 g_{9/2}^2 \quad 6-2$$

$$a_2 = - 0.4286 d_{5/2}^2 - 1.667 g_{9/2}^2 \\ + 5.669 d_{5/2} g_{9/2} \cos[\phi_{d_{5/2}} - \phi_{g_{9/2}}]$$

$$b_2 = 1.890 d_{5/2} g_{9/2} \sin[\phi_{d_{5/2}} - \phi_{g_{9/2}}]$$

There are now three equations and three unknowns. Because of the quadratic nature of these expressions, when they are inverted and solved in terms of the amplitudes and relative phase, two solutions are found.

However, it is also possible to determine the amplitudes and the relative phase by a non-linear least-squares fit to the data. This method produces essentially the same two solutions as the one described above, where the amplitudes and relative phase are determined from the a_i and b_i coefficients that have been extracted from the data. The two solutions that were determined from the coefficients are tabulated in Table 6-1, while those that were derived directly from the data are listed in Table 6-2. Fig. 6-1 shows the solutions derived directly from the data.

Table 6-1 Results of Pure E1 Analysis
Based on the Extracted a_2 and b_2 Coefficients

Solution 1					
E_n (MeV)	a_2^+	b_2^\ddagger	$\sigma(g_{9/2})/\sigma(\text{tot})$ (percent)	$\phi_{g_{9/2}} - \phi_{d_{5/2}}$ (degrees)	
8.0	0.403 ± 0.043	-0.079 ± 0.026	25.8 ± 8.4	22 ± 7	
9.0	0.164 ± 0.039	-0.134 ± 0.014	15.1 ± 3.2	50 ± 5	
10.0	0.131 ± 0.032	-0.143 ± 0.015	15.1 ± 3.1	55 ± 4	
11.0	-0.028 ± 0.065	-0.104 ± 0.028	5.6 ± 3.0	68 ± 11	
Solution 2					
8.0			63.0 ± 9.4	20 ± 6	
9.0			77.9 ± 3.9	41 ± 4	
10.0		= same as above =	78.4 ± 3.6	45 ± 4	
11.0			90.7 ± 19.0	47 ± 10	

⁺ From Tables 3-8 and 3-9

[‡] From Tables 3-11 and 3-12

Table 6-2

Results of Pure E1 Analysis
Based on Direct Fit to Data

Solution 1		
E_n (MeV)	$\sigma(g_{9/2})/\sigma(\text{tot})$ (percent)	$\varphi_{g_{9/2}} - \varphi_{d_{5/2}}$ (degrees)
8.0	23.2 ± 8.7	24 ± 6
9.0	16.4 ± 2.8	46 ± 3
10.0	13.1 ± 2.4	47 ± 4
11.0	7.6 ± 3.1	55 ± 9
Solution 2		
8.0	61.6 ± 8.6	22 ± 6
9.0	75.9 ± 3.0	38 ± 3
10.0	79.8 ± 2.6	38 ± 4
11.0	87.1 ± 3.6	41 ± 8

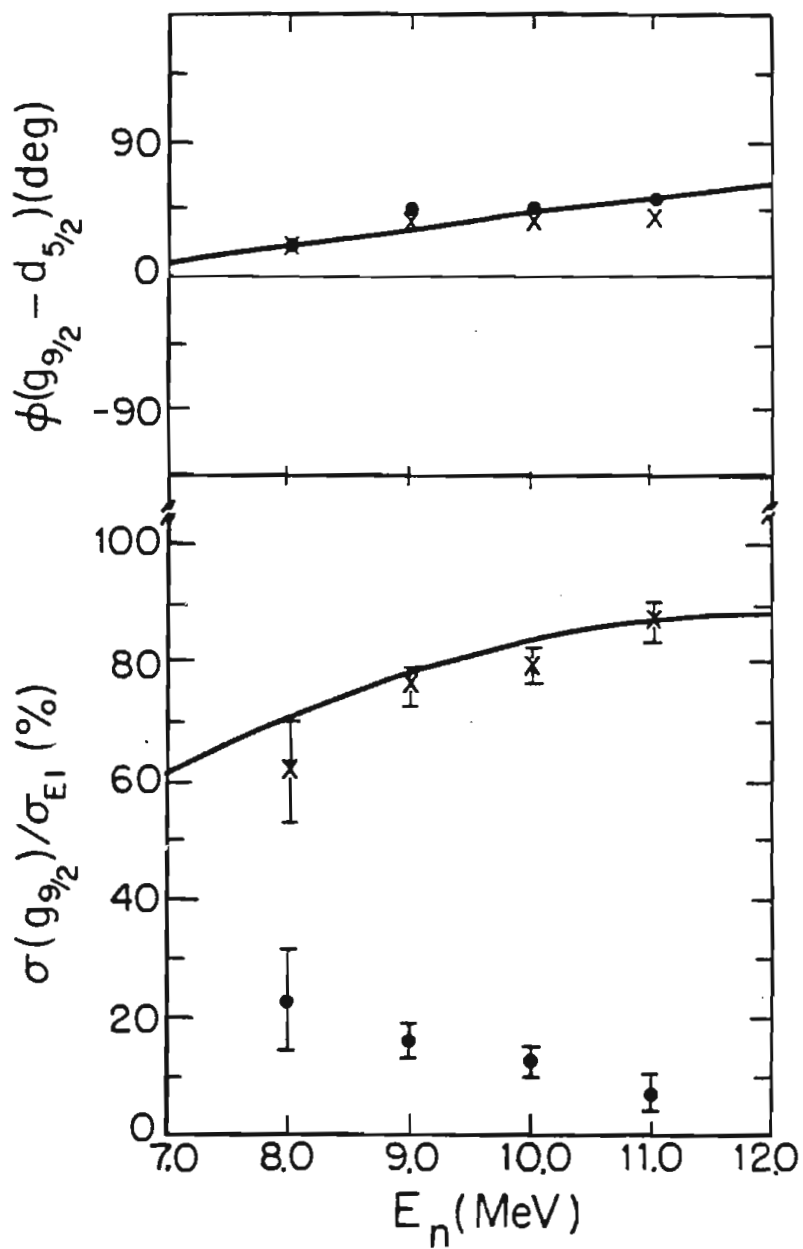


Figure 6-1. Percent $\sigma_{g_{9/2}}$ of the total E1 cross section and the $\phi_{g_{9/2}} - \phi_{d_{5/2}}$ relative phase determined by a pure E1 analysis of the data. The solid lines represent a DSD model calculation.

From the figure, it can be seen that one solution has a dominant $g_{9/2}$ amplitude, while the other has a dominant $d_{5/2}$ amplitude. The solid line is the result of a DSD calculation, and it clearly favors the solution where the $g_{9/2}$ amplitude accounts for most of the cross section. The theoretical calculations agree quite well with the data analysis, predicting not only the magnitude of the amplitudes, but also their change as a function of energy. The corresponding values of the relative phase are shown at the top of Fig. 6-1, along with the DSD calculations. In this case, the two solutions are essentially the same; however, as before, the calculations agree very well with both the phase values extracted from the data as well as the general trend of the phases with energy.

B. E1-E2 Analysis

The existence of non-zero odd a_i and b_i coefficients in the polynomial expansions of § 5-B indicate the presence of non-E1 radiation. However, the introduction of E2 amplitudes into the analysis complicates the problem still further. According to the selection rules discussed earlier, the possible E2 amplitudes are the $P_{3/2}$, $f_{5/2}$, $f_{7/2}$, $h_{9/2}$, and $h_{11/2}$ amplitudes. Even though the odd Legendre and associated Legendre coefficients, containing E1-E2 interference terms, can now be introduced, there are five additional amplitudes and five more relative phases. Even neglecting the $g_{7/2}$ E1 "spin-flip" term, there are now nine equations but fifteen unknowns, eight amplitudes and seven relative phases. Once again, a

model-independent analysis is impossible.

As it was mentioned earlier, there are three possibilities for the E2 form factor in the semidirect term, one proportional to r^2 , the commonly preferred surface peaked form factor, and a volume form factor. Preliminary calculations were done with each of the form factors to determine the relative size of the E2 amplitudes in the three cases, to see if any of them could be eliminated from the transition matrix analysis. It was found that using the form factor proportional to r^2 , the contributions from the $h_{11/2}$ and the $f_{7/2}$ amplitudes dominated the E2 cross section. Using the surface-peaked form factor, the $h_{11/2}$ and the $p_{3/2}$ contributions were largest, while in the case of the volume form factor, the $h_{11/2}$, $f_{7/2}$, and $p_{3/2}$ all were comparable in size.

From these results, it was clear that the $f_{5/2}$ and the $h_{9/2}$ E2 "spin-flip" amplitudes could be neglected from the analysis. However, it was not possible to unambiguously determine which of the other E2 amplitudes could be eliminated. Therefore, the analysis was done in two different ways, one using the $h_{11/2}$ and the $f_{7/2}$ E2 amplitudes, and the other using the $h_{11/2}$ and the $p_{3/2}$ E2 amplitudes. In either case, there were nine equations and seven unknowns, two E1 amplitudes, two E2 amplitudes, and three relative phases. In the first case, including the $h_{11/2}$ and the $p_{3/2}$ amplitudes, the equations become

$$a_0 = 3 d_{5/2}^2 + 5 g_{9/2}^2 + 2 p_{3/2}^2 + 6 h_{11/2}^2 \quad 6-3$$

$$a_1 = - 5.091 d_{5/2} p_{3/2} \cos[\varphi_{d_{5/2}} - \phi_{p_{3/2}}] \\ + 13.29 g_{9/2} h_{11/2} \cos[\varphi_{g_{9/2}} - \phi_{h_{11/2}}]$$

$$a_2 = - 0.4286 d_{5/2}^2 - 1.667 g_{9/2}^2 + 0.2857 p_{3/2}^2 \\ + 2.727 h_{11/2}^2$$

$$+ 5.669 d_{5/2} g_{9/2} \cos[\varphi_{d_{5/2}} - \phi_{g_{9/2}}]$$

$$a_3 = 0.2424 d_{5/2} p_{3/2} \cos[\varphi_{d_{5/2}} - \phi_{p_{3/2}}] \\ + 8.374 d_{5/2} h_{11/2} \cos[\varphi_{d_{5/2}} - \phi_{h_{11/2}}] \\ - 5.345 g_{9/2} p_{3/2} \cos[\varphi_{g_{9/2}} - \phi_{p_{3/2}}] \\ - 3.446 g_{9/2} h_{11/2} \cos[\varphi_{g_{9/2}} - \phi_{h_{11/2}}]$$

$$a_4 = - 1.454 h_{11/2}^2 \\ - 1.573 p_{3/2} g_{9/2} \cos[\varphi_{p_{3/2}} - \phi_{g_{9/2}}] \\ - 7.895 p_{3/2} h_{11/2} \cos[\varphi_{p_{3/2}} - \phi_{h_{11/2}}]$$

$$b_1 = 2.546 d_{5/2} p_{3/2} \sin[\varphi_{d_{5/2}} - \phi_{p_{3/2}}] \\ + 6.647 g_{9/2} h_{11/2} \sin[\varphi_{g_{9/2}} - \phi_{h_{11/2}}]$$

$$b_2 = 1.89 d_{5/2} g_{9/2} \sin[\varphi_{d_{5/2}} - \phi_{g_{9/2}}]$$

$$b_3 = - 0.0202 d_{5/2} p_{3/2} \sin[\varphi_{d_{5/2}} - \phi_{p_{3/2}}] \\ + 2.094 d_{5/2} h_{11/2} \sin[\varphi_{d_{5/2}} - \phi_{h_{11/2}}] \\ + 1.336 g_{9/2} p_{3/2} \sin[\varphi_{g_{9/2}} - \phi_{p_{3/2}}] \\ - 0.2872 g_{9/2} h_{11/2} \sin[\varphi_{g_{9/2}} - \phi_{h_{11/2}}]$$

$$b_4 = - 1.579 p_{3/2} h_{11/2} \sin[\varphi_{p_{3/2}} - \phi_{h_{11/2}}]$$

and for the second case where the $h_{11/2}$ and the $f_{7/2}$ amplitudes are taken into consideration,

$$a_0 = 3 d_{5/2}^2 + 5 g_{9/2}^2 + 4 f_{7/2}^2 + 6 h_{11/2}^2$$

$$a_1 = 4.454 d_{5/2} f_{7/2} \cos[\phi_{d5/2} - \phi_{f7/2}] - 3.055 g_{9/2} f_{7/2} \cos[\phi_{g9/2} - \phi_{f7/2}] + 13.29 g_{9/2} h_{11/2} \cos[\phi_{g9/2} - \phi_{h11/2}]$$

$$a_2 = -0.4286 d_{5/2}^2 - 1.667 g_{9/2}^2 - 1.088 f_{7/2}^2 + 2.727 h_{11/2}^2 + 5.669 d_{5/2} g_{9/2} \cos[\phi_{d5/2} - \phi_{g9/2}] - 3.223 f_{7/2} h_{11/2} \cos[\phi_{f7/2} - \phi_{h11/2}]$$

$$a_3 = -1.979 d_{5/2} f_{7/2} \cos[\phi_{d5/2} - \phi_{f7/2}] + 8.374 d_{5/2} h_{11/2} \cos[\phi_{d5/2} - \phi_{h11/2}] + 5.237 g_{9/2} f_{7/2} \cos[\phi_{g9/2} - \phi_{f7/2}] - 3.446 g_{9/2} h_{11/2} \cos[\phi_{g9/2} - \phi_{h11/2}]$$

$$a_4 = -1.959 f_{7/2}^2 - 1.454 h_{11/2}^2 + 6.446 f_{7/2} h_{11/2} \cos[\phi_{f7/2} - \phi_{h11/2}]$$

$$b_1 = 2.227 d_{5/2} f_{7/2} \sin[\phi_{d5/2} - \phi_{f7/2}] + 1.528 g_{9/2} f_{7/2} \sin[\phi_{g9/2} - \phi_{f7/2}] + 6.647 g_{9/2} h_{11/2} \sin[\phi_{g9/2} - \phi_{h11/2}]$$

$$b_2 = 1.89 d_{5/2} g_{9/2} \sin[\phi_{d5/2} - \phi_{g9/2}] - 1.074 f_{7/2} h_{11/2} \sin[\phi_{f7/2} - \phi_{h11/2}]$$

$$\begin{aligned}
b_3 = & - 0.1650 d_{5/2} f_{7/2} \sin[\phi_{d_{5/2}} - \phi_{f_{7/2}}] \\
& + 2.094 d_{5/2} h_{11/2} \sin[\phi_{d_{5/2}} - \phi_{h_{11/2}}] \\
& - 0.4364 g_{9/2} f_{7/2} \sin[\phi_{g_{9/2}} - \phi_{f_{7/2}}] \\
& - 0.2872 g_{9/2} h_{11/2} \sin[\phi_{g_{9/2}} - \phi_{h_{11/2}}]
\end{aligned}$$

$$b_4 = 0.6446 f_{7/2} h_{11/2} \sin[\phi_{f_{7/2}} - \phi_{h_{11/2}}]$$

The program DATAAMP [Came77] was used to search for the best fit of the amplitudes and relative phases to the data using a non-linear least squares criterion [Jens81]. Since the calculations predict that the E2 cross section is less than 5% of the total cross section in this energy range, the $h_{11/2}$ and the $f_{7/2}$ (case 1) or the $p_{3/2}$ (case 2) amplitudes were allowed to vary from 0% to 5% of the total cross section, in 0.5% steps. The $d_{5/2}$ and $g_{9/2}$ E1 amplitudes were restricted to 0% to 50% and to 50% to 100% of the total cross section, respectively, consistent with the pure E1 analysis of the previous section. This was done to locate approximately the χ^2 minima. Once the minima were found, the procedure was repeated, but the E2 amplitudes were unrestricted, and allowed to vary freely between 0% to 5% of the total cross section, and with the starting values of the search set at the minima found in the grid search. The solutions that were found in this manner are listed in Tables 6-3 and 6-4 with the corresponding values of χ^2 . As expected, the addition of E2 terms to the search has only a small effect on the $d_{5/2}$ and $g_{9/2}$ E1 contributions to the total cross section.

It is perhaps interesting to examine the χ^2 contours resulting from the search procedure described above. Figs. 6-2 and 6-3 give

Table 6-3 Solutions of E1-E2 Transition Matrix Analysis
for Search on $f_{7/2}$ and $h_{11/2}$ Amplitudes

E_n	$\%d_{5/2}$	$\%g_{9/2}$	$\%f_{7/2}$	$\%h_{11/2}$	$\phi_{g_{9/2}} - \phi_{d_{5/2}}$	$\phi_{f_{7/2}} - \phi_{d_{5/2}}$	$\phi_{h_{11/2}} - \phi_{d_{5/2}}$	χ^2
8.0	37.9 ± 10.5	60.9 ± 11.5	0.8 ± 3.4	0.4 ± 0.9	20 ± 7	13 ± 70	-68 ± 34	0.54
9.0	23.9 ± 2.4	71.8 ± 2.3	2.4 ± 1.1	1.9 ± 1.0	38 ± 3	146 ± 15	-37 ± 7	1.24
10.0	24.4 ± 2.5	73.2 ± 2.3	1.5 ± 3.1	1.0 ± 0.7	38 ± 4	-73 ± 22	-106 ± 9	0.48
11.0	8.4 ± 5.2	89.5 ± 5.8	1.2 ± 3.8	0.9 ± 1.0	47 ± 12	180 ± 61	-88 ± 35	2.07

Table 6-4 Solutions of E1-E2 Transition Matrix Analysis
for Search on $p_{3/2}$ and $h_{11/2}$ Amplitudes

E_n	%d5/2	%g9/2	%p3/2	%h11/2	$\phi_{g9/2}^{-\phi_{d5/2}}$	$\phi_{p3/2}^{-\phi_{d5/2}}$	$\phi_{h11/2}^{-\phi_{d5/2}}$	χ^2
8.0	39.2 ± 14.7	60.2 ± 14.1	0.5 ± 1.8	0.05 ± 0.4	19 ± 6	-120 ± 114	-109 ± 198	0.54
9.0	23.8 ± 3.2	75.7 ± 3.0	0.3 ± 0.4	0.3 ± 0.3	38 ± 4	-80 ± 34	-46 ± 17	1.35
10.0	23.3 ± 1.1	69.8 ± 1.0	2.9 ± 1.3	4.3 ± 0.7	38 ± 4	85 ± 11	-56 ± 7	0.54
11.0	9.3 ± 4.3	87.6 ± 7.2	1.5 ± 3.0	1.6 ± 1.7	54 ± 15	103 ± 36	-76 ± 18	2.03

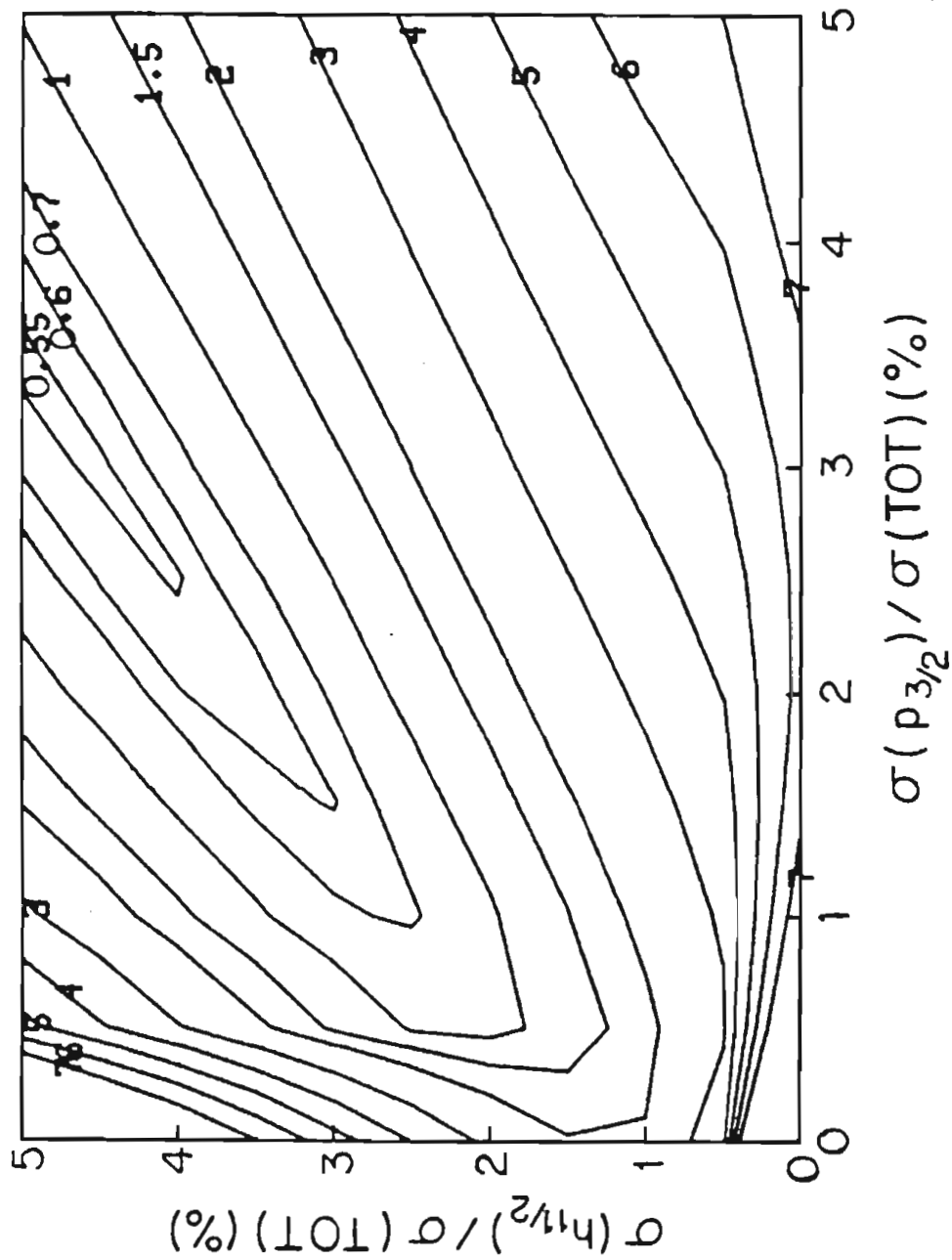
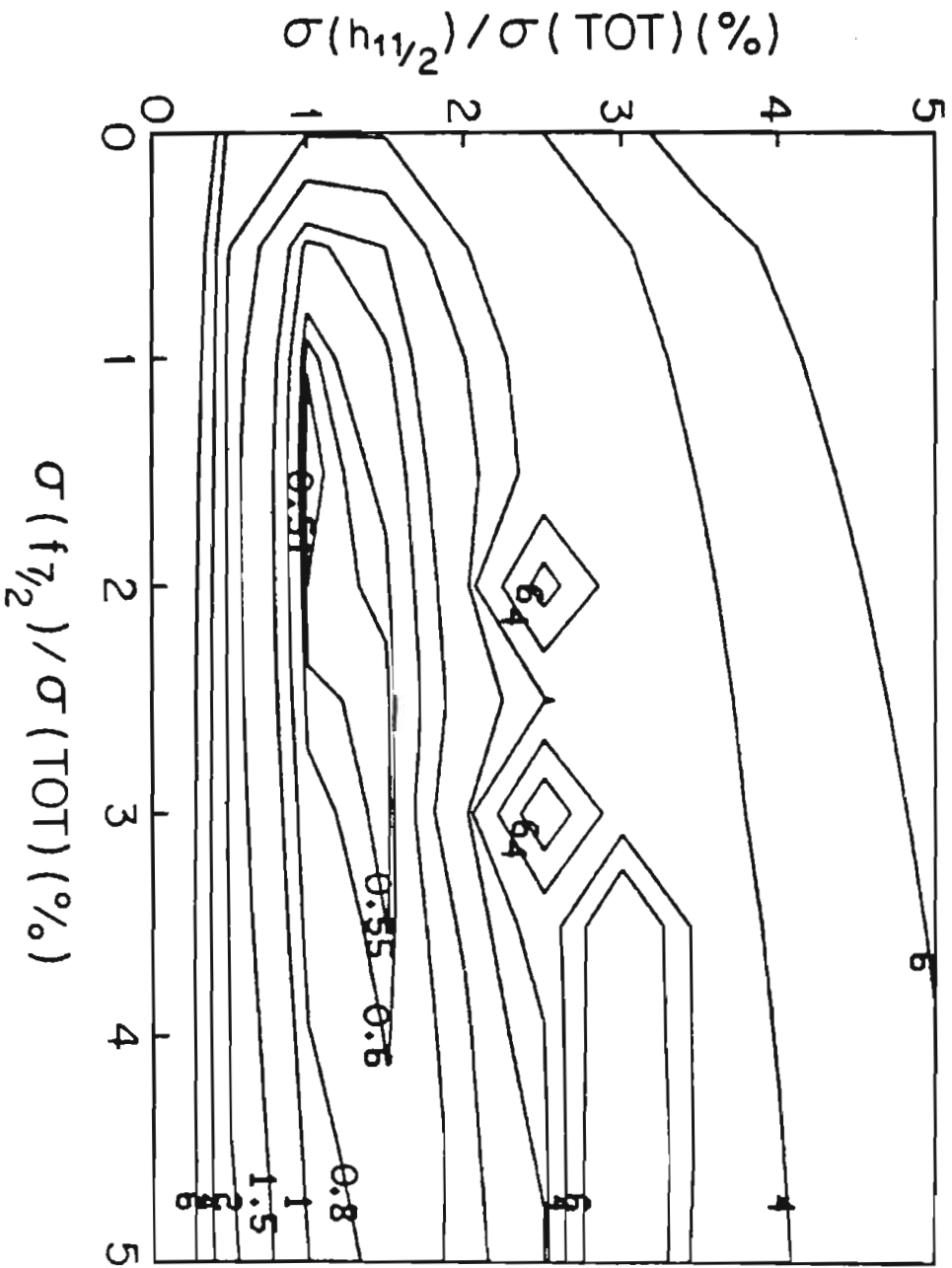


Figure 6-2. Contour plot produced by a χ^2 search on the $p_{3/2}$ and $h_{11/2}$ amplitudes at $E_n = 10$ MeV.

Figure 6-3. Contour plot produced by a χ^2 search on the $f_{7/2}$ and $h_{11/2}$ amplitudes at $E_n = 10$ MeV.



contour plots generated at $E_n = 10$ MeV for the search on the $p_{3/2}$ and $h_{11/2}$, and the $f_{7/2}$ and $h_{11/2}$ amplitudes, respectively. In the first case, the χ^2 contour is smoothly changing with energy, with a minimum along the upper $h_{11/2}$ boundary, corresponding to $\sigma(p_{3/2})/\sigma(\text{tot}) \simeq 3\%$ and $\sigma(h_{11/2})/\sigma(\text{tot}) \simeq 5\%$, for an E2 cross section of 8% of the total cross section. In the second case, there is more structure, with two steep maxima in the center of the plot, and a distinct minimum in the region where $1\% \leq \sigma(f_{7/2})/\sigma(\text{tot}) \leq 2\%$, and $\sigma(h_{11/2})/\sigma(\text{tot}) \simeq 1\%$, for a total E2 cross section from 2% to 3%.

7. Conclusions

The results of this study of the $^{40}\text{Ca}(n,\gamma_0)^{41}\text{Ca}$ reaction are as follows:

1) The $\sigma(90^\circ)$ yield curve which was measured from $E_n(E_\gamma) = 6$ (14.2) to 17 (24.9) MeV was reproduced quite well by a direct-semidirect model calculation which included only E1 radiation. When these (n,γ_0) cross sections were converted, using the principle of detailed balance, to the $\sigma_t(\gamma,n_0)$ cross sections, 1.6% of the classical electric dipole sum rule was found to be exhausted in this channel.

2) The a_2 and b_2 coefficients, measured in 1 MeV steps from $E_n = 8$ to 15 MeV, also agree quite well with the DSD calculations which includes only E1 radiation. This is especially true for the a_2 coefficients.

3) However, the finite size of the a_1 and the b_1 coefficients extracted from the angular distributions indicated that non-E1 radiation is present in the reaction. A DSD calculation which included collective E2 radiation gave the correct energy dependence, but magnitudes that were too small when the accepted surface-peaked form factor was used. By using a volume E2 form factor, it was found that the agreement between the calculations and the a_1 and b_1

coefficients was improved. Unfortunately, the effect on the predicted a_3 and b_3 coefficients was the opposite.

4) The measured a_3 , b_3 , a_4 , and b_4 coefficients are zero within experimental error. The E1-E2 DSD calculations with the surface-peaked E2 form factor are in agreement with these observations.

5) The addition of a direct M1 term to the E1-E2 DSD calculations (as in (4) above) improved the fit to the b_1 coefficients but made very little change in the a_1 coefficients.

6) The additional direct M1 term also made a significant difference in the calculated values of the 90° analyzing power. In this case, the calculations are insensitive to the E2 form factor and agree with the measured $A(90^\circ)$ values only if direct M1 radiation is included.

7) An approximately model-independent analysis was carried out to determine the E1 transition matrix elements for the (n, γ_0) reaction. Neglecting the $g_{7/2}$ "spin-flip" amplitude, two solutions were found, one where the $g_{9/2}$ amplitude accounted for about 80% of the E1 cross section, and the other where the $d_{5/2}$ amplitude accounted for 85% of the cross section. The DSD model calculations indicated that the former solution is the correct one.

8) An expanded analysis was made to determine both the E1 and E2 T-matrix elements. In this case, the $g_{7/2}$, $h_{9/2}$, and $f_{5/2}$ "spin-flip" terms were neglected. In addition, the analysis was performed in two

ways, first by including the $h_{11/2}$ and $p_{3/2}$ E2 amplitudes in the least-squares fit, and second by including the $h_{11/2}$ and $f_{7/2}$ E2 amplitudes. Both ways lead to satisfactory fits with similar χ^2 values. These fits indicated only that the E2 contribution to the total cross section is less than about 8%. This $\sigma(E2)$ is of the order of ten times as large as that predicted by the E1-E2 DSD model calculations made with the surface-peaked E2 form factor.

In conclusion, our calculations based on the direct-semidirect model of radiative nucleon capture describe reasonably well our experimental results for the $^{40}\text{Ca}(n, \gamma_0)^{41}\text{Ca}$ reaction. The best agreement between these calculations and the data were found when a surface-peaked E2 form factor was used and when terms describing direct M1 radiation were included. The main discrepancy which remains involves the large a_1 coefficients extracted from the data. This disagreement is at present not understood.

APPENDIX A

The addition of the second NaI crystal to our experimental set-up created the necessity of rewriting parts of our data reduction code, DATAAMP, originally programmed by C. Cameron [Came77]. The main effect of the second detector on cross section measurements is to increase the number of counts for a given run time. For an analyzing power measurement with a detector at the same angle on both the right and the left sides of the beam line, the analyzing power is defined as

$$A(\theta) = \frac{1}{P} * \frac{r - 1}{r + 1} \quad A-1$$

where

$$r = \sqrt{\frac{LU * RD}{LD * RU}} \quad A-2$$

LU (LD) = the number of counts in the left detector in the spin
up (down)state

RU (RD) = the number of counts in the right detector in the spin
up (down) state

and where P is the polarization and we have defined the spin "up" and spin "down" directions according to the Madison Convention [Bars70]. Therefore, the use of a second detector in analyzing power measurements allows the cancellation of any normalization factors between the two detectors and between the two spin states.

The program SCRAP was developed by K. Murphy [Murp82] to deal with neutron time-of-flight data taken with two detectors. Though his analysis had to be modified somewhat to accommodate the different experimental techniques of photonuclear work, the basic derivations are the same in each case. A suitable version of SCRAP was substituted for the one-detector data reduction section of DATAAMP and is described below. The fitting routines in DATAAMP remained unchanged.

In this appendix, the general expressions for cross section and analyzing power will be presented. These general expressions are more complicated than those above, since they include the possibility of different polarizations in the spin up and spin down states, spin up to spin down beam ratio calculations, and, when appropriate, the relative efficiency of the two detectors. In addition, the error analysis is presented, including the error introduced by the subtraction of background from the spectra. In this formalism, all data are to be considered normalized either to a monitor at zero degrees, where the analyzing power is zero, or to the integrated beam current (BCI).

B. Description of Scrap

The program Scrap calculates cross sections and analyzing powers with the associated errors for data taken with one detector or with two detectors set at the same angle. Since data is usually taken with both detectors at the same angle, all cross section calculations

passed into the fitting routines are first normalized to two detector values. For data taken with the two detectors set at different angles, this requires the knowledge of the left to right detector relative efficiency and its error.

The following independent variables are input to the program:

ELER, d(ELER)	the left to right detector relative efficiency and its error (default is 1.00 +/- 0.02)
NRUN	the run number
θ_r	the angle of the right detector relative to the beam direction
θ_l	the angle of the left detector relative to the beam direction
RUT, d(RUT) RDT, d(RDT) LUT, d(LUT) LDT, d(LDT)	the total number of counts in each detector for each spin state along with the associated errors (includes background)
RB, d(RB) LB, d(LB)	the average backgrounds in each detector with errors (= 0.5 * (spin up background + spin down background))
ARB, d(ARB) ALB, d(ALB)	the analyzing powers of these backgrounds with errors
PU, d(PU) PD, d(PD)	the neutron or proton polarizations in the spin up and spin down states and errors (PU > 0 and PD < 0)
MU, d(MU) MD, d(MD)	the monitor or BCI counts in each spin state and errors

In the case of unpolarized data, the polarization and analyzing power variables are input as zero and only one set of data is input

per detector.

The program distinguishes runs where the two detectors were at the same angle (two-detector runs) by comparing θ_r and θ_l . It then calculates the relative cross sections and analyzing powers for the two detector runs. The cross sections are then divided into their right and left detector contributions based on the value of the left to right detector relative efficiency calculated from the data just reduced. The expression for the relative efficiency between the detectors is

$$ELR = \frac{LU}{RU} * \frac{1 - PU * A(\theta)}{1 + PU * A(\theta)} \quad A-3$$

where $A(\theta)$ is the analyzing power of the two-detector run. Note that we use a different symbol here for the relative efficiency, to distinguish it from ELER. In principle, these two quantities should be the same.

Next, the program calculates the same quantities for the runs where the two detectors were at different angles (one-detector runs) and normalizes the values of the cross section to the two-detector values based on the value of ELER and $d(ELER)$. The expressions relating the various cross sections are

$$\begin{aligned} \sigma_{r2} &= \sigma_r * (1 + ELER) \\ \sigma_{l2} &= \sigma_l * (1 + 1/ELER) \end{aligned} \quad A-4$$

and

$$\begin{aligned} \sigma_{2r} &= \sigma_2 / (1 + ELR) \\ \sigma_{2l} &= \sigma_2 / (1 + 1/ELR) \end{aligned}$$

where

$\sigma_r (\sigma_l)$ = the one-detector cross section calculated from the right (left) detector only

$\sigma_{r2} (\sigma_{l2})$ = the two detector cross section calculated from σ_r (σ_l) and ELER

σ_2 = the two detector cross section

$\sigma_{2r} (\sigma_{2l})$ = the right (left) detector cross section calculated from σ_2 and ELR

The values of σ_2 , $d(\sigma_2)$, $(\sigma_2 * A(\theta))$, and $d(\sigma_2 * A(\theta))$ are then fed to the rest of the program to be fitted and plotted.

C. General Expressions

All the expressions for cross section and analyzing power presented in this appendix can be derived from a few basic relationships.

$$\begin{aligned}
 LJ &= \sigma(\theta) * (1 + PU * A(\theta)) * BU * EFFL & A-5 \\
 LD &= \sigma(\theta) * (1 + PD * A(\theta)) * BD * EFFL \\
 RU &= \sigma(\theta) * (1 - PU * A(\theta)) * BU * EFR \\
 RD &= \sigma(\theta) * (1 - PD * A(\theta)) * BD * EFR \\
 MU &= \sigma(\theta_m) * (1 + PU * A(\theta_m)) * BU * EFM \\
 MD &= \sigma(\theta_m) * (1 + PD * A(\theta_m)) * BD * EFM
 \end{aligned}$$

where the left and the right detectors are assumed to be at an angle θ , the monitor is located at an angle θ_m on the left side of the beam line and where the other symbols are as follows:

- LU (LD) = the net counts in the left detector in the spin up
 (down) state
 RU (RD) = the net counts in the right detector in the spin up
 (down) state
 MU (MD) = the net counts in the monitor detector in the spin up
 (down) state
 $\sigma(\theta)$ = the capture reaction cross section at angle θ
 $\sigma(\theta_m)$ = the elastic scattering cross section at angle θ_m
 $A(\theta)$ = the analyzing power at angle θ
 $A(\theta_m)$ = the analyzing power at angle θ_m
 PU (PD) = the neutron polarization in the spin up (down) state
 (PU > 0, PD < 0)
 BU (BD) = the total amount of beam in the spin up (down) state
 EFFL = the efficiency of the left detector
 EFFR = the efficiency of the right detector
 EFFM = the efficiency of the monitor detector

The last three quantities, EFFL, EFFR, EFFM contain all factors associated with the efficiency of the respective detectors, such as the detection efficiency of the crystal ϵ and the solid angle of the detector Ω .

For data taken with unpolarized beam, the equations reduce to

$$\begin{aligned}
 RN &= \sigma(\theta) * BN * EFFR & A-6 \\
 LN &= \sigma(\theta) * BN * EFFL
 \end{aligned}$$

where BN is the total integrated unpolarized beam current and RN (LN) is the net counts in the right (left) detector.

D. Backgrounds

For unpolarized data, background is easily handled. It is simply subtracted from the total number of counts and the error in the background is taken into account in the final error analysis (to be described later). That is,

$$\begin{aligned} LN &= LT - LB & A-7 \\ RN &= RT - RB \end{aligned}$$

where RT (LT) and RB (LB) are the total counts and the background, respectively in the right (left) detector.

For polarized data, the situation is complicated by the fact that the background observed might have a nonzero analyzing power. This would imply that any error made in the estimate of this background would affect a spin up measurement in the opposite way from a spin down measurement for a given detector. In fact, this may be an important effect to consider, since in experiments with low yields and high backgrounds, it could have a sizeable influence on subsequent calculations. For the two detector set-up, it can be shown that the true backgrounds are related to the average backgrounds and the measured analyzing powers of the backgrounds by the expressions

$$LUB = \frac{2 * LB}{(1 + A^+ * BB)} \qquad LDB = \frac{2LB * A^+ * BB}{(1 + A^+ * BB)} \qquad A-8$$

$$RUB = \frac{2 * RB}{(1 + A^- * BB)} \qquad RDB = \frac{2RB * A^- * BB}{(1 + A^- * BB)}$$

where

$$A^+ = \frac{1 + PD * ALB}{1 + PU * ALB} \qquad A^- = \frac{1 - PD * ARB}{1 - PU * ARB}$$

where $BB = BD/BU$. (See also the discussion below in § E.)

The equations for the net counts are now

$$\begin{aligned} LU &= LUT - LUB \\ LD &= LDT - LDB \\ RU &= RUT - RUB \\ RB &= RDT - RDB \end{aligned} \qquad A-9$$

E. Beam Ratio Calculations

It is now necessary to consider the calculation of the spin down to spin up beam ratio, $BB = BD/BU$, which will eventually be used in the expressions for the normalization between runs. Using the last two equations in [A-5], it is easy to see that

$$BB = \frac{BD}{BU} = \frac{MD * (1 + PU * A(\theta_m))}{MU * (1 + PD * A(\theta_m))} \qquad A-10$$

Since the monitor is located at zero degrees, this reduces to the simple form

$$\frac{BD}{BU} = \frac{MD}{MU} \qquad A-11$$

(This final expression has the added feature that the monitor counts can be replaced by the BCI, which is often a more convenient method of normalization.)

F. Normalization Techniques

Even though the data at this point have been corrected for the spin up to spin down beam ratio, it is still necessary to have some sort of standard against which to normalize the data from run to run. This is done by using the monitor. The important factor to know is $(\sigma_m(\theta)*EFFM)$, which can be determined from the number of counts in the monitor. From Eq. A-5,

$$\sigma(\theta_m)*EFFM = \frac{(PD*MU/BU - PU*MD/BD)}{PD - PU} \quad A-13$$

It will be seen later in the description of cross section and analyzing power calculations that the factor $(PD-PU)$ in the denominator will eventually cancel out, and that it will be important to know only the ratio of BD/BU , and not the separate values.

For unpolarized data, once again the general expression simplifies to give

$$\sigma(\theta_m)*EFFM = MN/BN \quad A-14$$

In this case, for normalization to an unpolarized monitor, it will be found that the final expressions contain no reference to the total beam.

G. Cross Section

From Eq. A-5, it can easily be determined that

$$\sigma_r = \frac{\sigma(\theta)*EFFR}{\sigma(\theta_m)*EFFM} = \frac{-PD*RU*BB + PU*RD}{-PD*MU*BB + PU*MD} \quad A-15$$

for the right detector, and

$$\sigma_l = \frac{\sigma(\theta)*EFFL}{\sigma(\theta_m)*EFFM} = \frac{PD*LU*BB - PU*LD}{PD*MU*BB - PU*MD} \quad A-16$$

for the left detector. Note that σ_r and σ_l are now expressed relative to the monitor and have units of detector counts/monitor counts.

These are the expressions used to calculate cross sections in the case where the two detectors are at different angles, with BB given by Eq. A-11. To get the two detector cross sections for the case where the two detectors are at the same angle, it is only necessary to add these two equations together.

$$\sigma_2 = \sigma_r + \sigma_l = \frac{-PD*BB*(LU + KU) + PU*(RD + LD)}{-PD*MU*BB + PU*MD} \quad A-17$$

As noted earlier, the two detector cross section represents the sum of the single detector measurements, and not their average.

For unpolarized data, the equations are

$$\sigma_r = \frac{\sigma(\theta)*EFFR}{\sigma(\theta_m)*EFFM} = RN/MN \quad A-18$$

$$\sigma_l = \frac{\sigma(\theta)*EFFL}{\sigma(\theta_m)*EFFM} = LN/MN$$

$$\sigma_2 = \sigma_r + \sigma_l = \frac{RN + LN}{MN}$$

To fit these cross sections as a function of angle, it is necessary to normalize the one-detector cross sections up to the

two-detector cross sections. This is done using Eq. A-4.

H. Analyzing Power Calculations

Starting from Eq. A-5, it is possible to solve for the analyzing power. For two-detector calculations, the equations can be manipulated into the following quadratic form:

$$\begin{aligned} & (1 - (LJ*RD)/(LD*RU)) * PU * PD * A^2(\theta) \\ & + (1 + (LJ*RD)/(LD*RU)) * (PD - PU) * A(\theta) \\ & + ((LJ*RD)/(LD*RU) - 1) = 0 \end{aligned} \quad A-19$$

The roots of this equation are:

$$A(\theta) = \frac{-B \pm \sqrt{DISC}}{DENOM} \quad A-20$$

where

$$B = (1 + (LU*RD)/(LD*RU)) * (PD - PU) \quad A-21$$

$$\begin{aligned} DISC = & (1 - (LJ*RD)/(LD*RU))^2 * (PD + PU)^2 \\ & + (4 * (LJ*RD)/(LD*RU) * (PD - PU)^2) \end{aligned}$$

$$DENOM = 2 * (1 - (LJ*RD)/(LD*RU)) * PU * PD$$

The physical solution is the one using the minus sign. There is no dependence on the beam ratio, EFR, or EFFL, because of the appearance of the ratio $(LJ*RD)/(LD*RU)$ in all three terms of Eq. A-19.

For one detector data, the situation is not nearly as complicated. The expression for the one-detector analyzing power can be easily extracted from either the two right detector or the two left

detector equations of Eq. A-5. For the left detector,

$$A_L(\theta) = \frac{RD - RU*BB}{(PU*RD - PD*RU*BB)} \quad A-22$$

The analyzing power of the left detector, $A_L(\theta)$, is the negative of this equation, since it is on the opposite side of the beamline.

I. Error Analysis

The error analysis for this problem is rather complicated. It is necessary to obtain the partial derivatives of the calculated quantities with respect to the measured quantities of the experiment: LUT, LDT, RDT, RUT, PU, PD, MU, MD, LB, ALB, RB, ARB, or, for unpolarized data, LT, RT, MN, LB, RB. As the analysis is formulated in this work, BB is the only calculated quantity depending entirely on input. Starting at this point, it is found that the following hierarchy of dependence is true:

for polarized data:

$$BB = f(MU, MD, PU, PD) \quad A-23$$

$$LUB = g_1(BB, PU, PD, LB, ALB)$$

$$LDB = g_2(BB, PU, PD, LB, ALB)$$

$$RUB = g_3(BB, PU, PD, RB, ARB)$$

$$RDB = g_4(BB, PU, PD, RB, ARB)$$

$$LU = h_1(LUT, LUB)$$

$$LD = h_2(LDT, LUB)$$

$$RU = h_3(RUT, RUB)$$

$$RD = h_4(RDT, RDB)$$

$$A_2(\theta) = k_1(LU, LD, RU, RD, PU, PD)$$

$$\sigma_2 = k_2(LU, LD, RU, RD, PU, PD, BB)$$

$$\begin{aligned} A_r(\theta) &= k_3(RU, RD, PU, PD, BB) && \text{and similarly for } A_l \text{ and } \sigma_l \\ \sigma_r &= k_4(RU, RD, PU, PD, BB) \end{aligned}$$

for unpolarized data:

$$\begin{aligned} LN &= p_1(LT, LB) \\ RN &= p_2(RT, RB) \\ \sigma_2 &= q_1(LN, RN, MN) \\ \sigma_r &= q_2(RN, MN) && \text{and similarly for } \sigma_l \end{aligned}$$

The first step in the error analysis is the calculation of the partial derivatives of BB with respect to its explicitly dependent variables. From this, one can iterate, and, using the chain rule, can calculate the appropriate partial derivatives of the other quantities in question. For example, the expression of the partial of LUB with respect to PU would be

$$\frac{\partial LUB_{tot}}{\partial PU} = \frac{\partial LUB_{ex}}{\partial PU} + \frac{\partial LUB}{\partial BB} * \frac{\partial BB}{\partial PU} \quad A-24$$

where the subscripts "tot" and "ex" are used to distinguish the total dependence from the explicit dependence of a quantity on a variable.

After all the partial derivatives have been calculated, the total error on a quantity can be found using the standard method given by Bevington [Bevi69]

$$\Delta^2 Q = \sum \left[\frac{\partial Q}{\partial V_i} * \Delta V_i \right]^2 \quad A-25$$

where the V_i are all the measured variables and the ΔV_i are the experimental errors in these variables.

For example, in the expression for $\Delta^2 \sigma_2$ there would be a term

$$\left[\frac{\partial \sigma_{\text{tot}}}{\partial \text{PU}} * \Delta \text{PU} \right]^2 \quad \text{A-26}$$

This procedure is used to calculate the errors in the cross section, analyzing power, and $\sigma(\theta) * A(\theta)$.

The errors in the two-detector cross sections ($\sigma_{\ell 2}, \sigma_{r 2}$) determined by Eq. A-4 from σ_r and σ_{ℓ} are given by

$$\Delta^2 \sigma_{r 2} = ((1 + \text{ELER}) * \Delta \sigma_r)^2 + (\sigma_r * \Delta \text{ELER})^2 \quad \text{A-27}$$

$$\Delta^2 \sigma_{\ell 2} = ((1 + 1/\text{ELER}) * \Delta \sigma_{\ell})^2 + \left(\frac{\sigma_{\ell} * \Delta \text{ELER}}{\text{ELER}^2} \right)^2$$

Notice that in the formulas above, ELER is not a calculated quantity, and has no dependence on the other measured quantities. To get the error on the two-detector cross sections which have been normalized down to their single-detector contributions, the following formulas must be used

$$\Delta^2(\sigma_{\ell 2}) = \Delta^2(\sigma_2 / (1 + 1/\text{ELR})) \quad \text{A-28}$$

$$= \sum \left[\left[(1 + 1/\text{ELR})^{-1} * \frac{\partial \sigma_2}{\partial V_i} + \left(\frac{\sigma_2}{\text{ELR}^2 * (1 + 1/\text{ELR})^2} * \frac{\partial \text{ELR}}{\partial V_i} \right) * \Delta V_i \right]^2 \right]$$

$$\Delta^2(\sigma_{r 2}) = \Delta^2(\sigma_2 / (1 + \text{ELR}))$$

$$= \sum \left[\left[(1 + \text{ELR})^{-1} * \frac{\partial \sigma_2}{\partial V_i} - \frac{\sigma_2}{(1 + \text{ELR})^2} * \frac{\partial \text{ELR}}{\partial V_i} \right] * \Delta V_i \right]^2$$

This time, the partial derivatives of ELR must be considered since the value used is now the one calculated on the basis of the individual run (see Eq. A-4).

To arrive at the error in $\sigma_j A_j(\theta)$, where the subscript "j" denotes "2", "2r", or "2f", almost the same technique is used. If it is assumed that all of the partial derivatives of the cross sections and analyzing powers (both one- and two-detector, normalized both ways) have already been determined, it is easy to see that

$$\begin{aligned} \Delta^2(\sigma_j * A_j(\theta)) &= \sum \left[\frac{\partial(\sigma_j * A_j(\theta))}{\partial V_i} * \Delta V_i \right]^2 & \text{A-29} \\ &= \sum \left[\left(\sigma_j * \frac{\partial A_j(\theta)}{\partial V_i} + A_j(\theta) * \frac{\partial \sigma_j}{\partial V_i} \right) * \Delta V_i \right]^2 \end{aligned}$$

J. Weighted Averages

In combining several sets of data, it is usually a straightforward procedure to determine an average value of the results by weighting each entry E_i by its error ΔE_i as follows:

$$Q = \frac{\sum E_i / \Delta^2 E_i}{\sum 1 / \Delta^2 E_i} \quad \text{A-30}$$

[Bevi69].

If all of the entries are uncorrelated, the error on Q would be

$$\Delta^2 Q = \frac{1}{\sum 1 / \Delta^2 E_i} \quad \text{A-31}$$

This is the method used for calculating the weighted averages and errors of σ_2 , $A(\theta)$, and $(\sigma_2 * A(\theta))$. However, this is not quite correct when taking a weighted average of cross sections where both σ_{r2} and σ_{f2} are involved. This is because both σ_{r2} and σ_{f2} depend on the value of ELER (see Eq. A-4). Thus, an error in the estimate of ELER will

affect both of these quantities.

An example may clarify this. Suppose data points were taken under the following conditions

RUN NO.	θ_r	θ_f	A-32
100	100°	70°	
101	80	100	
102	100	100	

The weighted average of all three data points is as expected:

$$\sigma_{\text{avg}} = \frac{\sigma_{f2}/\Delta^2\sigma_{f2} + \sigma_{r2}/\Delta^2\sigma_{r2} + \sigma_2/\Delta^2\sigma_2}{\sum 1/\Delta^2\sigma_i} \quad \text{A-33}$$

where σ_i can be σ_{f2} , σ_{r2} , or σ_2 .

Since each of these runs was done independently, any measurement done during one would not affect a measurement made during the other. (For a moment, let ELER be excluded from consideration.) In effect, this would mean, for example, that there would now be three independent variables labeled PU, one for each run. So, the partial of any of the cross sections with respect to PU would be independent of the partial of any of the other cross sections with respect to PU. This would lead to a term in the error equation of the form

$$\frac{\sum \left[\frac{1}{\Delta^4\sigma_i} * \frac{\partial\sigma_i}{\partial\text{PU}_i} \right]^2 * \Delta^2\text{PU}_i}{\left[\sum 1/\Delta^2\sigma_i \right]^2} \quad \text{A-34}$$

where ΔPU_i is the error on PU for the i^{th} run. This is also true for partials with respect to any of the other variables

(LUT, LDT, RUT, RDT, PD, etc.) as well, except for ELER. Any error made in the determination of ELER would create an error in both σ_{r2} and σ_{f2} , no matter when these one-detector cross sections were measured. Thus, the partial derivative of the average cross section with respect to ELER would look like

$$\left[\frac{\partial \sigma_{\text{avg}}}{\partial \text{ELER}} \right]^2 = \frac{\left[\frac{1}{\Delta^2 \sigma_{f2}} * \frac{\partial \sigma_{f2}}{\partial \text{ELER}} + \frac{1}{\Delta^2 \sigma_{r2}} * \frac{\partial \sigma_{r2}}{\partial \text{ELER}} \right]^2}{\left[\sum 1/\Delta^2 \sigma_i \right]^2} \quad \text{A-35}$$

Note that there does not appear a partial of σ_2 with respect to ELER.

In general, if \bar{E} denotes "all variables except ELER",

$$\Delta^2 \sigma_{\text{avg}} = \frac{\sum \left[\frac{1}{\Delta^4 \sigma_i} * \sum \left[\frac{\partial \sigma_i}{\partial V_j} * \Delta V_j \right]^2 \right]_{\bar{E}} + \left[\frac{1}{\Delta^2 \sigma_{f2}} * \frac{\partial \sigma_{f2}}{\partial \text{ELER}} + \frac{1}{\Delta^2 \sigma_{r2}} * \frac{\partial \sigma_{r2}}{\partial \text{ELER}} \right]^2 * \Delta^2 \text{ELER}}{\left[\sum 1/\Delta^2 \sigma_i \right]^2} \quad \text{A-36}$$

In all cases considered here,

$$\frac{\partial \sigma_{r2}}{\partial \text{ELER}} = \sigma_r \quad \text{A-37}$$

$$\frac{\partial \sigma_{f2}}{\partial \text{ELER}} = -\sigma_f / \text{ELER}^2$$

The contribution to the first term of Eq. A-36 from σ_2 is thus

$$\frac{1}{\Delta^4 \sigma_2} * \Delta^2 \sigma_2 \quad \text{A-38}$$

The corresponding term from σ_{r2} would be

$$\frac{1}{\Delta^4 \sigma_{r2}} * [\Delta^2 \sigma_{r2} - \sigma_r^2 * \Delta^2 \text{ELER}] \quad \text{A-39}$$

and from σ_{f2} ,

$$\frac{1}{\Delta^4 \sigma_{f2}} * [\Delta^2 \sigma_{f2} - \frac{\sigma_{f2}^2}{\text{ELER}^4} * \Delta^2 \text{ELER}] \quad \text{A-40}$$

The last term in Eq. A-36 involving the partials with respect to ELER, is given by

$$\left[\frac{-1}{\Delta^2 \sigma_{f2}} * \frac{\sigma_{f2}}{\text{ELER}^2} + \frac{1}{\Delta^2 \sigma_{r2}} * \sigma_r \right]^2 * \Delta^2 \text{ELER} \quad \text{A-41}$$

Since the $\Delta^2 \sigma_i$ have already been calculated in Eq. A-27, we are merely subtracting off the parts of them which are due to the uncertainty in ELER, and then adding them back in correctly. If, in Eq. A-36, we were to include the error due to ELER in the summation over the V_j in the first term, and to eliminate the second term entirely, we would overestimate the total error. These formulas have been generalized to handle up to sixty measurements.

Bibliography

- [Arvi78] J. Arvieux, J. P. Albanese, M. Buenerd, D. Lebrun
Giant-Resonance Studies via Inelastic Pion
Scattering
Phys. Rev. Lett. 42 (1979) 753
- [Arth75] E. D. Arthur, D. M. Drake, and I. Halpern
Fore-Aft Anisotropy in the Radiative Capture
of 14-MeV Neutrons
Phys. Rev. Lett. 35 (1975) 914
- [Bars70] H. H. Barshall and W. Haeberli, eds.
Polarization Phenomena in Nuclear Reactions
Proc. of the Third International Symposium
Madison, 1970
- [Becc69] F. D. Becchetti, Jr. and G. W. Greenlees
Nucleon-Nucleus Optical Model Parameters,
A < 40, E < 50 MeV
Phys. Rev. 182 (1969) 1190
- [Bel065] T. A. Belote, A. Sperduto, W. W. Buechner
Energy-Level Structure of ^{41}Ca from the
 $^{40}\text{Ca}(d,p)^{41}\text{Ca}$ Reaction
Phys. Rev. 139 (1965) B80
- [Berg74] I. Bergqvist, D. M. Drake, and D. K. McDaniels
Radiative Capture of Fast Neutrons by ^{40}Ca
Nucl. Phys. A231 (1974) 29
- [Bert76] F. E. Bertrand
Excitation of Giant Multipole Resonances through
Inelastic Scattering
Ann. Rev. Nuc. Sci. 26 (1976) 457
- [Bevi69] P. E. Bevington
Data Reduction and Error Analysis for the
Physical Sciences
McGraw-Hill Book Co., New York 1969
- [Blom69] J. Blomqvist and T. T. S. Kuo
Core Polarizations and Particle-Hole Excitations
in ^{40}Ca and ^{48}Ca
Phys. Lett. 29 (1969) 649
- [Braj74] D. Brajnik, D. Jamnik, G. Kernel, U. Miklavzic,
and A. Stanovnik
Photonuclear Reactions in ^{40}Ca
Phys. Rev. C 9 (1974) 1901

- [Brow64] G. E. Brown
Direct and Semi-direct (p, γ) and (n, γ) Reactions
Nucl. Phys. 57 (1964) 339
- [Came77] C. Cameron
Ph.D. Thesis, Duke University 1977
- [Carl75] J. D. Carlson, C. D. Zafiratos, D. A. Lind
Optical Model Analysis of Quasielastic (p,n)
Reactions at 22.8 MeV
Nucl. Phys. A249 (1975) 29
- [Cleg74] T. B. Clegg, G. A. Bissinger, and T. A. Trainor
A Lamb-Shift Polarized Ion Source for the
TUNL Tandem Accelerator
Nucl. Instr. and Meth. 120 (1974)
- [Clem65] C. F. Clement, A. M. Lane, and J. R. Rook
Radiative Capture by Excitation of Collective
Vibrations
Nucl. Phys. 66 (1965) 273
- [Coh55] B. L. Cohen
(p, γ) Cross Sections
Phys. Rev. 100 (1955) 206
- [Dien73] E. M. Diener, J. F. Amann, and P. Paul
Proton Capture into the Giant Dipole Resonance
of ^{40}Ca
Phys. Rev. C 7 (1973) 695
- [Dien73a] E. M. Diener, J. F. Amann, and P. Paul
Isospin Effects in the Giant Dipole Resonance
of ^{42}Ca
Phys. Rev. C 7 (1973) 705
- [Dros78] M. Dros
Unified Absolute Differential Cross Sections for
Neutron Production by the Hydrogen Isotopes for
Charged Particle Energies Between 6 and 17 MeV
Nucl. Sci. and Eng. 67 (1978) 190
- [Garb76] D. I. Garber, and R. R. Kinsey
Neutron Cross Sections; Vol. II, Curves
Information Analysis Center Report, 3rd Ed.
Brookhaven National Laboratory
Upton, N. Y. (1973) 99 BNL 325

- [Gel153] M. Gell-Mann, and V. L. Telgdi
Consequences of Charge Independence for Nuclear
Reactions Involving Photons
Phys. Rev. 91 (1953) 169
- [Goul81] C. R. Gould, L. G. Holzweig, S. E. King, Y. C. Lau,
R. V. Poore, N. R. Roberson, and S. A. Wender
The XSYS Data Acquisition System at
Triangle Universities Nuclear Laboratory
IEEE Trans. on Nucl. Sci. NS-28,
No. 5 (1981) 3708
- [Hann79] S. S. Hanna
Overview of Giant Resonances with Emphasis on
Recent E1 Results
Giant Multipole Resonances
Proc. of the Giant Multipole Resonance Topical
Conf.; Oak Ridge, Tenn., 1979
Fred E. Bertrand, ed.
- [Hayw70] E. Hayward
Photonuclear Reactions
U. S. National Bureau of Standards Monograph No. 118
Washington, D. C., 1970
- [Hayw79] E. Hayward, W. R. Dodge, and B. H. Patrick
Some Experiences Using a Positron Annihilation Beam
Nucl. Instr. and Meth. 159 (1979) 289
- [Holz81] L. G. Holzweig and R. V. Poore
Event Analysis Language 'EVAL' for the
TUNL VAX-11/780
IEEE Trans. on Nucl. Sci. NS-28,
No. 5 (1981) 3815
- [Jens79] M. J. Jensen, D. R. Tilley, H. R. Weller,
N. R. Roberson, S. A. Wender, and T. B. Clegg
Polarized Neutron Capture in the Giant
Resonance Region of ^{41}Ca
Phys. Rev. Lett. 43 (1979) 609
- [Jens81] M. J. Jensen
Fast Neutron Capture by ^{13}C
Ph.D. Dissertation
North Carolina State University, 1981
- [King81] S. E. King, Y. C. Lau, and C. R. Gould
Data Acquisition with a VAX 11/780 and MBD
Branch Driver
IEEE Transactions on Nucl. Sci. NS-28,
No. 5 (1981) 3822

- [Kita80] H. Kitazawa, private communication
- [Lane59] A. M. Lane and J. E. Lynn
Analysis of Experimental Data on Nuclear Capture Reactions
Nucl. Phys. 11 (1959) 646
- [Lang59] A. Langsdorf
Neutron Collimation and Shielding for Experimental Purposes
in Fast Neutron Physics
eds. J. B. Marion and J. L. Fowler,
(New York: Interscience Publishers, 1959) I, 744
- [Leon72] R. Leonardi
Isospin Splitting of the Giant Resonance,
and Neutron and Proton rms Radii
Phys. Rev. Lett. 28 (1972) 836
- [Leon75] R. Leonardi and E. Lipparini
Isospin Splitting of the Giant Resonance.
I. Isodoublets
Phys. Rev. C 11 (1975) 2073
- [Liso75] P. W. Lisowski, R. L. Walter, C. E. Busch,
and T. B. Clegg
Polarization Transfer in the $^2\text{H}(d,n)^3\text{He}$
Reaction at $\theta = 0^\circ$
Nucl. Phys. A242 (1975) 298
- [Long72] G. Longo and F. Saporetti
The Effect of a Volume Form of the Particle-
Vibration Coupling in Fast Nucleon Radiative
Capture
Phys. Lett. 42B (1972) 17
- [Mang81] S. A. Manglos
Ph.D. Thesis, Duke University, 1981
- [Marr75] R. E. Marrs, E. G. Adelberger, K. A. Snover,
and M. D. Cooper
Mirror γ Decays in ^{13}C and ^{13}N
Phys. Rev. Lett. 35 (1975) 202
- [Murp83] K. Murphy
Ph.D. Thesis, Duke University 1983
- [Nils80] L. Nilsson, M. Drog, and D. M. Drake
Isospin Structure of the Giant Dipole Resonance
in ^{42}Ca
Phys. Rev. 21C (1980) 902

- [Nils81] L. Nilsson, M. Drosg, D. M. Drake, and A. Lindholm
Isospin Structure of the Giant Dipole Resonance in ^{41}Ca
Phys. Rev. C 21 (1981) 902
- [Poto73] M. Potokar
The Complex Coupling Interaction in the Radiative
Capture of Fast Nucleons
Phys. Lett. 46B (1973) 346
- [Poto77] M. Potokar, A. Likar, M. Budnar, F. Cvelbar
Analysis of Fast Neutron Capture Data Based on the
Refined Direct-Semidirect Model
Nucl. Phys. A237 (1977) 29
- [Robe81] N. R. Roberson and S. E. Edwards
Interface for the TUNL VAX Data Acquisition Facility
IEEE Trans. on Nucl. Sci. NS-28, No. 5 (1981) 3834
- [Rost79] H. Rost, W. Eyrich, A. Hofmann, U. Scheib,
F. Vogler, and H. Rebel
A Study of the Giant Resonance Region of ^{40}Ca by
Inelastic Scattering of 104-MeV α -Particles
Phys. Lett. 88B (1979) 51
- [Sate72] G. R. Satchler
Excitation of Giant Dipole and Giant Quadrupole
States in Nuclei
Nucl. Phys. A195 (1972) 1
- [Snov76] K. A. Snover, J. E. Bussoletti, K. Ebisawa,
T. A. Trainor, and A. B. McDonald
Application of the Direct-Semidirect Model to the
Interpretation of E1 and E2 Strength
in $^{14}\text{C}(p_{\text{pol}}, \gamma_0)^{15}\text{N}$
Phys. Rev. Lett. 37 (1976) 273
- [Stor70] E. Storm and H. I. Israel
Photon Cross Sections from 1 keV to 100 MeV for
Elements $Z=1$ to $Z=100$
Nucl. Data Tab. 7 No.6 (1970) 565
- [Trai74] T. A. Trainor, T. B. Clegg, and P. W. Lisowski
The Tensor Analyzing Power A_{zz} at $\theta = 0^\circ$
for the $^3\text{He}(d, p)^4\text{He}$ Reaction
Nucl. Phys. A220 (1974) 533-540
- [Uber71] H. Uberall
Electron Scattering from Complex Nuclei
(New York: Academic Press, 1971)

- [Ward81] L. Ward, D. R. Tilley, D. M. Skopik, N. R. Roberson,
and H. R. Weller
Confirmation of the Photoneutron Cross Section for
 ^4He below 33 MeV
Phys. Rev. C 24 (1981) 317
- [Well80] H. R. Weller and N. R. Roberson
Capture Reactions with Protons, Neutrons, and
Alpha Particles
Rev. Mod. Phys. 52 (1980) 699
- [Well82] H. R. Weller, N. R. Roberson, G. Mitev, L. Ward,
and D. R. Tilley
Polarized Neutron Capture on ^3He at $E_n = 9.0$ MeV
Phys. Rev. C 25 (1982) 2111
- [Wend78] S. A. Wender, N. R. Roberson, M. Potokar,
H. R. Weller, and D. R. Tilley
Quadrupole Radiation in Fast-Neutron Capture
on ^{40}Ca
Phys. Rev. Lett. 41 (1978) 1217
- [Wend80] S. A. Wender, C. E. Floyd, T. B. Clegg,
and W. R. Wylie
A High Efficiency Bunching System for
Polarized Beams
Nucl. Instr. and Meth. 174 (1980) 341
- [Wend81] S. A. Wender
A High Efficiency Bunching System for the TUNL
Polarized Ion Source
IEEE Trans. on Nucl. Sci. NS-28 No. 2 (1981) 1465
- [Wend82] S. A. Wender, H. R. Weller, N. R. Roberson,
D. R. Tilley, and R. G. Seyler
Neutron Capture in the Giant Resonance of ^{15}N
Phys. Rev. C 25 (1982) 89
- [Will80] A. Willis, M. Morlet, N. Marty
Excitation of the Giant Dipole Resonance in
 ^{208}Pb , ^{120}Sn , ^{90}Zr , ^{58}Ni , and ^{40}Ca by the Scattering
of 108 MeV Deuterons
Nucl. Phys. A344 (1980) 137
- [Yama78] T. Yamagata, K. Iwamoto, S. Kishimoto, B. Saeki,
and K. Yuasa
Isoscalar Multipole Resonances in ^{40}Ca
Phys. Rev. Lett. 40 (1978) 1628

Biography

Colleen Mary Fitzpatrick

Place and Date of Birth	New Orleans, La. April 25, 1955
University Education	Rice University, Houston, Tex. B. A. Physics, 1976
Positions Held	NSF Research Assistant Chemistry Dept., Rice University 1974, 1975 Teacher-Counselor Ecole d'Humanite CH 6082, Berner Oberland, Switzerland 1976 - 1977 Teaching Assistant, Duke University 1977 - 1978 Research Assistant, Duke University 1978-1983
Memberships	The American Physical Society
Publications	Polarized Proton Capture to the First Excited State of ^{31}P , with C. P. Cameron, N. R. Roberson, Hideo Kitazawa, N. R. Roberson, D. R. Tilley, and H. R. Weller; AIP Conference Proceedings No. 69, Part 1; ed. G. G. Ohlsen et al, p. 602